HERMES



MERCURY

43rd Annual VFS Student Design Competition

Hybrid Electric Tiltrotor

Sponsored by: LEONARDO

UNIVERSITY OF MARYLAND

Alfred Gessow Rotorcraft Center
Department of Aerospace Engineering
University of Maryland
College Park, MD 20740 U.S.A.

Alfred Gessow Rotorcraft Center
Department of Aerospace Engineering
University of Maryland
College Park, MD 20742

Visesh Uppoor
Graduate Student (Team Lead)
vuppoor@umd.edu

Howard Zheng
Graduate Student
hzheng17@umd.edu

Alexander Teacu
Graduate Student
ateacu@umd.edu

Manmohan Thakur
Graduate Student
mthakur@umd.edu

Jacques Read
Graduate Student
jread7@umd.edu

Margaret Donovan
Graduate Student
mdonova8@umd.edu

John Schmidt
Graduate Student
jls99@umd.edu

Dakota Brakob
Graduate Student
dbrakob@umd.edu

John Jessamy
Graduate Student
jjessamy@umd.edu

Dr. Inderjit Chopra
Faculty Advisor
chopra@umd.edu

Dr. Vengalattore Nagaraj
Faculty Advisor
vnagaraj@umd.edu

Dr. Anubhav Datta
Faculty Advisor
datta@umd.edu

Academic Course:
ENAE634: Helicopter Design (3 Credits)

ACKNOWLEDGEMENTS

The UMD graduate design team acknowledges the following people for their invaluable discussion, guidance, and support throughout this project.

Prof. James D. Baeder — Igor Sikorsky Distinguished Professor in Rotorcraft, Department of Aerospace Engineering

Tomasz Krysinski — Visiting Professor, Department of Aerospace Engineering

Dr. Mrinalgouda Patil — Loads and Dynamics Engineer, Joby Aviation

Kumardip Basak — Graduate Student, Alfred Gessow Rotorcraft Center

Xavier Delgado — Graduate Student, Alfred Gessow Rotorcraft Center

Dogyu Jun — Graduate Student, Alfred Gessow Rotorcraft Center

Nathan O'Brien — Graduate Student, Alfred Gessow Rotorcraft Center

Logan Swaisgood — Graduate Student, Alfred Gessow Rotorcraft Center

Vivek Uppoor — Graduate Student, Alfred Gessow Rotorcraft Center



Alfred Gessow Rotorcraft Center
Department of Aerospace Engineering
University of Maryland
College Park, MD 20742 U.S.A.

To the Vertical Flight Society:

The members of the University of Maryland Graduate Student Design Team hereby grant VFS full permission to distribute the enclosed Executive Summary and Final Proposal for the 43rd Annual Student Design Competition as they see fit.

Sincerely,

The UMD Graduate Design Team

Contents

1 Introduction **1**

2 Concept of Operations **3**
2.1 Pre-Flight and Startup . . . 4
2.2 Departure Hover — Segment 1 . . . 4
2.3 Climb — Segment 2 . . . 4
2.4 Cruise — Segment 3 . . . 4
2.5 Descent — Segment 4 . . . 5
2.6 Arrival Hover — Segment 5 . . . 5
2.7 Mission Summary . . . 5

3 Hermes Hybridization **7**
3.1 Hybrid Architectures . . . 7
3.1.1 Series Hybrid . . . 8
3.1.2 Parallel Hybrid . . . 9
3.1.3 Combined Series-Parallel Hybrid Configuration . . . 10
3.1.4 Architecture Comparisons . . . 10
3.2 Hybrid Power Distribution Strategy . . . 11
3.2.1 Power Distribution Principles . . . 11
3.2.2 Experimental Validation . . . 12
3.2.3 Architecture Selection . . . 14
3.3 Reliability . . . 15
3.4 Hybrid Vehicle Sizing . . . 17
3.5 Motor Selection . . . 20
3.6 Battery . . . 21
3.6.1 Battery Management System . . . 22
3.7 Battery and Motor Cooling . . . 22
3.8 Fuel System . . . 23
3.9 Mission Configuration . . . 24

4 Hermes Drive System **26**
4.1 Baseline XV-15 Drive System . . . 26
4.2 *Hermes* Drive System . . . 27
4.3 Gear Sizing . . . 27
4.4 Supercritical Cross-Shaft . . . 29
4.5 Center Gearbox . . . 30
4.6 Material Properties . . . 31
4.7 Auxiliary Components . . . 32

5 Hermes Engine Controls **32**
5.1 Cockpit Controls . . . 32
5.2 Full Authority Digital Engine Controllers . . . 32
5.2.1 Rotor Speed Governing Through Conversion . . . 32
5.3 Hybrid Management Computer . . . 33

6 Hermes Rotor Hub Design **33**
6.1 Hub Selection . . . 33
6.2 Rotor Hub Assembly . . . 34

6.3 Constant-Velocity Joint . . . 34
6.4 Pitch Link and Pitch Horn . . . 35
6.5 Swashplate Design . . . 35
6.6 Finite Element Analysis . . . 36

7 Hermes Vehicle Performance **37**
7.1 Hover Performance . . . 37
7.2 Cruise Performance . . . 37
7.3 Climb Performance . . . 41

8 Mercury Hybridization **44**
8.1 Hybrid Configuration Selection . . . 44
8.2 Selection of Battery and Engine Sizes . . . 45
8.3 Battery and Motor Selection . . . 47
8.4 Battery and Motor Cooling . . . 47
8.5 Fuel System . . . 48
8.6 Mission Configuration . . . 49

9 Mercury Rotor Design **51**
9.1 Blade Aerodynamic Design . . . 51
9.1.1 New AGRC-Series Airfoil Design . . . 51
9.1.2 Blade Planform Optimization . . . 52
9.2 Blade Structural Design . . . 54
9.2.1 Structural Design Approach . . . 55
9.2.2 Internal Blade Structure . . . 55
9.2.3 Blade Root and Hub Attachment . . . 56
9.2.4 Blade Manufacturing . . . 56
9.2.5 Three-Dimensional Stress Analysis . . . 57
9.2.6 Blade Sectional Properties . . . 57
9.3 Rotor Aeroelastic Stability . . . 59
9.4 Rotor Hub . . . 59

10 Mercury Transmission **60**
10.1 Gear Sizing . . . 60
10.2 Cross Shaft . . . 60
10.3 Central Gearbox . . . 61
10.4 Gearbox Casing and Mounting . . . 61

11 Mercury Wing Design **62**
11.1 Wing Aerodynamic Design . . . 63
11.1.1 Wing Airfoil Design . . . 63
11.1.2 Wing Geometry . . . 64
11.2 Wing Structural Design . . . 65
11.2.1 Torque Box Sizing and Stiffness . . . 65
11.2.2 Material Selection and Manufacturing . . . 67
11.2.3 Finite Element Analysis . . . 67
11.3 Whirl Flutter Stability Analysis . . . 69

12 Mercury Airframe Design **70**
12.1 Fuselage Design . . . 70
12.1.1 Fuselage Aerodynamic Design . . . 70
12.1.2 Fuselage Structural Design . . . 72
12.1.3 Finite Element Analysis . . . 72
12.2 Nacelle Design . . . 73
12.2.1 Nacelle Aerodynamic Design . . . 73
12.2.2 Nacelle Structural Design . . . 75
12.3 Landing Gear . . . 75
12.3.1 Tire Selection . . . 75
12.3.2 Landing Gear Position . . . 76
12.4 Crashworthiness . . . 76

13 Mercury Empennage **77**
13.1 Empennage Configuration . . . 77
13.2 Empennage Structure . . . 77

14 Mercury Flight Controls and Avionics **78**
14.1 Fly-by-Wire Architecture . . . 78
14.1.1 Cockpit Controls . . . 79
14.1.2 Full Authority Digital Engine Controllers and Hybrid Management Computer . . . 79
14.2 Avionics . . . 79
14.2.1 Cockpit Layout . . . 79
14.2.2 Avionics Architecture . . . 79
14.2.3 Hybrid Monitoring System . . . 80
14.2.4 Autopilot . . . 81
14.2.5 Communications and Power . . . 81
14.2.6 Health and Usage Monitoring System . . . 81

15 Mercury Flight Dynamics **82**
15.1 Control Mixing . . . 82
15.2 Aircraft Stability . . . 82

16 Mercury Vehicle Performance **83**
16.1 Vehicle Drag Estimation . . . 83
16.2 Hover Download . . . 84
16.3 Hover Performance . . . 85
16.4 Conversion Corridor . . . 86
16.5 Cruise Performance . . . 86
16.6 Climb Performance . . . 88

17 Aircraft Operations and Sustainment **89**
17.1 Technological Risk Assessment . . . 89
17.2 Sustainment Impacts . . . 89
17.3 Emergency Procedures . . . 90
17.3.1 One Engine Inoperative . . . 90
17.3.2 All Engine Inoperative Autorotation . . . 90
17.4 Cost . . . 91

18 Acoustics **92**

19 Proprotor RPM Strategies **92**
19.1 Cruise Rotor Speed Reduction 93
19.2 Rotor Speed Variation During Climb and Descent 94
19.3 Limitations Caused by Mechanical Drive System 94

20 Aircraft Comparisons **95**
20.1 Vehicle Weight and Balance 95
20.2 General Overview of All Aircraft 96

21 Additional Mission Capabilities **97**

22 Summary **98**

23 Team Composition **100**

List of Figures

1.1 *Hermes* and *Mercury* . . . 2
2.1 RFP mission profile. . . . 3
3.1 Block diagram of a series hybrid. Gen = generator, Mot = motor, ESC = electronic speed controller. . . . 7
3.2 Notional sketch of a series hybrid in an XV-15 with an electric drive. . . . 8
3.3 Block diagram of a parallel hybrid. M/G = motor/generator, ESC = electronic speed controller. . . . 9
3.4 Notional sketch of a parallel hybrid in an XV-15 with a mechanical drive. . . . 9
3.5 Block diagram of a combined series-parallel hybrid. Gen = generator, M/G = combined motor/generator unit, ESC = electronic speed controller. . . . 10
3.6 Hybrid and electric aviation test-bed, including the engine, motor, and various sensors. . . . 12
3.7 Battery-engine integration that combines power from both sources. . . . 12
3.8 The core principles of the power distribution strategy with battery recharging are demonstrated in hardware. $P_C = P_{cruise}$ and $P_H = P_{hover}$ . . . 13
3.9 Flowchart for hybrid configuration sizing and selection procedure. . . . 18
3.10 Three engine configuration (3E) analysis. . . . 19
3.11 Sizing the two throttled engines configuration (2E-T). . . . 20
3.12 *Hermes* battery pack design. . . . 21
3.13 *Hermes* cooling system. . . . 23
3.14 *Hermes* fuel bladders (orange) in the left wing. . . . 24
3.15 *Hermes* mission power required and power supplied from the engines. . . . 25
4.1 XV-15 preparing for takeoff. . . . 26
4.2 Unmodified XV-15 drive system. . . . 27
4.3 *Hermes*' drive system architecture. . . . 28
4.4 *Hermes* gearbox inside nacelle with gears highlighted. . . . 29
4.5 *Hermes* cross-shaft first and second natural frequencies with operating RPM band. . . . 30
4.6 Cross-shaft with supporting components. . . . 30
4.7 Half span of transmission between central gearbox and nacelle. . . . 31
4.8 *Hermes* central gearbox. . . . 31
6.1 Gimbaled rotor hub assembly. . . . 34
6.2 Constant-velocity joint exploded view. . . . 35
6.3 Yoke FEA at 2g hover loading condition. . . . 36
7.1 *Hermes* hover power required and total maximum rated power (MRP) and battery power available under ISA and ISA +20°C conditions at various pressure altitudes. . . . 37
7.2 Power required in flight of the XV-15 and *Hermes* in helicopter, conversion, and airplane modes. Symbols: XV-15 flight test data, lines: predictions. . . . 38
7.3 L/D of the XV-15 and *Hermes* in helicopter, conversion, and airplane modes. Symbols: XV-15 flight test data, lines: predictions. . . . 39
7.4 Velocities for best endurance and range for the XV-15 and *Hermes*. . . . 39
7.5 Range and endurance of XV-15 and *Hermes* with two pilots. . . . 40
7.6 Height-velocity envelope for XV-15 and *Hermes*. . . . 40
7.7 Climb rate of XV-15 and *Hermes* with varying power usage. . . . 41
8.1 Comparison of two hybrid configurations with each point representing a set of design parameters for each configuration. . . . 45
8.2 Required weight of hybrid propulsion components resulting from the amount of electrical power needed to hover for multiple charge/discharge cycles in cruise. . . . 46

8.3 Battery charge and discharge C-rates resulting from the amount of electrical power needed to hover for various charge-discharge cycle counts. . . . 46
8.4 Mercury battery pack design. . . . 47
8.5 *Mercury* liquid cooling system for battery and motor. . . . 48
8.6 *Mercury* fuel bladders (orange). . . . 49
8.7 *Mercury* mission power required and power supplied from the engines. . . . 50
9.1 Spanwise sectional angle of attack and Mach number in hover and cruise modes of the *Hermes*. 52
9.2 Geometry and aerodynamic performance of baseline and optimized rotor blade airfoils. . . . 53
9.3 *Mercury* proprotor planform optimization Pareto front. . . . 54
9.4 *Hermes* and *Mercury* proprotor twist and chord distribution. . . . 54
9.5 *Mercury* proprotor blade planform with airfoil section transitions. . . . 55
9.6 Proprotor blade cross-section. . . . 56
9.7 Rotating bending stresses on *Mercury* blade in hover. . . . 57
9.8 Non-dimensional blade sectional property distributions. . . . 58
9.9 *Mercury* fan plots at hover and cruise operating conditions. . . . 59
10.1 *Mercury* nacelle gearbox in cruise. . . . 60
10.2 *Mercury*'s drive system architecture diagram. . . . 61
10.3 *Mercury* cross shaft first and second natural frequencies with operating RPM band. . . . 62
10.4 *Mercury* central gearbox cutaway, with highlighted spur gears and coolant pump. . . . 62
11.1 Aerodynamic comparison of candidate wing airfoil sections evaluated using CFD. . . . 63
11.2 Comparison of NACA 64A413 and AGRC-W413 wing airfoils. . . . 65
11.3 Wing surface c_p distribution and streamlines at cruise. . . . 66
11.5 Grid search results for the wing torque box skin composite layup, showing half wing torque box weight of feasible designs that meet XV-15 stiffness targets. . . . 66
11.4 Grid search results for the wing torque box skin composite layup, showing half wing torque box weight of feasible designs that meet XV-15 stiffness targets. . . . 67
11.6 Wing FEA at 3.5g airplane mode loading condition. . . . 68
11.7 Wing FEA at 2g hover loading condition. . . . 68
11.8 University of Maryland Tiltrotor Rig (MTR) in the Glenn L. Martin Wing Tunnel. . . . 69
11.9 Mercury Whirl flutter stability analysis. . . . 70
12.1 Frontal area cross-section comparison. . . . 71
12.2 Fuselage surface C_p with streamlines at cruise conditions. . . . 71
12.3 *Mercury* Internal structure. . . . 73
12.4 *Mercury* fuselage finite element model. . . . 74
12.5 : Surface c_p with streamlines from CFD for nacelles in airplane mode. . . . 74
12.6 Nacelle in helicopter mode. . . . 75
12.7 Nacelle in airplane mode. . . . 75
13.1 Cruise stability roots for *Mercury* with a V-tail and cruciform tail design compared to the XV-15 . . . 78
13.2 *Mercury* vertical and horizontal stabilizers have independent load paths to the fuselage structure. . . . 78
14.1 Flight controls diagram. . . . 78
14.2 *Mercury* cockpit and cabin top view. . . . 79
14.3 Copilot cockpit view. . . . 80
14.4 *Mercury* hybrid monitoring system. . . . 80
14.5 Health and usage monitoring system flowchart. . . . 81
15.1 *Mercury* open loop stability roots in hover and airplane cruise. . . . 83
16.1 Hover download factor variation with wing flap deflection. . . . 84

16.2 *Mercury* hover power required and maximum rated power (MRP) available from the engines under ISA and ISA+20 conditions at different pressure altitudes. 85
16.3 Conversion corridor for *Mercury* with $\theta_{flap} = 0°$. 86
16.4 Power required at sea level for *Mercury* in helicopter, conversion, and airplane modes with best endurance and best range velocities in airplane mode. 87
16.5 L/D at sea level for *Mercury* in helicopter, conversion, and airplane modes. 87
16.6 Range and endurance of *Mercury* with two pilots. 88
16.7 Height-velocity envelope for *Mercury* in airplane mode. 89
16.8 Climb rate of *Mercury* at sea level with various combinations of battery and engine usage. . 89
17.1 Power flow diagram during OEI and AEI operations of *Hermes* and *Mercury* hybrid powertrain. 91
18.1 Noise comparison between *Hermes* and *Mercury* in hover at 4K/95. 92
19.1 Cruise performance of *Hermes* and XV-15 at 3048 m (10000 ft) altitude and 156 m/s (303 kt) airspeed for varying rotor RPM. 93
19.2 Effect of rotor RPM on climb, cruise, and descent power and fuel consumption for *Mercury*. 94
20.1 Center of gravity (CG) variation for XV-15, *Hermes*, and *Mercury*. 95
21.1 Alternative mission capabilities of *Mercury*. 98

List of Tables

2.1 Mission summary for *Hermes* and *Mercury*. 5
3.1 Series hybrid and parallel hybrid weight breakdown 14
3.2 USAF risk level matrix by severity and frequency 15
3.3 Engine reliability over 7.4 million flight hours 16
3.4 Component reliability breakdown 16
3.5 RAC levels for series and parallel configurations 17
3.6 *Hermes* Battery specifications: cell, module, and pack 21
3.7 *Hermes* Cooling System 22
3.8 Mission parameters for *Hermes* 24
3.9 *Hermes* battery usage during the mission. 25
4.1 *Hermes* transmission, stage gear ratios 28
8.1 *Mercury* Battery specifications: cell, module, and pack 47
8.2 *Mercury* Cooling System 48
8.3 Mission parameters for *Mercury* 49
8.4 *Mercury* battery usage during the mission. 50
9.1 *Hermes* / XV-15 rotor blade airfoil sections. 51
9.2 Blade natural frequencies in hover, 9.2° collective, 589 RPM. 58
9.3 Blade natural frequencies in cruise, 56.1° collective, 343 RPM. 58
10.1 *Mercury's* Transmission Stage Gear Ratios 61
11.1 Wing parameters for *Hermes* and *Mercury*. 64
11.2 Wing natural frequencies (/rev) at cruise RPM. 69
12.1 Tire Parameter. **Chosen tire.* 76
15.1 Control Mixing Strategy 82
16.1 Component wise flat-plate drag area breakdown for *Hermes* and *Mercury* in airplane mode 84
16.2 Vertical drag breakdown for *Mercury* in hover at 4K/95. 85
19.1 Rotor Speeds for XV-15, *Hermes*, and *Mercury* 95
20.1 Full Weight Breakdown 96
20.2 General Vehicle Parameters 97

RFP Compliance Matrix — *Hermes* (Phase I) and *Mercury* (Phase II)

RFP Requirement	Source	*Hermes*	*Mercury*
Civil/commercial OEI operating standards	2.2	17.3.1	17.3.1
Phase I — Constrained Hybrid Propulsion Design of the XV-15			
Hybrid architecture trade study and selection	2.2.1	3.1	—
Hybrid vehicle sizing; ≥10% mission power from electric source	2.2.1	3.4	—
Battery specification compliance-	2.2.1	3.6	—
Drive system and transmission design	2.2.1	4	—
Phase II — Minimally Constrained Hybrid Electric Tiltrotor Design			
Hybrid architecture selection and sizing	2.2.2	—	8
Payload: 1600 lb; cabin for 6 passengers + crew	2.2.2	—	12, 20.1
$V_{NO} \geq 300$ ktas; $V_{NE} \geq 350$ ktas	2.2.2	—	16.5
HOGE ≥ 4536 kg (10,000 lb) at 4000 ft/95°F	2.2.2	—	16.3
Load factors: 2G (helicopter/conversion), 3.5G (airplane)	2.2.2	—	9.2
Autorotation at any airspeed and flight mode	2.2.2	—	17.3
Mission Performance (RFP 2.3, 2.4)			
HOGE power required vs. gross weight	2.3	7.1	16.3
Cruise power required vs. airspeed; V_{be}, V_{br}	2.3	7.2	16.5
Payload-range diagram	2.4	7.2	16.5
Height-velocity diagram	2.4	7.2	16.5
Climb performance	2.3	7.3	16.6
Weight & Balance			
Component weight breakdown	2.4	20.1	20.1
CG analysis and evolution through mission	2.4	20.1	20.1
Design parameters table (RFP Table 2)	2.4	20.2	20.2
Hybrid Electric System			
Architecture discussion, trade studies, and operational impacts	2.4	3.1–3.3	8.1–8.2
Technology risk assessment	2.4	17.1	17.1
Manufacturing, operations, and sustainment	2.4	17.2	17.2
Graduate Task			
Proprotor RPM strategies and hybrid system implications	2.5	19	19

1 Introduction

The tiltrotor configuration has established itself as the premier solution for long-range vertical flight. By transitioning from rotor lift in hover to wing lift in cruise, tiltrotors achieve ranges and speeds that conventional helicopters cannot match while retaining vertical takeoff and landing capability. The Bell XV-15 is the most thoroughly documented example of this configuration, with an extensive flight test and research record spanning decades. Its successors, the Bell Boeing V-22 Osprey and the Bell V-280 Valor, have demonstrated the operational value of the tiltrotor concept across thousands of flight hours in demanding military service. The civil tiltrotor market offers the next frontier for this configuration, with vehicles such as the Leonardo AW609 offering high-speed regional runway independent air mobility.

Realizing the full potential of civil tiltrotors requires pushing the configuration's performance envelope further in three ways. First, "hot and high" hover capability is essential for operations across all terrains and climates. Second, high cruise speeds are necessary to make the tiltrotor economically competitive with fixed-wing aircraft. Third, fuel efficiency directly affects operational cost, which governs whether civil tiltrotor operations are commercially viable at scale. Improvements in these areas are also transformative for time-critical operations such as Emergency Medical Services (EMS), where patient outcomes are strongly influenced by the ability to deliver care within the first "golden hour" following a traumatic injury [1], and Search and Rescue (SAR), where faster arrival on scene grants crews a wider window to execute rescues.

Hybrid electric propulsion offers a promising pathway to all these three areas of performance improvement. The automotive industry has demonstrated the principle at scale. The Toyota Prius, and generations of hybrid vehicles that followed, established that pairing a thermal engine with an electric motor allows it to always operate close to its most fuel efficient point, with the electric system covering peak power demands. This enables the thermal engine to be better matched to the demands of the majority of the mission, rather than being sized for the short highest power segments. The aerospace industry has recently accelerated similar efforts, with demonstrator programs like the Airbus EcoPulse validating distributed hybrid-propulsion architectures [2] and NASA's Revolutionary Vertical Lift Technology (RVLT) project establishing the design space for hybrid-electric VTOL concepts [3]. Academic research has further explored these benefits, showing that hybrid architectures have the potential to reduce fuel burn, increase range, and reduce emissions [4, 5].

The University of Maryland responds to the two phases of the 43rd Annual VFS Student Design Competition to design a hybrid electric tiltrotor, sponsored by Leonardo Helicopters, with two vehicles: ***Hermes*** for phase 1 and ***Mercury*** for phase 2 (Fig. 1.1). The names Hermes and Mercury draw from the Greek and Roman gods of travel and commerce. Swift and light by nature, Hermes and Mercury embody the vehicles' dual mandate: minimizing weight without sacrificing performance and completing missions that demand both hover capability and efficient high-speed cruise.

Hermes is a parallel hybrid redesign of the XV-15 in response to phase 1, with the same gross takeoff weight of 5897 kg (13,000 lb), retaining the proven T53 turboshaft engines in the nacelles and adding a single electric motor and battery pack at the fuselage center. In this parallel hybrid architecture, both the thermal engines and the electric motor drive the proprotors mechanically through the drivetrain, with no intermediate conversion to electrical power. This approach retains the hybrid benefit while minimizing added component weight, requiring no additional generators or power conversion hardware beyond the motor inverter. Compared to a series and series-parallel architecture, this design also removes failure modes in the powertrain and thus improves reliability. A lightweight supercritical cross-shaft transmits the electric motor power mechanically to both rotors and provides engine-out redundancy, a safety critical feature for civil certification. *Hermes* reduces rotor speed by 42% in cruise using a proven gimbaled hub based on the V-22, enabling sustained flight at 156 m/s (260 KCAS) at 3,048 m (10,000 ft) through the

567 km (306 nm) mission with reserves. The empty weight of 4,572 kg (10,038 lb) is marginally lower than the original XV-15 despite the addition of hybrid components, achieved through modern drivetrain architecture and electronic hybrid engine control.



Figure 1.1: *Hermes* and *Mercury*

Mercury is a clean-sheet, highly optimized parallel hybrid-electric tiltrotor in response to phase 2 that leverages modern materials and aerodynamic optimization to maximize the benefits of the hybrid powertrain. *Mercury* features a composite construction proprotor with a tailored aerodynamic planform improving propulsive efficiency and hover figure of merit by 5.9% and 6.3% respectively compared to the XV-15 proprotor. A 29% reduction in fuselage drag is achieved through a slim fuselage enabled by a 1x6 seating configuration and tandem pilot seats. A thin 13% thick carbon/epoxy composite wing free from whirl flutter past the limit airspeed of 180 m/s (350 kt) further results in an overall vehicle drag reduction of 28% compared to the XV-15 baseline. Utilizing 30% downscaled T53 engines, *Mercury's* hybrid power system is sized through the same process as *Hermes*. A fully digital fly-by-wire control system and Full Authority Digital Engine Controllers (FADEC) reduce pilot workload and enable simple operation of the hybrid power cycling strategy in cruise. These features are all packaged in a 4,939 kg (10,891 lb) gross take off weight aircraft, 16% lighter than *Hermes* and the XV-15.

Hermes and *Mercury* translate the automotive hybrid principle directly to the tiltrotor mission. As in the Toyota Prius, the turboshaft engines are held at their most efficient operating point, maximum continuous power (MCP), throughout cruise. Surplus power beyond what the proprotors require is used to charge the battery through the electric motor operating as a generator. Once fully charged, the electric motor engages and the turbine engines throttle down, maintaining total shaft power. This unique cycling procedure is used throughout the mission to keep the turbine engines at MCP as long as possible, leading to fuel savings. In addition to efficiency, the electric motor and battery provide an additional safety margin: in the event of a single-engine failure, the battery supplies supplemental shaft power. In the case of a dual engine failure, and at any airspeed or flight mode, the electric motor sustains rotor RPM as the nacelles tilt vertical to begin autorotation. Both vehicles are capable of hover out of ground effect at full gross takeoff weight in 1,219 m / 35°C (4,000 ft / 95°F) conditions, utilizing the electric motor to supplant the turbine engines at takeoff power setting. In cruise, both vehicles are capable of sustained flight at 260 KCAS (303 KTAS) at 3,048 m (10,000 ft) through the 567 km (306 nm) mission with reserves, competitive with fixed-wing regional turboprops on speed while offering the unique flexibility of vertical take-off and landing. These high performance hover and cruise capabilities are beyond what the XV-15 design could achieve, enabled by the inclusion of the hybrid-electric powerplant.

Hermes and *Mercury* demonstrate that hybrid electrification of a tiltrotor platform is not only technically achievable but offers a compelling combination of performance, efficiency, and commercial viability for the emerging civil tiltrotor market.

This report begins with the design of *Hermes*, covering the modifications from the XV-15 in chapters 3 to 7. The design of *Mercury* is covered in chapters 8 to 16. Considerations for both vehicles are detailed in the remainder of the report.

2 Concept of Operations

Hermes and *Mercury* are civil hybrid-electric tiltrotors designed to fulfill a 567 km (306 nm) regional transport mission while retaining vertical takeoff and landing capability. The tiltrotor configuration is uniquely suited to time-critical operations, including emergency medical services, search and rescue, and regional air mobility, where the combination of VTOL flexibility, and fixed-wing cruise speed and range cannot be matched by either a helicopter or a conventional turboprop. Both vehicles carry two pilots at 181 kg (400 lb) combined. *Hermes* can carry an additional 510 kg (1,123 lb) of payload for a total payload of 691 kg (1,523 lb). *Mercury* carries six passengers at 544 kg (1,200 lb), for a total payload of 727 kg (1,600 lb) including pilots. The primary mission profile shared by *Hermes* and *Mercury* is shown in Fig. 2.1 and consists of five segments: departure hover, climb, cruise, descent, and arrival hover. The hybrid strategy operates automatically but transparently to the pilots through all segments, managed by the Hybrid Management Computer (HMC) in coordination with FADECs on each turboshaft engine.

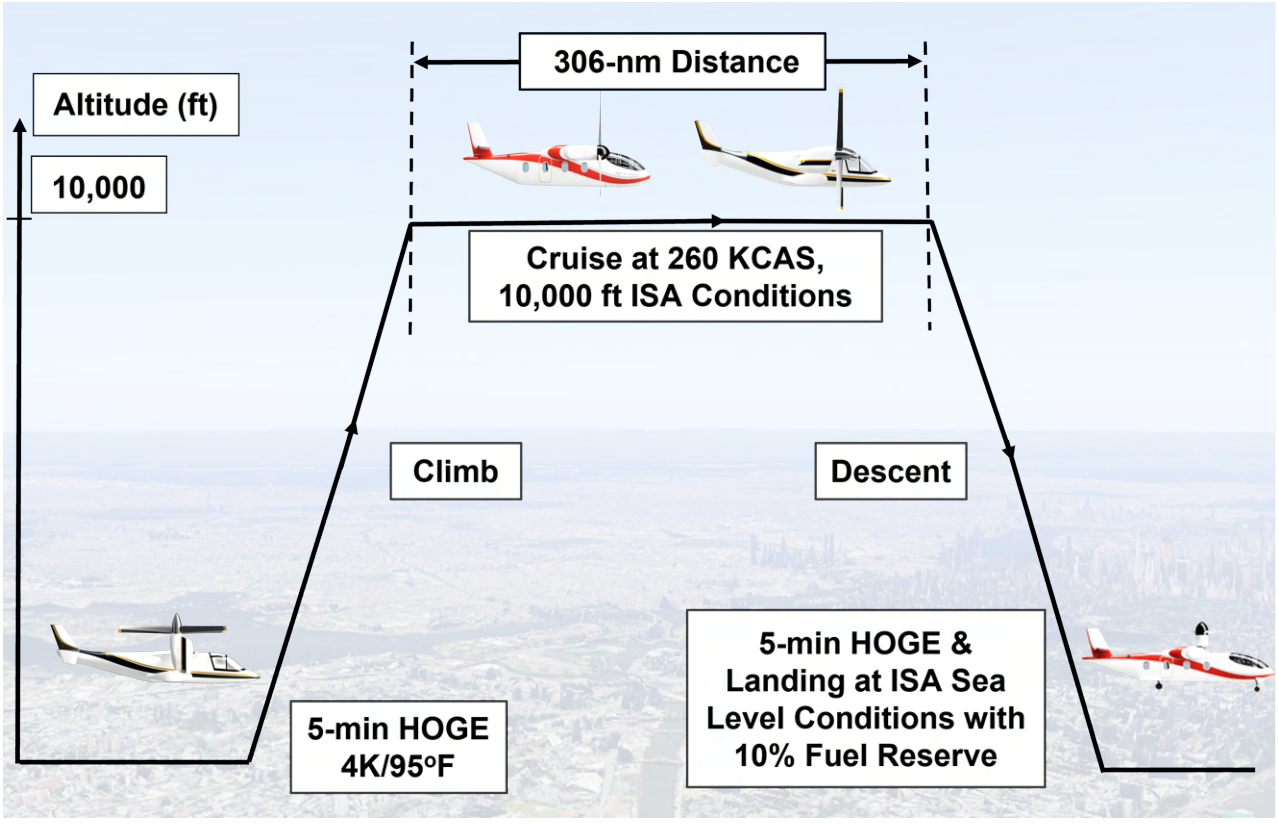


Figure 2.1: RFP mission profile.

2.1 Pre-Flight and Startup

Both vehicles start with nacelles vertical and proprotors faced upward. Engine start is initiated sequentially using console start buttons. The engine is monitored automatically by the FADEC, which sequences fuel flow, ignition, and acceleration to ground idle without pilot intervention. Once both engines reach idle, the HMC performs a self-test of the battery, motor, and inverter and posts a go/no-go status on the hybrid monitoring display.

2.2 Departure Hover — Segment 1

Both vehicles lift off vertically with nacelles at 90°. *Hermes* departs at its full gross takeoff weight of 5,897 kg (13,000 lb), and *Mercury* departs at 4,939 kg (10,891 lb). The departure hover is performed at 1,219 m / 35°C (4,000 ft / 95°F) conditions. Under these "hot-and-high" conditions, the turboshaft engines at takeoff power setting alone cannot sustain hover. The electric motor supplements the turbine engine outputs, providing 180 kW (245 HP) for *Hermes* and 162 kW (220 HP) for *Mercury*, for the five-minute hover segment. The battery discharges at a C-rate of 9.0 and 9.5 respectively. At the end of the hover segment each vehicle has consumed approximately 56 kg (124 lb) and 36 kg (80 lb) of fuel respectively.

2.3 Climb — Segment 2

Following the hover segment, the pilots initiate a conversion to forward flight by adding forward cyclic followed by advancing the nacelle tilt switch. As the vehicle reaches a threshold speed, the nacelles tilt forward from 90° toward 0° in approximately 12 seconds. As the forward speed increases, wing lift progressively replaces rotor lift and the proprotors transition from a lifting to a propulsive role. The mechanical flight controls carried over from XV-15 into *Hermes* and the fly-by-wire system in *Mercury* mix the pilot control inputs into corresponding swashplate and control surface outputs automatically as a function of airspeed.

Once commanded by the pilot and established in airplane mode with nacelles at 0°, the FADEC initiates the rotor speed reduction as the vehicle accelerates through the scheduled airspeed threshold. *Hermes* and *Mercury* both reduce rotor speed from 589 RPM to 343 RPM, a 42% reduction enabled by their gimbaled constant-velocity rotor hubs.

Both vehicles climb to 3,048 m (10,000 ft) ISA at 64 m/s (125 kt). During climb, the engines are throttled to MCP and surplus shaft power charges the battery through the motor operating as a generator, recharging the battery fully before the cruise segment begins. *Hermes* completes the climb in 10.6 minutes; *Mercury* in 5.5 minutes.

2.4 Cruise — Segment 3

Both vehicles cruise in airplane mode at 156 m/s (260 KCAS, 303 KTAS) at 3,048 m (10,000 ft) ISA for 60.7 minutes, covering the 306 nm mission distance. The hybrid cycling strategy operates continuously through cruise. The HMC alternates between running the turbine engines at MCP while recharging the battery, and running the electric motor to discharge the battery and throttling down the turbine engines. This cycling repeats automatically throughout cruise — five charge/discharge cycles for *Hermes* and four for *Mercury* — keeping the engines near their peak efficiency point throughout the segment. The pilot monitors the hybrid system state through a dynamic energy flow display in the cockpit. The discharge C-rate during cruise is maintained below 9 for both vehicles.

Cruise is the dominant fuel-consuming segment, accounting for 550 kg (1,212 lb) of fuel for *Hermes* and

408 kg (898 lb) for *Mercury*. The fuel savings from the hybrid cycling strategy are realized here: by keeping engines at MCP during charge phases and supplementing the rotor power with the battery during discharge phases, both vehicles achieve lower specific fuel consumption than the unmodified XV-15 operating at a fixed throttle setting.

2.5 Descent — Segment 4

Descent from 3,048 m (10,000 ft) to the destination site is initiated by reducing throttle and pitching the aircraft into a descent attitude. Engine power during descent is substantially below MCP, so the surplus in available shaft power recharges the battery through the motor operating as a generator. *Hermes* recharges at 102 kW (139 HP) over 10 minutes; *Mercury* at 80 kW (109 HP) over 10 minutes. The battery is returned to full charge before arrival hover begins.

As the vehicle decelerates through the airspeed threshold and following pilot command, the FADEC initiates a rotor speed increase to 589 RPM prior to nacelle tilting, ensuring full hover RPM is available before conversion. The pilots then command the nacelle tilt from 0° back to 90° to transition back to helicopter mode.

2.6 Arrival Hover — Segment 5

The arrival hover is performed at sea-level ISA conditions. At sea level, both engines alone can sustain hover without motor assist, but the battery begins this segment fully charged. Therefore, this energy is utilized. In this segment, the electric motor provides 180 kW for *Hermes* and 162 kW for *Mercury*. Both vehicles land vertically at the destination pad after the five-minute arrival hover. The total fuel reserve carried is 83 kg (184 lb) for *Hermes* and 62 kg (136 lb) for *Mercury*, representing 10% % of the mission fuel as required by the RFP.

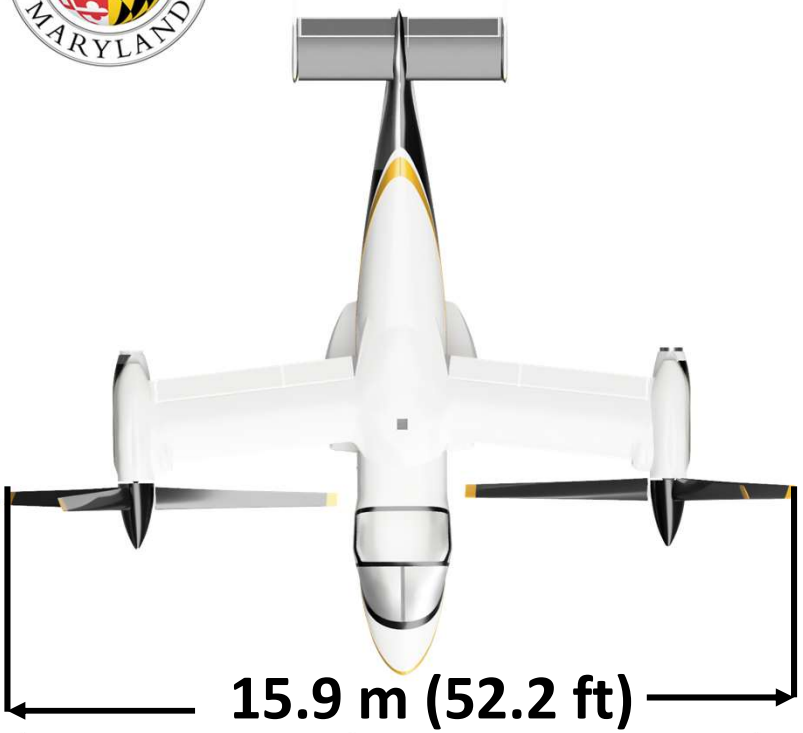
2.7 Mission Summary

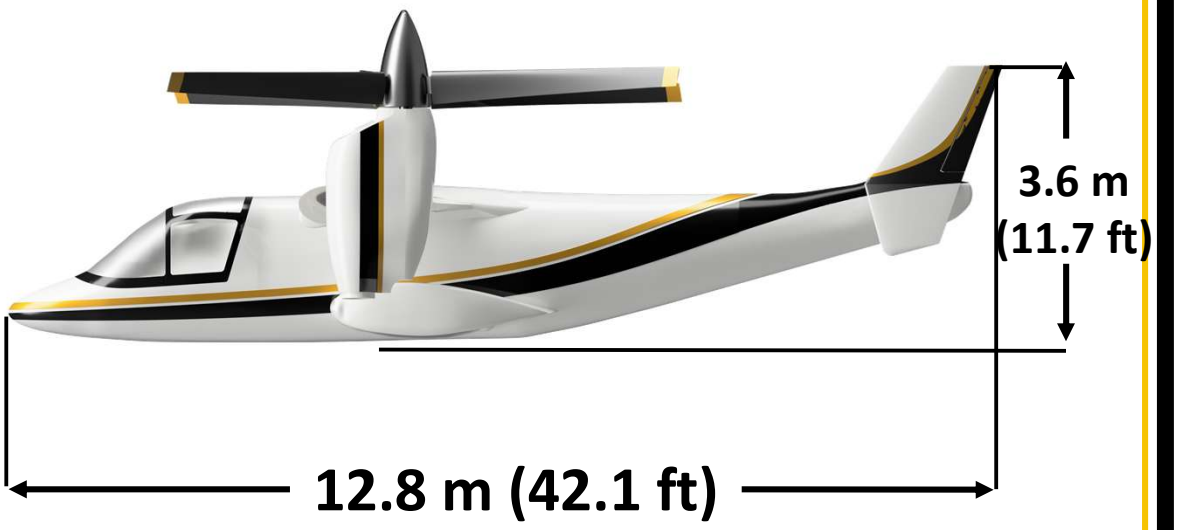
The complete mission parameters for both vehicles are summarized in Table 2.1. *Mercury*'s 28% lower vehicle drag and 15% lower gross takeoff weight reduce the total mission fuel by 26% relative to *Hermes*, from 834 kg (1,839 lb) to 615 kg (1,355 lb), while completing the same 567 km (306 nm) mission with similar payload. Both vehicles demonstrate that the parallel hybrid electric architecture, with its MCP cycling strategy, delivers fuel efficiency gains over the XV-15 baseline while enabling improved "hot-and-high" hover performance through electric motor assistant.

Table 2.1: Mission summary for *Hermes* and *Mercury*.

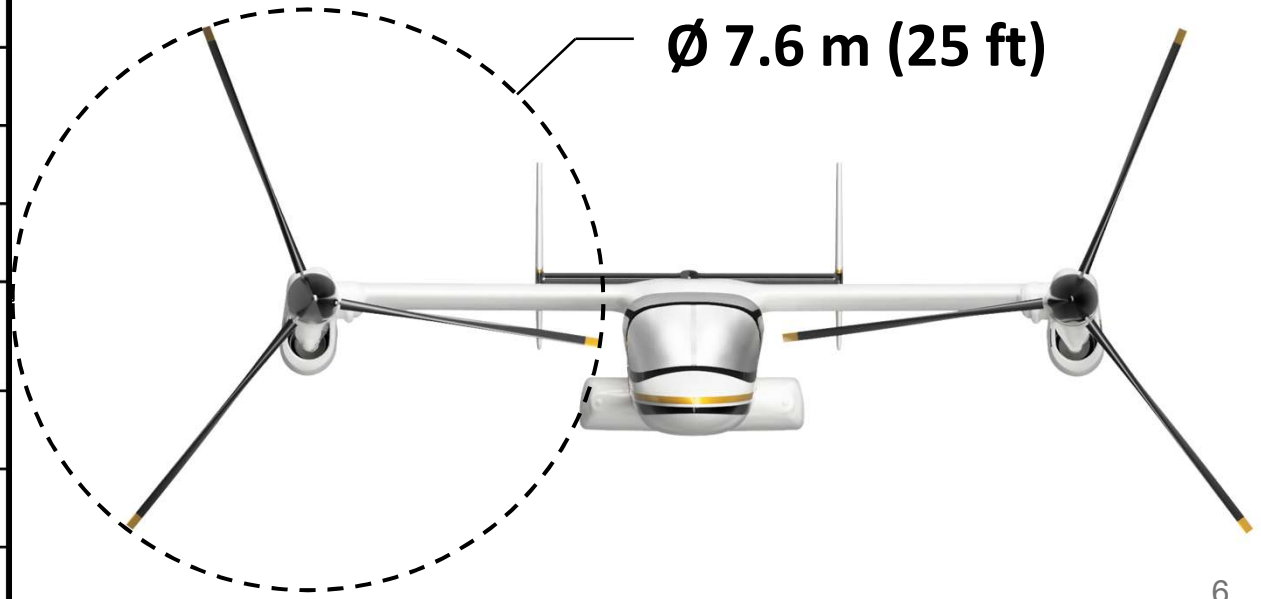
Segment	**Duration (min)**	**Conditions**	**Fuel Used, kg (lb)**	
			Hermes	*Mercury*
Departure HOGE	5	4K/95°F, GTOW	56 (124)	36 (80)
Climb	10.6 / 5.5	ISA	56 (123)	39 (87)
Cruise	60.7	ISA, 10,000 ft	550 (1212)	408 (898)
Descent	10	ISA	37 (81)	33 (72)
Arrival HOGE	5	ISA SL	52 (115)	37 (82)
Reserve (10%)	—	—	83 (184)	62 (136)
Total	**91.3 / 86.2**	—	**834 (1839)**	**615 (1355)**

Hermes Overview, Phase 1





Characteristics	Value
GTOW	5897 kg (13000 lb)
Payload	509 kg (1123 lb)
Fuel Weight	834 kg (1839 lb)
Turboshaft Power	1864 kW (2500 hp)
Electrical Power	180 kW (241 hp)
Range	1308 km (706 nm)
Max Speed	163 m/s (317 kts)



3 Hermes Hybridization

A novel hybrid-electric transmission is at the heart of the new design. The crucial elements of this transmission – engine-coupled generator and battery-recharge cycles are hardware tested in the lab to establish their feasibility and reliability. This test data became the basis for the design.

The original XV-15 has a propulsion system comprised of two Lycoming T53 turboshaft engines located in the nacelles. These turbine engines are mechanically connected to the proprotors through a series of gearboxes. The novel engine-battery hybridization strategy proposed for *Hermes* realizes a significant boost in performance although at the expense of increased system complexity. Among the various electrical power sources available for hybridization, the two most practical are batteries and hydrogen fuel cells. The battery hybridization is preferred due to its compactness, maturity, and simplicity compared to high volume tanks required for hydrogen. Using this strategy, *Hermes* gains an 8% increase in maximum continuous power (MCP) at sea level over the XV-15 with mild changes to empty weight. This enables *Hermes* to hover at 1,219 m / 35°C (4000 ft / 95°F) atmospheric conditions and cruise at 260 KCAS (303 KTAS) at 3048 m (10,000 ft) altitude, which are not possible with the existing XV-15 propulsion system.

Hybrid technology commercialized for automobiles and ground vehicles are not suitable for aircraft. Regenerative braking, one of the core principles of automotive technology, is not viable for any practical flight segment. The variation of speed and power are also different for aircraft – rotor speed and power decrease with aircraft speed, opposite of what is needed in ground vehicles – necessitating a new approach to hybridization.

A unique hybrid power strategy is used for *Hermes* that enables improved performance versus XV-15 by minimizing engine weight and specific fuel consumption (SFC). This hybrid power distribution strategy has been studied through experimental testing conducted at the University of Maryland's Alfred Gessow Rotorcraft Center (UMD AGRC) [6–10]. Using this strategy, a parallel hybrid architecture for *Hermes* is selected for to its low weight and reliability.

3.1 Hybrid Architectures

In this section, three existing engine-battery hybrid architectures are analyzed: series, parallel, and series-parallel configurations.

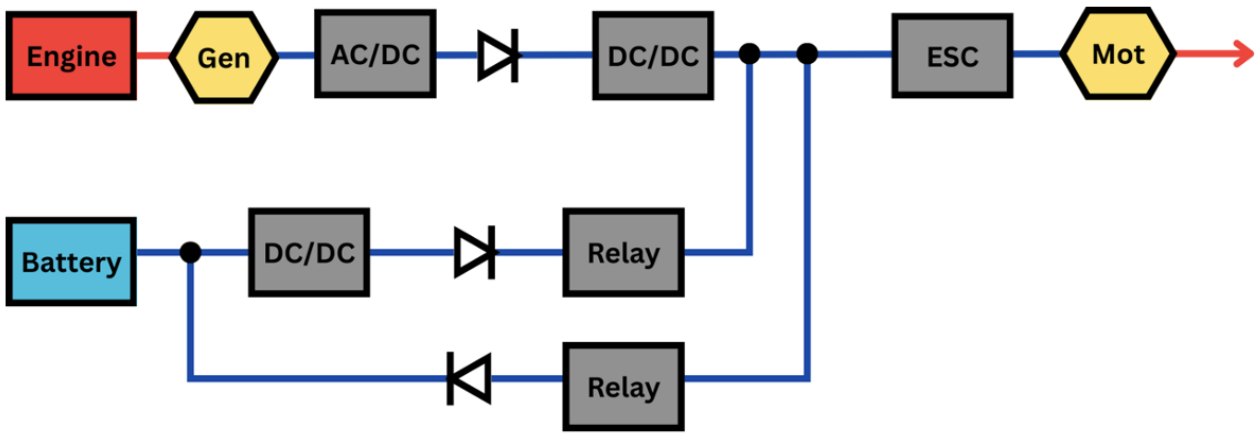


Figure 3.1: Block diagram of a series hybrid. Gen = generator, Mot = motor, ESC = electronic speed controller.

3.1.1 Series Hybrid

In the series hybrid configuration, both power sources are connected in such a way that the load is always driven electrically as shown in Fig. 3.1. The power components comprise of two parallel branches, one for the engine and one for the battery. The engine branch burns fuel with an internal combustion engine, which then converts mechanical power into AC electrical power through a generator. The three following components, an AC/DC rectifier, a power diode, and a DC/DC converter, then converts this AC power into DC power that only flows out from the engine branch and can be combined with any other DC power source. The battery branch is already DC power. There are two relay activated paths for the battery branch, one discharge path with a DC/DC converter to hold a constant voltage as the battery depletes, and one recharge path that takes excess power in. The AC/DC rectifier, DC/DC converters, diodes, and relays comprise the power electronics needed for discharging and recharging the battery. The shared voltage bus powers an electronic speed controller (ESC) and a motor, which then feeds into the load.

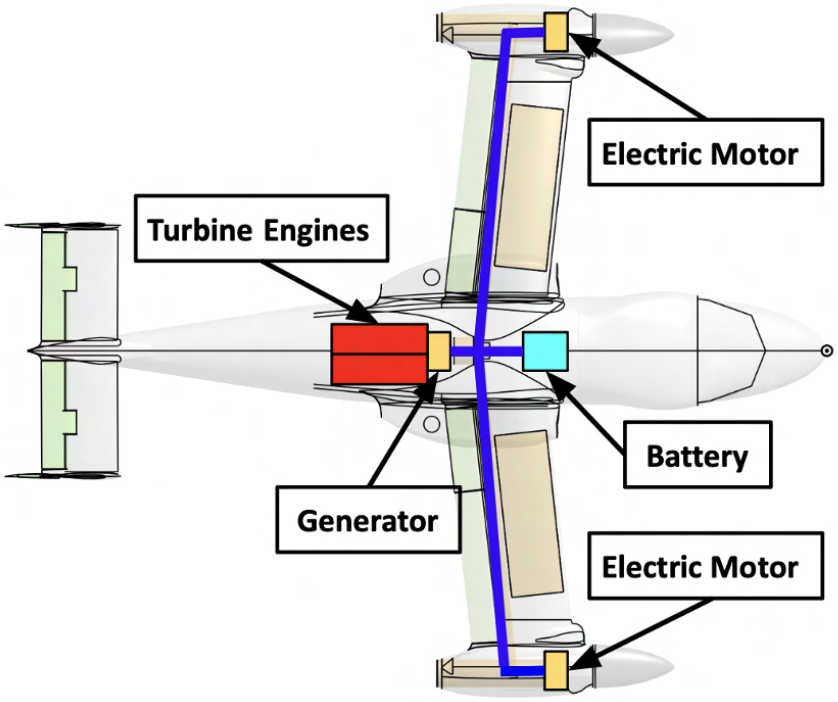


Figure 3.2: Notional sketch of a series hybrid in an XV-15 with an electric drive.

Adapting this architecture for the *Hermes* design and replacing the original XV-15 power plant would follow what is shown in Fig. 3.2. The most prominent change is one ESC and motor set for each nacelle to power each rotor. The turbine engines that were located in the XV-15 nacelles would then have to be placed in the fuselage alongside the generator and battery to make room for electric motors. The XV-15 transmission must also be completely changed due to the electric drive, eliminating the cross-shaft, but requiring a torque coupling device to combine power from both turbines into the same generator. A key asset of a fully electrically driven architecture is the direct connection between rotors and electric motors, enabling rapid and precise RPM control. Reliability concerns from the electric drive and efficiency losses from converting turbine power to electric power and then back to mechanical power are the main drawbacks of this configuration.

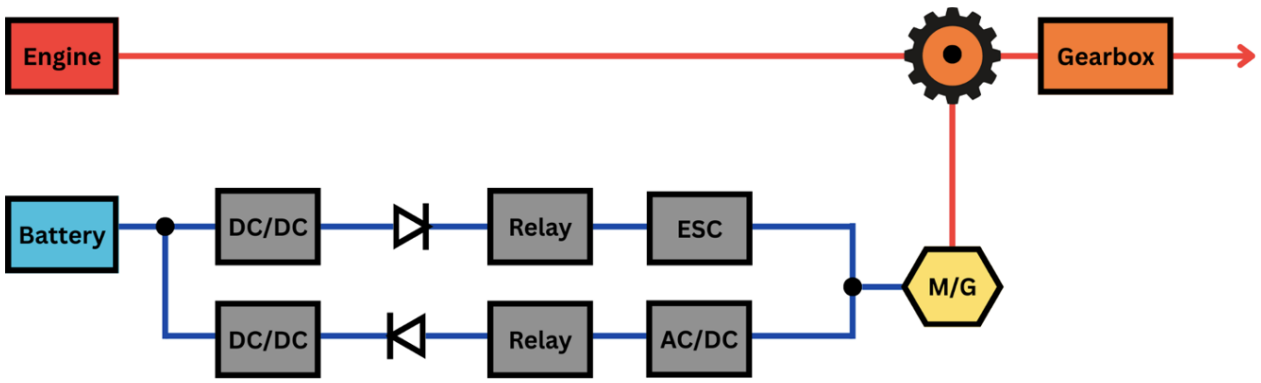


Figure 3.3: Block diagram of a parallel hybrid. M/G = motor/generator, ESC = electronic speed controller.

3.1.2 Parallel Hybrid

A parallel hybrid configuration retains most of the same components as a series hybrid, with a few key differences as shown in the block diagram in Fig. 3.3. There are still two branches, one for the engine and one for the battery. However, instead of converting mechanical power into electrical power, thermal engine shaft power is transmitted directly to the load through a set of torque coupling gears and an RPM reduction gearbox. The battery branch retains both paths for discharging and recharging with associated power electronics, except now all power out and in is converted either to or from mechanical power via a motor/generator component that performs both functions, labeled M/G. When discharging, the motor torque combines with engine torque through the torque coupling gears; when recharging, excess power is fed back into the motor which now acts as a generator.

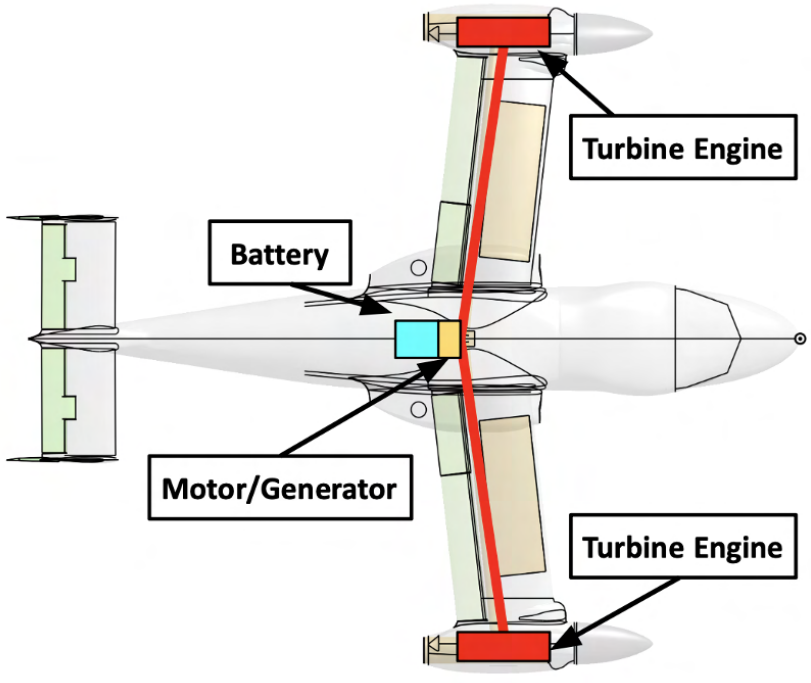


Figure 3.4: Notional sketch of a parallel hybrid in an XV-15 with a mechanical drive.

Figure 3.4 shows that *Hermes* would require only one motor/generator unit if using this architecture, with the turbine engines directly powering the rotors through gearboxes in the nacelles. This configuration would retain almost the exact same transmission and engine placement as the XV-15, including the cross-shaft. A torque coupling device must be included in the fuselage, except this would couple torque from the motor/generator unit to the cross-shaft. The battery would still be located in the fuselage to avoid changing the external geometry and adding weight to the nacelles. A key benefit of retaining a mechanical drive is that power loss from the turbine engines would be kept to a minimum. Also, since the XV-15 transmission would be largely unchanged, the hybrid propulsion system would be just as reliable as the XV-15 propulsion system. However, unlike the series architecture, the rotors would be driven by a direct mechanical connection to the turbine engines, so RPM control would be similar to that of the XV-15.

3.1.3 Combined Series-Parallel Hybrid Configuration

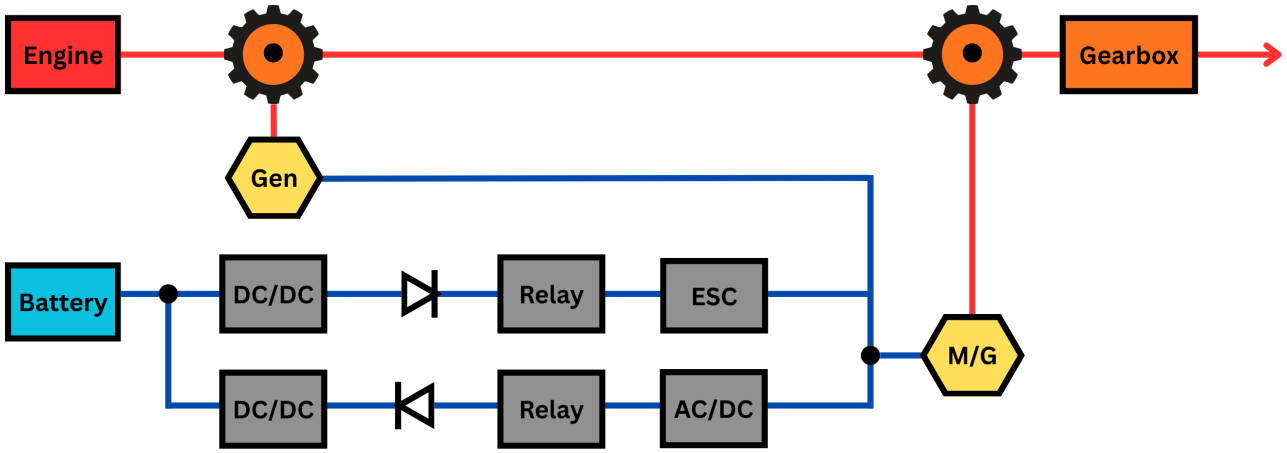


Figure 3.5: Block diagram of a combined series-parallel hybrid. Gen = generator, M/G = combined motor/generator unit, ESC = electronic speed controller.

Another possible hybrid architecture that combines all the components of both the series and parallel architectures is shown in Fig. 3.5. This allows for both electric and mechanical drives and keeps the advantages of each. This is accomplished through the use of an additional device similar to the torque coupling gears, but now engine torque would be split between generator and the mechanical transmission line. This increases the total number of components required for generating power compared to either series or parallel alone. Because minimizing weight is crucial in aviation, this architecture is discarded.

3.1.4 Architecture Comparisons

The main difference between the series and the parallel hybrid configurations is that series allows only for an electric drive, whereas parallel has a purely mechanical drive. An electric drive gives more flexibility in terms of rotor RPM control with much faster response times in contrast to changing turboshaft engine RPM. However, there is a higher loss of power on the engine branch in the series configuration because mechanical shaft power is converted to electrical power through the generator before being converted again to mechanical power through the motor. Even at a high efficiency of 95% for each of the four components between the engine and the load, that gives a total efficiency of only 81% on the engine branch. The parallel configuration, on the other hand, uses a mechanical drive directly from the engine to the load, so no turbine power is lost through conversion.

Another difference is the number of components and their weights. To accomplish the RFP mission,

Hermes requires more power beyond what the base XV-15 power plant can output. To avoid upscaling the existing T53 Lycoming turboshaft engines to provide this extra power, at least two turbines are still necessary regardless of the hybrid architecture chosen. The exact weights of the turbine engines, battery, motor/generator units, and other components scale with power and torque. Therefore, the power distribution between the turbine engines and the battery must first be calculated before weights can be compared against each other quantitatively for either configuration.

3.2 Hybrid Power Distribution Strategy

To calculate the weight of the turbine engines, battery, motor(s), and/or generator, the power provided by each component must first be known. In conventional hybrid vehicles such as hybrid automobiles, the power shared by the engine branch and battery branch at any given time is usually controlled by an optimization algorithm that minimizes fuel consumption at any given instant [11, 12]. However, the differences between driving an automobile and flying a tiltrotor are enough to warrant a new power distribution strategy fit for *Hermes*. In this new strategy, the goal is to minimize turbine engine weight by reducing the peak power it has to supply, while still minimizing fuel weight by operating at low SFC. Furthermore, flight missions are usually pre-determined with set hover, climb, cruise, and descent speeds and powers, which is in stark contrast to the more erratic driving cycles experienced by automobiles that encounter high variance in speed due to traffic and road signage. Therefore, the power distribution for flying *Hermes* can be solved ahead of time instead of being computed continuously mid-flight. The driving principles behind this power distribution strategy are given in the following section.

3.2.1 Power Distribution Principles

Starting from the power sources, both turbine engines are set to provide the same amount of power, adding to a total engine power P_E. The battery power, P_B, augments the engine power during the high power hover segments, represented by the following equation:

$$P_E + P_B = P_{hover}.$$

This ensures that the turbine engines do not need to provide the full power during hover, resulting in lower engine weights. In lower power segments such as cruise, the turbine engines are set to provide a power greater than that required by the rotors, with excess power P_r directed to recharge the battery, represented by the following equation:

$$P_E = P_{cruise} + P_r.$$

The battery is also used during cruise whenever it becomes fully charged to save engine fuel. The total amount of time the battery discharges, t_d, and the time it recharges, t_r, adds up to the total cruise duration, with the number of recharge cycles given by n_{cyc}, represented by the following equation:

$$n_{cyc} \cdot t_d + (n_{cyc} - 1) \cdot t_r = t_{cruise}.$$

Conservation of energy is used to constrain all free variables. The total amount of energy E_B provided by the battery in hover is equal to the amount of energy used to recharge the battery, which is constant. Thus:

$$E_B = P_r \cdot t_r = P_B \cdot t_{hover}.$$

P_{hover} and P_{cruise} will vary under different flight conditions, so a threshold power must be set to differentiate between high power and low power segments of flight.

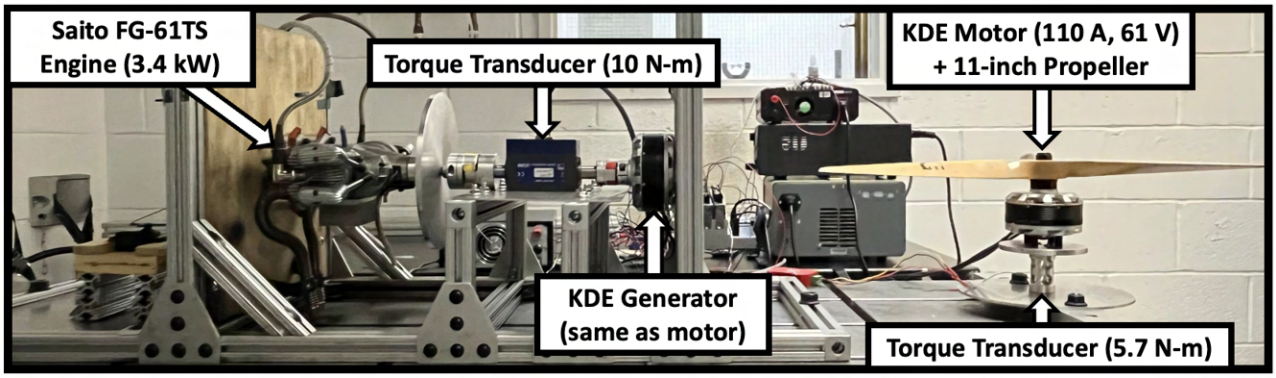


Figure 3.6: Hybrid and electric aviation test-bed, including the engine, motor, and various sensors.

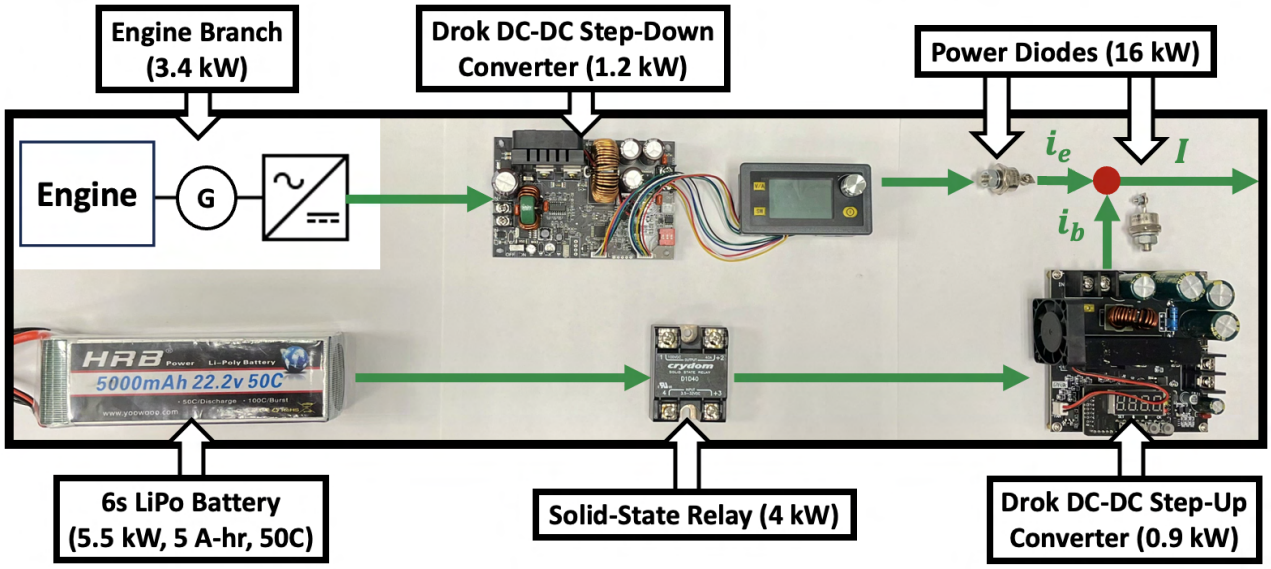


Figure 3.7: Battery-engine integration that combines power from both sources.

3.2.2 Experimental Validation

The hybrid power distribution strategy is a new, but crucial feature to operating *Hermes* at desired performance. To prove the feasibility of this strategy, detailed test data was acquired from an in-house hybrid and electric aviation test-bed, albeit at a small scale of 300 W (0.41 HP) peak power (Fig. 3.6). Specifically, a bench-top hybrid engine-battery test-bed was operated with a small-scale 4-stroke Saito FG-61TS combustion engine outputting mechanical shaft power that was combined with electrical DC power from a 5 Ah capacity, 6S cell voltage, 50/100C discharge/burst Li-Po battery. All components were selected with higher power ratings than what was used during testing to prevent overheating. The actual hardware used is shown in Fig. 3.6, and Fig. 3.7 shows the power electronics used in the battery branch of the hybrid test-bed. In Fig. 3.7, the engine branch (engine, generator, and passive AC-DC rectifier) is included as a block diagram to show how the engine and battery share power. The currents from the engine branch, i_e, and the battery branch, i_b, sum to the total current, I, delivered to the load. For recharging, a duplicate battery branch in reverse is included to direct current to the battery and not away from it. The test-bed uses a series hybrid configuration, but the power distribution strategy and power electronics would be the same if a parallel hybrid configuration was used instead.

In Fig. 3.8, the two driving principles of the hybrid power distribution strategy are demonstrated experi-

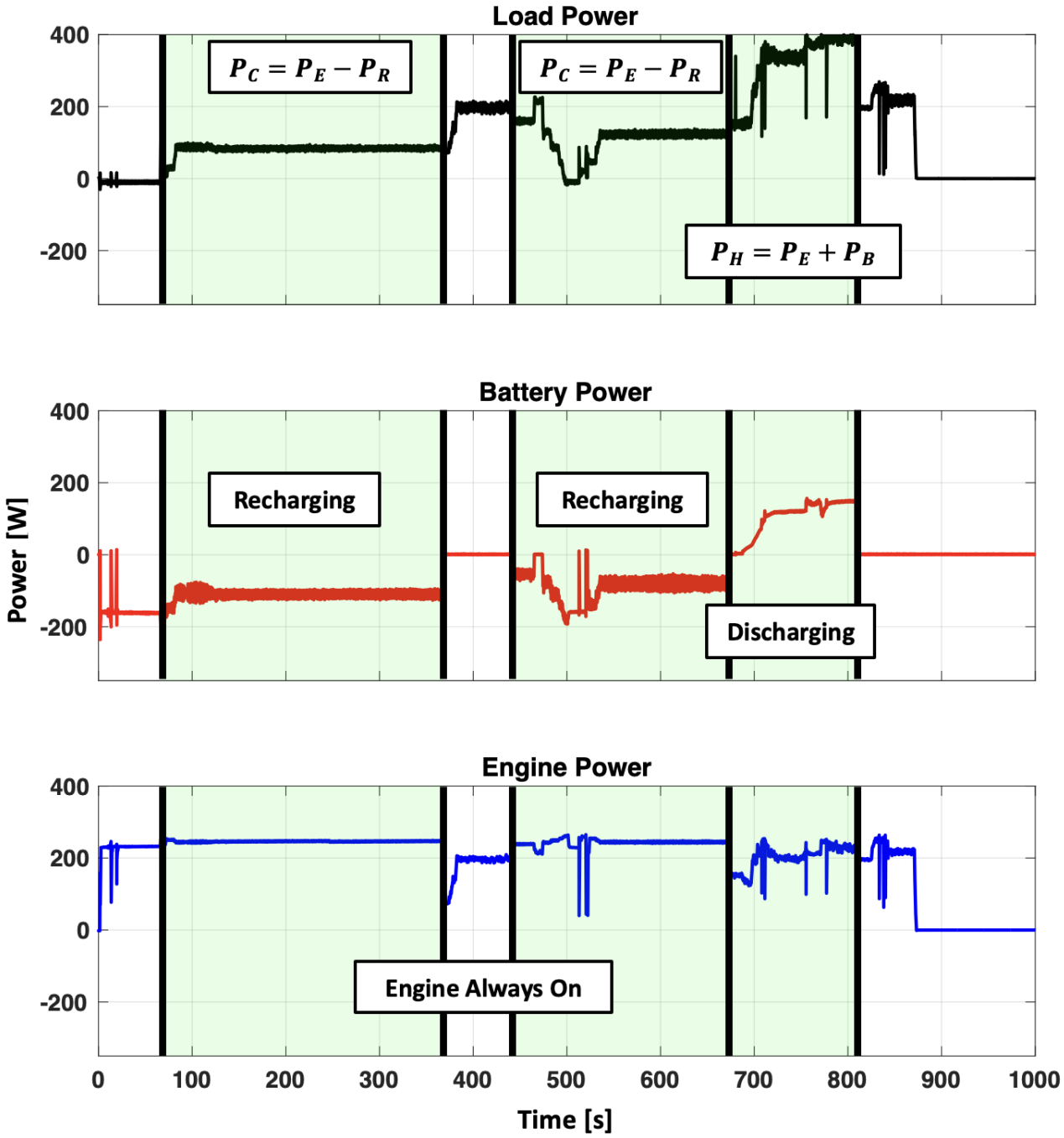


Figure 3.8: The core principles of the power distribution strategy with battery recharging are demonstrated in hardware. $P_C = P_{cruise}$ and $P_H = P_{hover}$

mentally. These principles are engine-battery power sharing in power intensive segments, simulating hover, and battery recharging in segments with lighter power requirements, simulating climb, cruise, and descent. There are three regions of interest in the test data in which all three of the load, battery, and engine are active at the same time. In the first region of interest (t = 75 - 375 s), the engine is held at a constant power level. At the same time, the engine is powering the rotor load and recharging the battery. All power lines are held at a steady state, simulating stable battery recharging during cruise. In the second region of interest (t = 440 - 675 s), the power required by the motor load is varied while the engine recharges the

battery. This allows more engine power to flow to the battery, recharging it at a faster rate than before, demonstrating the change in power distribution when transitioning between climb, cruise, and descent. In the third region of interest (t = 675 - 810 s), the power required from the rotor is increased while the battery is switched from recharging to discharging. Now, the engine power is supplemented by the battery power, simulating the power distribution required during hover. Any time outside of the three regions of interest, at least one of the three components, engine, battery, or rotor, is not in use.

The major conclusions from this experimental data are twofold. First, the power electronics outlined in the prior sections on hybrid architectures work as intended, enabling our power distribution strategy to discharge and recharge the battery when demanded. Since the power electronics are the same regardless of hybrid configuration, the power distribution strategy is also valid for any choice of hybrid configuration. Second, automatic control of the power electronics is necessary to ensure no loss of power. The test-bed was controlled manually, resulting in many instances of engine power loss whenever the engine RPM was not precisely tuned. Furthermore, there were three sets of actuators in the test-bed, one for engine RPM, one for rotor RPM, and one for switching the battery between discharge and recharge states. There are too many actuators to be monitored and controlled by the pilot in addition to the pre-existing flight actuators. Therefore, the power distribution strategy and power threshold must be pre-loaded onto the onboard flight computer to control the power electronics and reduce pilot workload. This also requires sensors to measure load power and battery power in real time so that the flight computer knows when the battery needs to augment engine power and when the battery needs to cycle between discharging and recharging.

3.2.3 Architecture Selection

Component	**Series**			**Parallel**		
	Quantity	**Unit Weight** kg (lb)	**Total Weight** kg (lb)	**Quantity**	**Unit Weight** kg (lb)	**Total Weight** kg (lb)
Turbine Engine	2	201 (444)	402 (888)	2	201 (444)	402 (888)
Fuel	-	-	790 (1740)	-	-	790 (1740)
Battery	1	141 (311)	141 (311)	1	141 (311)	141 (311)
Motor	2	274 (605)	549 (1210)	-	-	-
Generator	1	69 (152)	69 (152)	-	-	-
Motor/Generator	-	-	-	1	151 (332)	151 (332)
TOTAL	**6**	-	**1951 (4301)**	**4**	-	**1483 (3271)**

Table 3.1: Series hybrid and parallel hybrid weight breakdown

The full breakdown of the major components required for each configuration is shown in Table 3.1, along with a weight breakdown calculated by applying our power distribution strategy to the RFP mission. The power electronic components are the same regardless of configuration (DC/DC converters, AC/DC rectifier, and power diodes), so they are not included in this comparison. Table 3.1 shows that the series configuration weighs significantly more than the parallel configuration (almost 500 kg). This is due to the increased number of motor/generator units, with the motors in the nacelles having to be sized for rotor power which peaks in hover. In the parallel configuration, the motor is sized for peak battery power, which is significantly less than peak rotor power. Otherwise, turbine engine, battery, and fuel weight remain the same between configurations. This is due to holding the power distribution constant between both

configurations so that direct comparisons can be made across the same mission profile. These conclusions hold regardless of the number of discharge and recharge cycles used during cruise.

Overall, the increased weight penalty of having more than one motor/generator unit puts the series configuration at a major disadvantage to the parallel configuration. Therefore, the parallel configuration best suits *Hermes'* goal of minimizing empty weight.

3.3 Reliability

To assess reliability, the USAF Airworthiness Risk Assessment Matrix [13] was used. This matrix consists of six probability levels for four categories of failure severity as shown in Table **??**.

Probability Level	FR per FH	Catastrophic	Critical	Marginal	Negligible
Frequent	10^{-3} <P	1	3	7	13
Probable	10^{-4} <P<10^{-3}	2	5	9	16
Occasional	10^{-5} <P<10^{-4}	4	6	11	18
Remote	10^{-6} <P<10^{-5}	8	10	14	19
Improbable	10^{-6}>P	12	15	17	20

Table 3.2: USAF risk level matrix by severity and frequency

A failure mode never occurring is functionally impossible, so the matrix reduces to 20 different risk levels in ascending order from least acceptable to most acceptable. Risk levels 1-5 are high risk areas, 6-9 are serious risk areas, 10-17 are medium risk areas, and 18-20 are low risk areas. The practical reliability goal for a civil design is low risk, consisting of failures which are negligible in severity and improbable to occasional in frequency.

For a system where any component failure causes system failure, the system failure rate is governed by the equation $FR = 1 - \prod (1 - FR_n)$. If the failure rate is very small, this can be simplified to $FR = \sum FR_n$. For a system where all components must fail for the system to fail, the failure rate of the system is governed by the equation $FR = \prod FR_n$, or equivalently $FR = kFR_n$ for a system of k quantity of component n.

The components governing the failure rate for the series and parallel configurations are the engine (FR_E), generator (FR_G), motor (FR_M), gearbox (FR_{GB}), and cross-shaft (FR_X).

For the series architecture, if any component in either rotor subsystem fails, the system fails. This means the failure rate of the series architecture is:

$$FR_S = 1 - \left[1 - (1 - FR_E)(1 - FR_G)(1 - FR_M)(1 - FR_{GB})\right]^2 \tag{1}$$

which simplifies to:

$$FR_S = 2(FR_E + FR_G + FR_M + FR_{GB}) \tag{2}$$

For the parallel architecture to experience a system failure, either gearbox must fail, both engines must fail, or the cross-shaft and either engine must fail. The failure rate of the system is the sum of these three failure modes:

$$FR_P = FR_E^2 + \left[1 - (1 - FR_{GB})^2\right] + FR_X\left[1 - (1 - FR_E)^2\right] \tag{3}$$

This can be simplified to:

$$FR_P = FR_E^2 + 2FR_{GB} + 2FR_X FR_E \tag{4}$$

Two of the three failure modes for the parallel architecture are higher order terms, making the reliability of the parallel architecture primarily a function of the gearbox reliability. Thus, the parallel architecture has the additional advantage that reliability can be improved just by designing the gearbox to higher standards, while the series architecture requires improving the reliability of every propulsion component to improve the system reliability.

Engine reliability data for the T53 is drawn from a 1974 engine experience report [14], which summarizes 2,614 recorded incidents caused by T53 engine failures across 7.4 million flight hours accumulated between 1970 and 1974.

The failure rate of the engine in each severity category was calculated as the quotient of mishaps in that category and the total flight hours. The number of recorded incidents in each category, both non-cumulative and cumulative, along with associated failure rates are given by table 3.3. Failure rates for the generator, motor, gearbox, cross-shaft, and battery were taken from a NASA report on the safety of urban air mobility concept vehicles [15]. These components generally failed between every 1 million and 10 million hours, but specific failure rates for components used in our hybrid architecture are given in Table 3.4. Failure rates for each severity level were calculated using the appropriate series or parallel system equation and the failure rates for individual components. Each severity category then had its frequency classified into one of the six frequency ranges specified by the USAF matrix. Finally, a Risk Assessment Code (RAC) was assigned to each severity level for the hybrid and parallel architectures, and the worst (lowest) RAC for that architecture was taken as the system's RAC when assessing the overall risk level. This process is detailed in Table 3.5.

Severity	**N**	ΣN	**Rate (R)**
Catastrophic	140	140	1.9E-05
Critical	181	321	4.3E-05
Marginal	763	1084	1.5E-04
Negligible	1530	2614	3.5E-04

Table 3.3: Engine reliability over 7.4 million flight hours

For the series architecture, catastrophic failure occurs about 5 times per 10^5 flight hours, placing it in the high risk category. For the parallel architecture, catastrophic failure occurs about 8 times per 10^7 flight hours, placing it in the medium risk category. The parallel architecture provides a nearly 100-fold improvement in reliability, and achieves the highest RAC score possible short of eliminating the risk of catastrophic failure entirely.

Component	**Failure Rate Per Flight Hour**
Generator	4.30E-06
Motor	9.24E-07
Gearbox	4.23E-07
cross-shaft	7.15E-07
Battery	5.61E-06

Table 3.4: Component reliability breakdown

The complete elimination of a risk as complex as the propulsion system is impractical or even impossible

to achieve, but the parallel architecture comes by far the closest. The parallel architecture provides the most efficient means to further reduce risk by improving the gearbox, while the series architecture requires improvement of every component in the system for the same effect. The series architecture has an unacceptably high risk level and would require significant sacrifices in requirements (customer accepting frequent catastrophes), weight (making all components redundant), or maintenance costs (substantially more frequent upkeep) to be an adequate solution. For this reason, the parallel architecture has a very clear and substantial advantage when it comes to reliability of the propulsion system.

	Series	**Parallel**
Catastrophic FR	4.91E-5	8.46E-7
Catastrophic RAC	4	12
Critical FR	9.80E-5	8.48E-7
Critical RAC	6	15
Marginal FR	3.04E-4	8.68E-7
Marginal RAC	9	17
Negligible FR	7.17E-4	9.71E-7
Negligible RAC	16	20
Minimum RAC	4	12

Table 3.5: RAC levels for series and parallel configurations

3.4 Hybrid Vehicle Sizing

The selected parallel hybrid architecture uses a mechanical drive, so there is no electrically distributed propulsion. As such, to fulfill RFP requirements, at least 10% power must come from electrically generated sources, i.e. a battery. This section outlines a refined sizing and battery charging/recharging strategy.

The hybrid sizing procedure follows the flowchart shown in Fig. 3.9. The procedure begins by initializing fixed parameters defined in the RFP and parameterizing several design variables for hybrid sizing. A BEMT-based whole-vehicle trim solver was utilized to determine the power required for each segment of the mission and the associated fuel consumption. A new empty weight is then calculated considering the modifications required to actualize the hybrid architecture. A configuration is selected to minimize empty weight as outlined in the RFP and maintain manageable C-rates for the battery to reduce degradation and cooling needs.

The sizing procedure examined multiple hybrid configurations with different combinations of battery sizes, engine quantity, and operating procedures.

The configurations are listed as follows:

1. One engine, one battery and motor (1E)
2. Two engines, one battery and motor, engine cycling on and off during cruise (2E)
3. Three engines, one battery and motor, additional engine cycling on and off during cruise (3E)
4. Two engines, one battery and motor, engine throttling during cruise (2E-T)

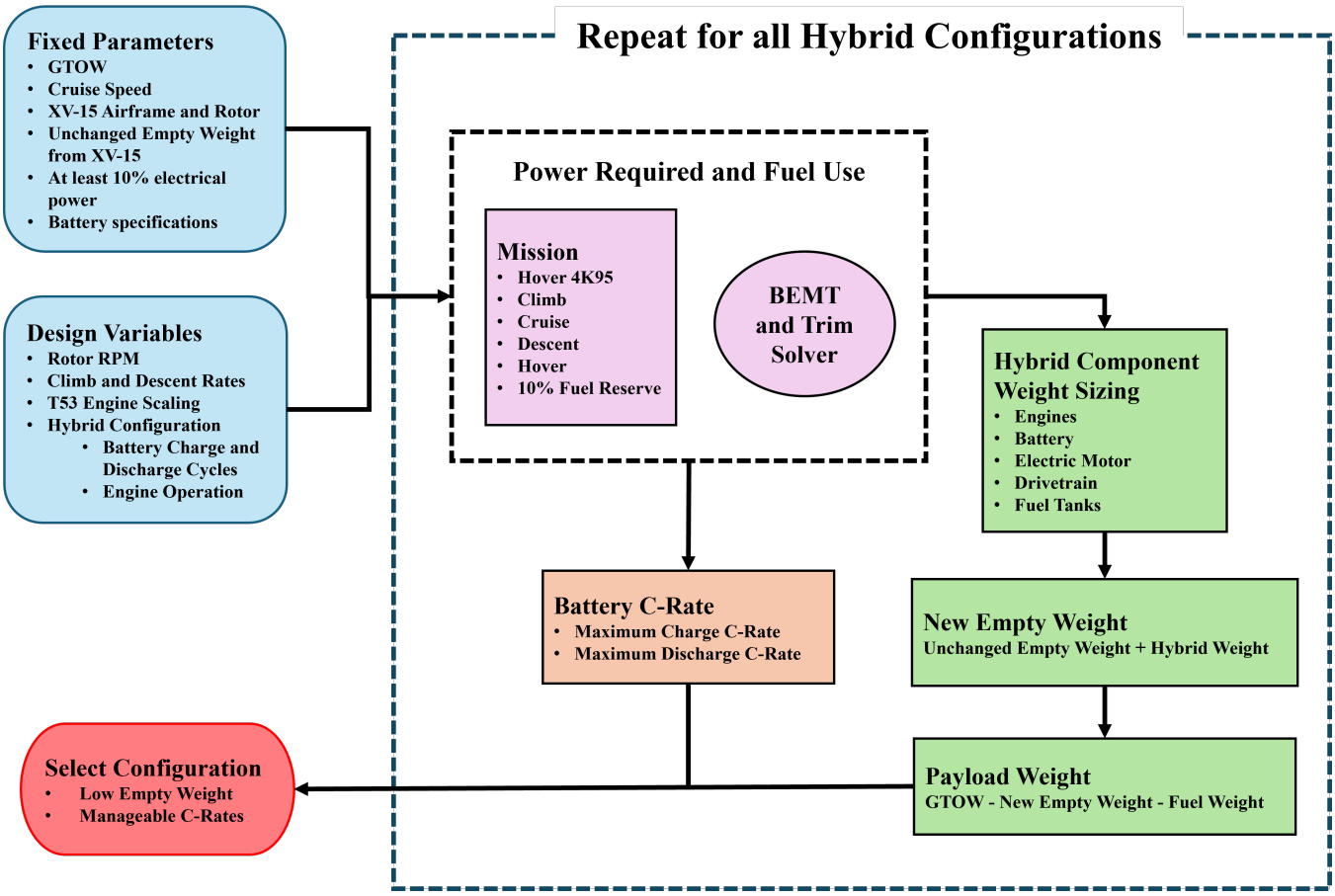


Figure 3.9: Flowchart for hybrid configuration sizing and selection procedure.

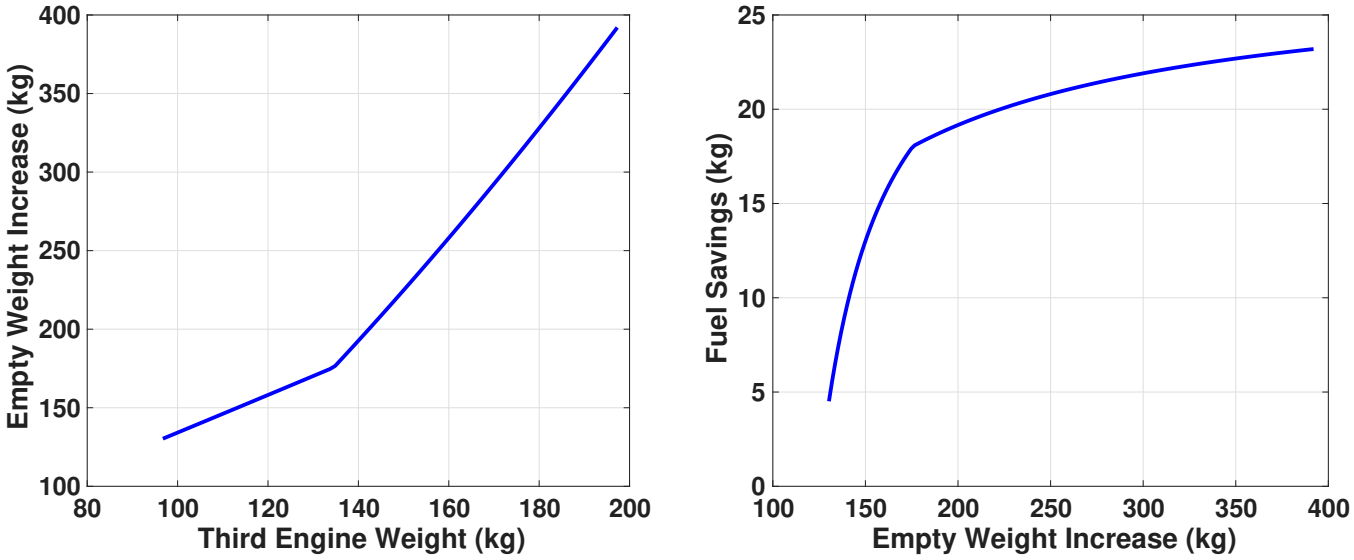
Configurations 2E, 3E, and 2E-T all utilize multiple engines to meet hover power demands, leaving excess installed power in cruise. Configurations 2E and 3E manage this surplus by cycling engines on and off during cruise to charge the battery, while configuration 2E-T instead throttles both engines continuously to modulate battery charging and discharging. Configuration 1E, by contrast, carries only a single engine and must rely on a substantially larger battery to supplement hover and cruise power.

The T53 engines each have a maximum rated power (MRP) of 698 kW (936 HP) at 1,219 m / 35°C (4,000 ft / 95°F or 4K/95 in short), atmospheric conditions. Furthermore, in airplane mode, the T53 engines supply a maximum continuous power (MCP) of 783 kW (1,050 HP) each at an airspeed of 156 m/s (303 kt) and 3,048 m (10,000 ft) altitude. These power limitations significantly affected the configuration selection. The power required to hover out of ground effect at 4K/95 conditions for a gross weight of 5,897 kg (13,000 lb) is 1,576 kW (2,113 HP) which necessitates an additional 180 kW (241 HP) from electrical sources. The RFP does not permit modifications to the airframe, rotor, and gross weight, which would reduce this hovering power, so configurations had to address this high power need.

Configuration 1E cannot provide the necessary power to complete the initial hover and high-speed cruise segments without adding considerable battery and motor weight, therefore substantially increasing empty weight. At minimum, the battery must provide 878 kW (1,177 HP) to hover and at least 875 kWh of energy over the course of the mission. At the given power density of 2.5 kW/kg, the battery would weigh 351 kg (774 lb). However, the energy density is 250 kWh/kg, so to meet the energy demand from the mission, the battery must weigh at least 3,500 kg (7,716 lb). Recharging the battery during the mission is not possible for this configuration. Configuration 1E is not selected for *Hermes*.

Configuration 2E operates the engines at MCP, corresponding to lowest specific fuel consumption. During periods where one engine is turned off in cruise, a battery and electric motor must provide the power. For a battery and electric motor that provides the power of a T53 engine, the empty weight increases by 422 kg (931 lb) and only saves 58 kg (128 lb) of fuel for moderate charging and discharging C-rates. The C-rate describes how quickly a battery is charged or discharged relative to its capacity, where high C-rates generate excessive heat and accelerate battery degradation. Due to the large increase in empty weight, configuration 2E is not chosen.

Configuration 3E utilizes three engines with two engines providing the majority of required power while a third engine cycles on and off during cruise. While turned off, the battery and electric motor provide the power required in cruise. This again allows all three engines to operate at MCP whenever on. Two T53 engines operating at MCP exceed the required cruise power of 1397 kW (1873 HP), so a three engine setup would require all engines to be downscaled to always operate at MCP. To fulfill the 10% electrical power requirement, the two downscaled engines output at an MCP of 629 kW (855 HP) each and the third smaller engine provides at least 140 kW (187 HP) of power. The size of the third engine increases as the desired battery power and recharge rates increase. The third engine and battery must provide the same amount of power to cruise, and higher recharge rates increase the excess power needed from the engine. Fig. 3.10(a) shows the empty weight growth for varied third engine sizes. As expected, increasing the size of the third engine increases the overall empty weight. The amount of fuel saved over the entire mission is an order of magnitude less than the empty weight growth as shown in Fig. 3.10(b). This configuration is not selected due to the sizable increase in empty weight and the added complexity of a third engine.



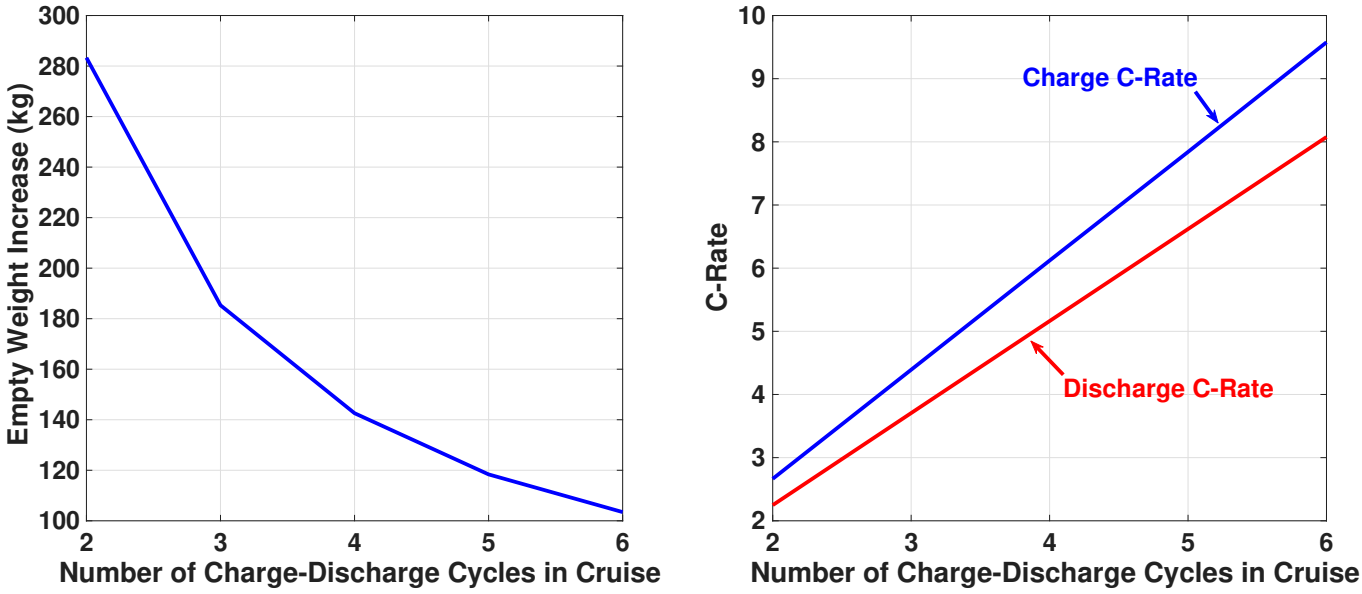
(a) Empty weight growth for a selected third engine size

(b) Fuel savings from empty weight growth

Figure 3.10: Three engine configuration (3E) analysis.

Configuration 2E-T relies upon two T53 engines, the same ones used on the XV-15, but throttles them up and down to charge and discharge a battery. The battery is recharged and discharged several times throughout the cruising segment of the mission. Figure 3.11(a) shows empty weight growth from the hybrid propulsion components, engines, battery, and motor, for a set number, N, of recharge/discharge cycles. Because the battery recharges during the climb segment, the cruise segment begins and ends with the battery discharging. As such, the battery discharges N times and recharges N-1 times. The weight of the hybrid components substantially decreases as the number of cycles increase at the cost of higher C-rates. Two T53 engines output a cumulative MCP of 1,566 kW (2,100 HP) which provides an excess of

169 kW (230 HP). Increasing the number of charge/discharge cycles raises the amount of time the battery charges and discharges per cycle as the cruise segment has a fixed flight time of one hour. This decreases the energy capacity needed from the battery. Fuel weight is not considered because the RFP desires minimal empty weight growth. Figure 3.11(b) shows the recharge and discharge C-rates of the battery for a varied number of recharge/discharge cycles in cruise. C-rate increases linearly with the number of cycles. Configuration 2E-T is selected for its low empty weight growth and overall simplicity. The final 2E-T configuration balances weight with C-rate by selecting five recharge/discharge cycles to reduce weight as much as possible while also ensuring manageable C-rates for safe and reliable battery operation throughout the mission. The associated weight increase for the propulsive components is approximately 120 kg (265 lb).



(a) Empty weight sizing for varying recharge/discharge cycles during cruise

(b) C-rates for varying recharge/discharge cycles during cruise

Figure 3.11: Sizing the two throttled engines configuration (2E-T).

3.5 Motor Selection

The choice of motor for *Hermes* was primarily guided by two key requirements: fulfilling the 180 kW (241 HP) continuous power requirement in the initial hover segment and achieving a high specific power and torque to keep weight at a minimum. Three motors were evaluated: The Yasa YM720, Evolito D250 and H3X HPDM-180R. The Yasa YM720 delivers 180 kW (241 HP) with a mass of 33 kg (73 lb), resulting in a specific power of 5.45 kW/kg. In contrast, the Evolito D250 is capable of 207 kW (278 HP) with a much lower mass of 13 kg (29 lb), resulting in a specific power of 15.9 kW/kg. The H3X HPDM-180R provides the same 180 kW (241 HP) output as the YM720 but at a much lower mass of 12.3 kg (27 lb), resulting in a specific power of 13.9 kW/kg. Operating at 180 kW (241 HP), the HPDM-180R rotates at 20,000 RPM, corresponding to a maximum continuous torque of 86 N-m (63.4 lb-ft). A significant advantage of the HPDM-180R is its integrated inverter and reduction gearbox, which substantially reduces total system weight compared to the YM720 and D250, where these would be separate additions. Furthermore, the integrated reduction gearbox enables the high-speed HPDM-180R motor to produce greater torque than the YM720. HPDM-180R can also be used as a motor and generator, suiting the exact needs for *Hermes'* parallel hybrid architecture. The H3X HPDM-180R was selected for *Hermes* as it balances power,

integration simplicity, and weight.

3.6 Battery

The battery needs a capacity of 21.6 kWh to provide sufficient power for the RFP mission. Per the calculated capacity and the RFP guidelines, the battery mass is set at 86.4 kg (191 lb). To achieve a mechanical power output of 180 kW (241 HP), the battery must deliver 196 kW (262 HP) of electric power, accounting for the motor's efficiency losses ranging from 92% to 94%.

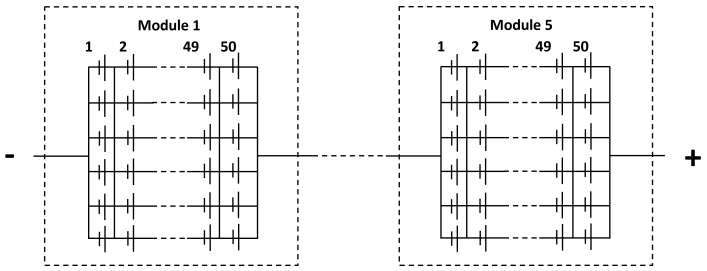


Figure 3.12: *Hermes* battery pack design.

The battery capacity of 21.6 kWh is sized such that a maximum of 80% of the total energy is utilized during the mission for any given charge cycle, preserving battery health and extending cycle life over the operational lifetime of the aircraft. The battery experiences the highest load in hover where the motor draws 194 kW of power, resulting in a discharge rate of 9.0C. The battery recharges during the cruise segment of the mission at a rate of 7.8C. The weight of the power electronics needed to cycle the battery between discharging and recharging is included under battery accessories in Section 20 .

Multiple battery types were examined for this mission: Nickel Manganese Cobalt (NMC), Lithium Iron Phosphate (LFP), and Nickel Cobalt Aluminum Oxide (NCA). The NCA chemistry was the only chemistry to meet the high discharge rate at a maximum of 7-16C [16], while also being able to operate at high temperatures and falling in the range of energy density stated in the RFP. The extensive operational history of this chemistry within electric vehicles provides validation of its performance, establishing it as a mature technology for this mission.

A 21700 NCA cell has a nominal voltage of 3.6 V and capacity of 4 Ah, the system configuration consists of a 250S6P pack. This pack is organized into five 50S6P modules to simplify the manufacturing process (Fig. 3.12). Each module is enclosed in a CS-29.1353-compliant casing to prevent hazardous gas leakage. Battery specifications are summarized in Table 3.6.

Table 3.6: *Hermes* Battery specifications: cell, module, and pack

(a) Cell		(b) Module		(c) Pack	
Nominal Voltage	3.6 V	Cells/Group	6	Total Modules	5
Capacity	4 Ah	Groups/Series	50	Total Cells	1500
Maximum Discharge Rate	16 C	Cells/Module	300	Nominal Voltage	900 V
Cathode	NCA	Nominal Voltage	180 V	Capacity	24 Ah
		Capacity	24 Ah	Mass	86.4 kg
		Energy	4.34 kWh	Energy	21.6 kWh
				Energy Density	250 Wh/kg
				Power Density	2500 W/kg

3.6.1 Battery Management System

A battery management system (BMS) is mandatory for battery operation. The BMS is engineered to handle the specific stressors of a 194 kW (264 HP) output, 9.0C discharge rate, and a 7.8C charge rate. The BMS continuously monitors individual cell voltages to ensure uniform discharge across the battery pack, preventing the over-discharge of any single cell during the 9.0C high-power draw. By tracking temperatures at multiple locations, the BMS detects early signs of thermal runaway, which is critical given the significant heat generated by the high discharge rates and the 4 charge cycles at 7.8C. This thermal monitoring ensures compliance with CS-29.1353 requirements, mandating an automatic shutdown if temperatures exceed critical thresholds to protect the aircraft and crew. By maintaining these operational boundaries, the BMS preserves long-term battery health despite the demanding mission requirements.

3.7 Battery and Motor Cooling

A comprehensive cooling system is required to maintain reasonable battery and motor temperatures, especially during the initial hover segment when the ambient air temperature is 35°C (95°F). Combined with the high power draw from the motor and battery, the cooling requirement is largest this mission segment. At peak continuous output in hover, the battery and electric motor produce 43.5 kW of heat. *Hermes* must maintain a battery operating temperature no more than 70°C (158°F) as limited by the NCA battery type. The motor is limited to an operating temperature of 60°C (140°F). The operating conditions as well as the cooling system components are outlined in Table 3.7.

Table 3.7: *Hermes* Cooling System

Components		**Value**	
Peak Waste Heat		43.5 kW	150000 BTU/hr
Battery Temperature Limit		70°C	158°F
Motor Temperature Limit		60°C	140°F
Radiator			
	Weight	4.5 kg	9.9 lb
	Material	Aluminum	
Fan			
	Weight	10.9 kg	24 lb
	Power	250 W	0.33 HP
	Flow Rate	1.39 m^3/s	2940 CFM
Coolant		De-ionized Water	
	Weight	8 kg	17.6 lb
	Pump Flow Rate	37.7 L/min	9.9 gal/min
	Pump Pressure	150 kPa	21.8 psi
	Pump Power	440 W	0.6 HP

The cooling system is closed-loop and liquid cooled, servicing the battery and motor. The complete setup is shown in Fig. 3.13 with the battery and motor connected in parallel. The coolant discharging from the pump splits through a Y-fitting and flows to the motor and battery separately. Another Y-fitting merges

the coolant pipes after exiting the motor and battery. Inside the battery casing, the coolant is delivered through internal coolant pipes interwoven between cells to maximize heat removal. The radiator, fan, and coolant pump are sized to remove 43.5 kW of heat. De-ionized water is selected as coolant because it is electrical insulating. With a specific heat of 4.18 kJ kg^{-1} K^{-1}, the water flow rate must be at least 37.7 L/min (9.9 gal/min) to not exceed the operating temperatures of the battery and motor. This flow rate is delivered by an AMT 3682 centrifugal pump at a pressure of 150 kPa (21.8 psi), circulating the coolant in 6.5 seconds. The pump operates at 3000 RPM and is connected to the central gearbox to receive power from the engines and motor. An aluminum tube-and-fin heat exchanger is used as the radiator with a volume of 270 mm × 270 mm × 25 mm. A Sparrow PF181V fan supplies 1.39 m^3/s (2,940 CFM) of air to the radiator and is powered by an independent motor. A large quantity of air is required due to the high ambient temperature reducing the effectiveness of cooling.

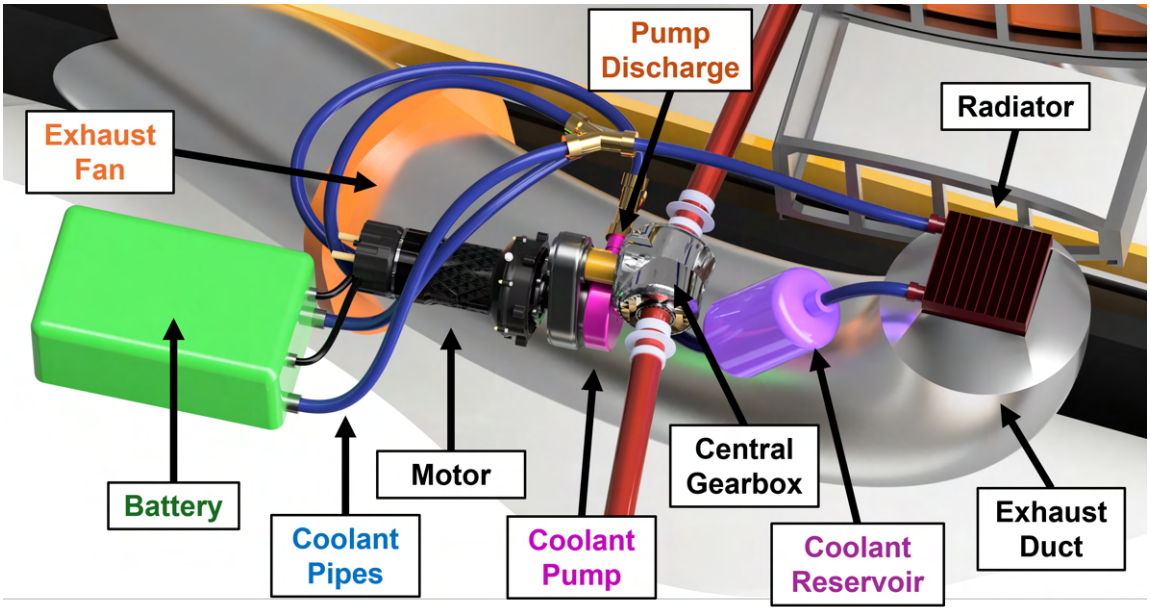


Figure 3.13: *Hermes* cooling system.

3.8 Fuel System

The XV-15 has a fuel system with a combined capacity of 684 kg (1509 lb) across four interconnected fuel tanks, with two per wing [17]. Each fuel tank is made of a flexible bladder and connected to each of the other fuel tanks through a network of pipes and valves. This fuel system has multiple redundancies built in for improved reliability. Gravity and pressure feed lines can feed any engine from any tank in case of emergency, and in case of boost pump failure, the backup engine-driven pump can keep pumping fuel up to altitudes of 3,048 m (10,000 ft).

Due to the appropriate fuel system of the XV-15, the only change in the fuel system for *Hermes* is the total fuel capacity. A new fuel tank with a volume of 98 liters (26 gal) is added per wing in the empty space between the third and the fourth ribs, labeled as fuel tank 3 and colored orange in Fig. 3.14. This extra fuel tank in each wing adds a total of 158.8 kg (350 lb) of extra fuel capacity, giving *Hermes* the range to complete the RFP mission whereas the XV-15 could not.

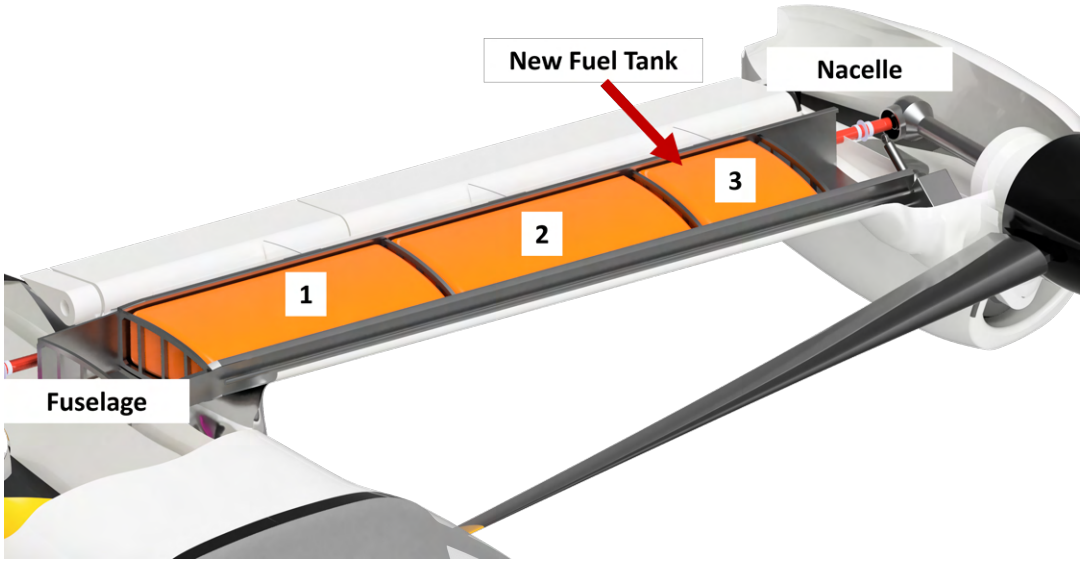


Figure 3.14: *Hermes* fuel bladders (orange) in the left wing.

3.9 Mission Configuration

The operating conditions of the mission for *Hermes* is defined in Table 3.8. In total, 834 kg (1839 lb) of fuel is required to fulfill the RFP mission spanning a total of 91.3 minutes. *Hermes* begins the mission at 5897 kg (13000 lb) and expends 751 kg (1655 lb) of fuel before landing at the end of the mission. An additional 10% fuel reserve, 83 kg (184 lb) is carried by *Hermes*.

Mission Segment	**Atmospheric Conditions**	**Time**	**Speed**	**Power Required**	**Fuel Use**
		min	m/s (kt)	kW (HP)	kg (lb)
HOGE	1219 m / 35°C 4000 ft / 95°F	5	0	1576 (2113)	56 (124)
Climb	ISA	10.6	51 (100)	760 (1019)	56 (123)
Cruise	ISA 3048 m / 10000 ft	60.7	155 (303)	1397 (1873)	550 (1212)
Descent	ISA	10	51 (100)	450 (604)	37 (81)
HOGE	ISA Sea Level	5	0	1302 (1746)	52 (115)
Reserve	-	-	-	-	83 (184)
Total	-	91.3	-	-	834 (1839)

Table 3.8: Mission parameters for *Hermes*

Battery usage during the mission is outlined in Table 3.9. The mission requires discharging the battery during the initial hover segment, five times in cruise, and during the final hover segment. The battery is also recharged during climb, four times in cruise, and during descent when surplus power from the engines is used to charge the battery. The T53 engines each supply an MRP of 698 kW (936 HP) under 4K/95 atmospheric conditions, so to complete the initial hover segment, the battery must supply 180 kW (241 HP) after efficiency losses. The engine output in the climb, cruise, and descent segments is set to MCP. The climb segment is completed in 10.6 minutes and utilizes only one engine throttled to MCP, idling the other

engine, to minimize fuel consumption while also recharging the battery. The cruise segment fulfills the 10% electrical power usage dictated in the RFP by throttling the engine down from the MCP at 3,048 m (10,000 ft) altitude of 783 kW (1,050 HP) to 627 kW (842 HP), a 24.6% reduction, and discharging the battery at 140 kW (190 HP). Operating the engines at MCP, 12% above cruising power, the battery recharges with 169 kW (230 HP) of excess power. The descent segment recharges the battery for the final hover segment. The engines are able to provide the required power for the final hover segment, and doing so would forgo the need to recharge the battery during descent. However, using the battery reduces the overall mission fuel consumption. The state of charge shown in Table 3.9 is the charge percentage at the end of each segment. The distribution of power required, operating power for the engine, and battery use is illustrated in Fig. 3.15.

Mission Segment	**Time per Cycle**	**Number of Cycles**	**C-Rate**	**Battery Power**	**Power Share Ratio**	**State of Charge**
	min			kW (HP)	%	%
HOGE, Discharge	5	1	9.0	180 (241)	11	25
Climb, Charge	10.6	1	3.9	85 (115)	11	100
Cruise, Charge	6.0	4	7.8	169 (230)	11	100
Cruise, Discharge	7.3	5	6.9	140 (190)	10	16
Descent, Charge	10	1	4.7	102 (139)	23	100
HOGE, Discharge	5	1	9.0	180 (241)	14	25

Table 3.9: *Hermes* battery usage during the mission.

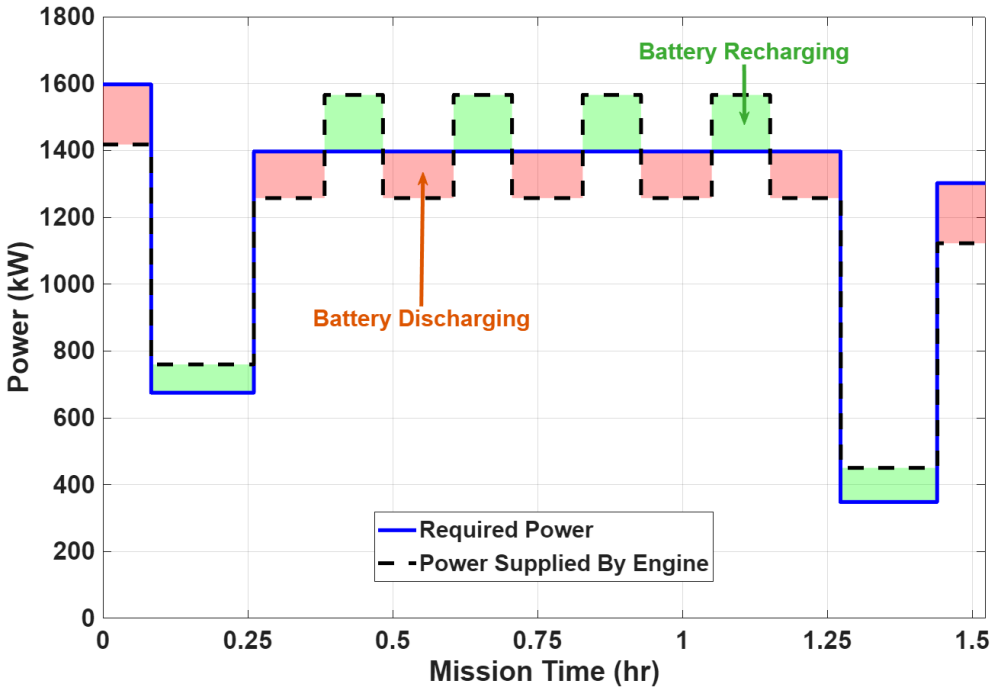


Figure 3.15: *Hermes* mission power required and power supplied from the engines.

4 Hermes Drive System

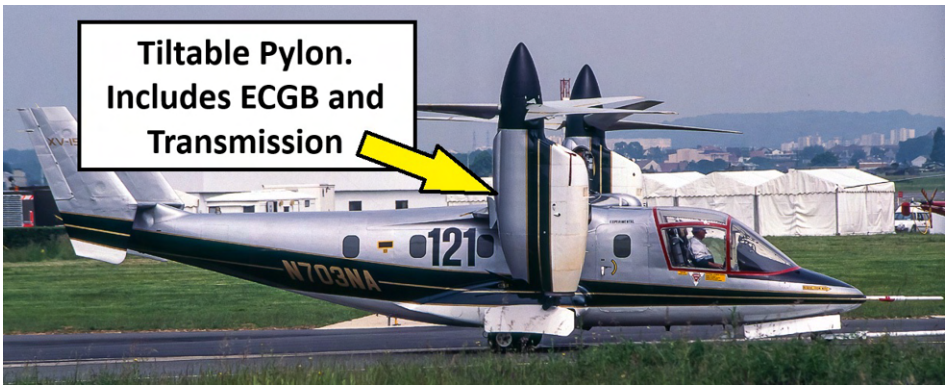


Figure 4.1: XV-15 preparing for takeoff.

Figure 4.1 shows a view of the XV-15 in hover configuration. The XV-15 has two pylons at the wingtips that can be tilted from 0° (airplane mode) up to 95° (helicopter mode). An innovation of the Bell tiltrotor designs (Model 300, XV-15, etc.) was to include the engine and transmission in the tiltable pylon. The XV-15 uses the Lycoming T53-LTC1K-4K turboshaft engine, but the same transmission as the Model 300 aircraft (which used the Pratt and Whitney PT-6 engine). Since the PT-6 output drive shaft operated at 30,000 RPM (at hover) and the LTC1K-4K output speed is about 22,000 RPM, an "engine-coupling gearbox" (ECGB) was required in the XV-15 for using the Model 300 main transmission [18]. This ECGB increases the engine output RPM to match the higher input speed of the Model 300 main gearbox.

The hybridization implemented in the *Hermes* gave an opportunity to redesign the pylon and its contents. The designs are presented in the following subsections as follows: first, the baseline drive system of the XV-15 is described, followed by the description of the *Hermes* transmission.

4.1 Baseline XV-15 Drive System

Figure 4.2 shows a schematic of the XV-15 drive system [17]. The output of the Lycoming T53 engine (about 22,000 RPM) is first increased to 30,000 RPM using the ECGB. The rest of the transmission reduces this RPM to the design rotor shaft speed of 565 RPM (53:1 reduction ratio) in three stages consisting of two spur gear stages and two planetary stages. Although, the design XV-15 hover rotor speed was 565 RPM [17], improved maximum gross weight was possible with a higher hover RPM. The rotor speeds flown on the XV-15 were 589 RPM in hover and 517 RPM in cruise.

In addition to this, the first reduction stage also powers a cross-shaft that enables single-engine flight capability by allowing one engine to drive both proprotors. The cross-shafts of the port and starboard engines are connected through a center gearbox using a pair of bevel gears. The center gearbox accommodates the direction change required by the cross-shafts to accommodate the forward sweep and dihedral of the wings.

At the design gross weight of 5900 kg (13,000 lb), the XV-15 is too heavy to hover on one engine, but it has demonstrated that it can maintain altitude in forward flight. When both engines are working, the cross-shaft is kept rotating, and only comes into action when one of the engines fails (OEI condition).

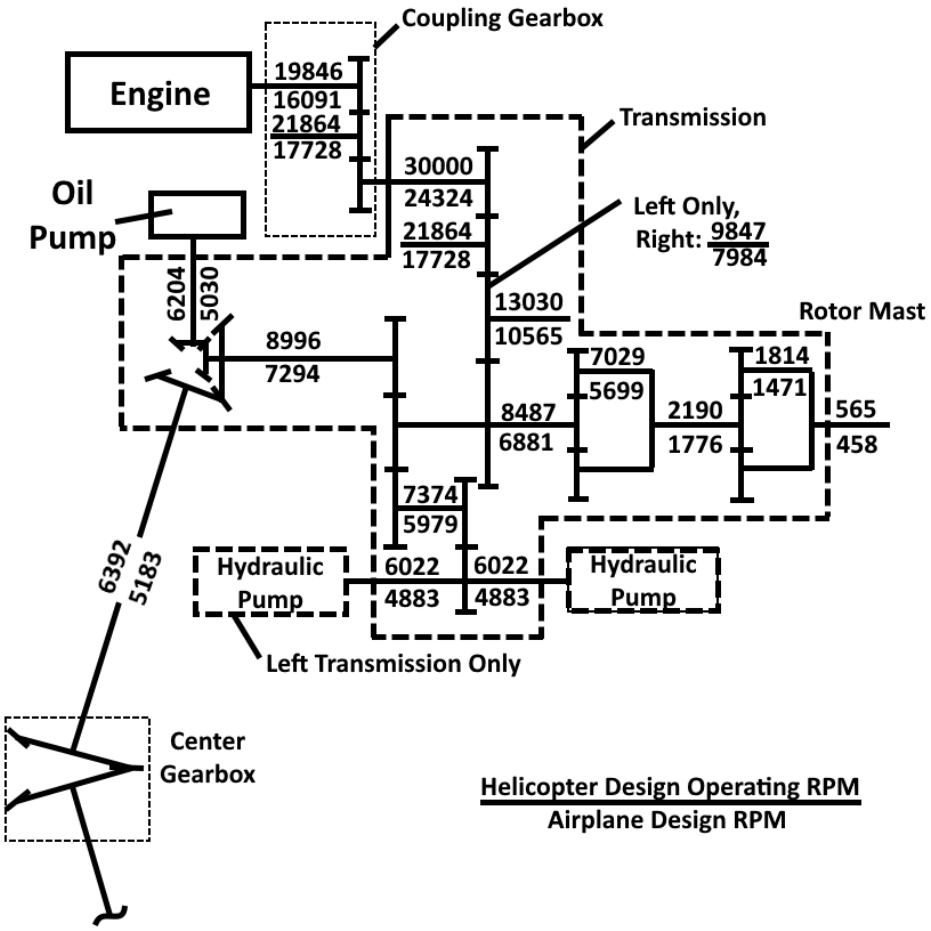


Figure 4.2: Unmodified XV-15 drive system.

4.2 *Hermes* Drive System

The drive system of *Hermes*, shown in Table 4.1 and Fig. 4.3, is a simplified version of the XV-15 drive system and includes the modifications required to accommodate the hybridization components. The ECGB is eliminated, and the output of the T53 LTC1K-4K engine (20,000 RPM) is used without any modification to the transmission. This makes the design of the main transmission more compact (Fig. 4.4). The motor input is fed into the center gearbox.

4.3 Gear Sizing

The sizing of the transmission gear train is an iterative process driven by the required speed reduction and the torque transmitted at each stage. Gear geometry is primarily dictated by two parameters: the number of teeth and the gear module. The ratio between the meshing gears is established by the rotational speed reduction desired and the ratio of their respective tooth counts. The gear module governs the physical dimensions of the teeth and consequently the ability to withstand the applied contact and root bending loads felt on the teeth.

The overall transmission ratio is dictated by the rotational output of the engine, 20,000 RPM, and the required 589 RPM at the rotor in hover, resulting in a required reduction ratio of 35.4:1. This reduction is distributed across multiple gear stages within the nacelle to achieve the desired rotor speed while main-

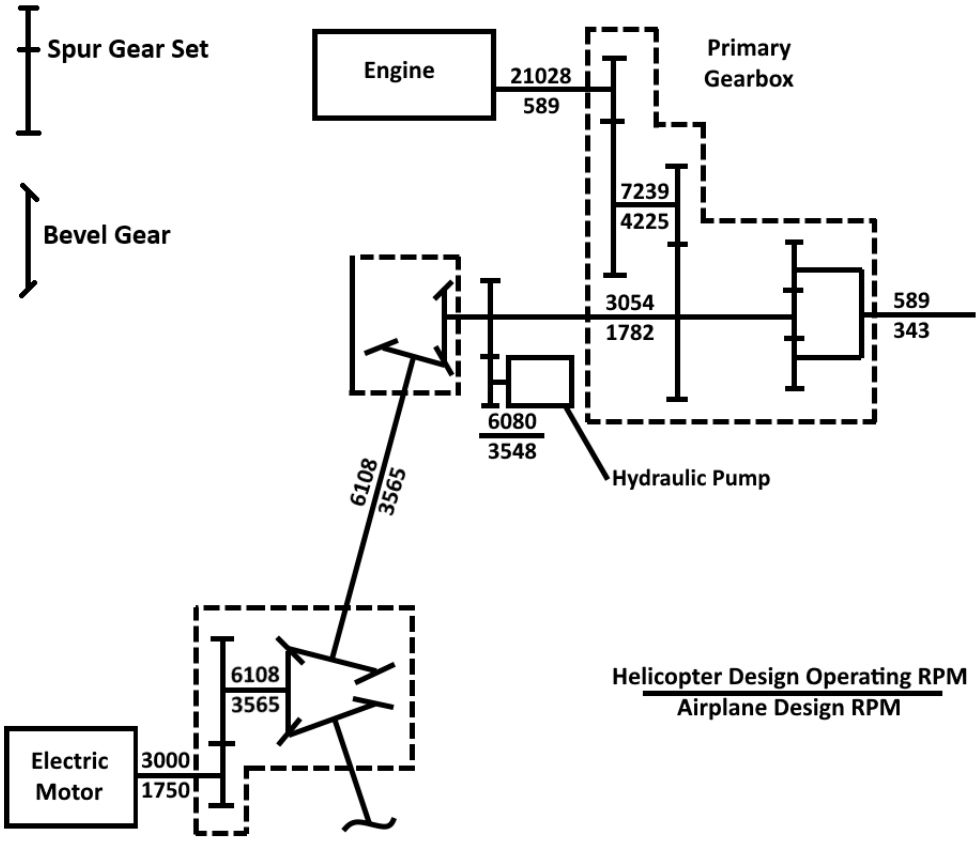


Figure 4.3: *Hermes*' drive system architecture.

Table 4.1: *Hermes* transmission, stage gear ratios

Gearbox		Teeth	Gear Module	Ratio	Efficiency
1st stage - Spur	Input	21	6	2.905	97%
	Output	61			
2nd stage - Spur	Input	27	7	2.370	97%
	Output	64			
3rd stage - Planetary	Sun - Input	27	7	5.185	98%
	Planet - Output	43			
	Ring - Fixed	113			
Bevel Transition	Connected to Rotor Shaft	27	7	5.185	98%
	Connected To Cross-Shaft	43			

taining acceptable gear dimensions and minimizing weight. *Hermes* also has the task of providing power from its 3000 RPM electric motor to the rotor. The ratio between the motor and rotor is therefore 5.1:1. The difference between these ratios required the electric motor to be placed after a substantial reduction stage following the engine to reduce any additional efficiency losses.

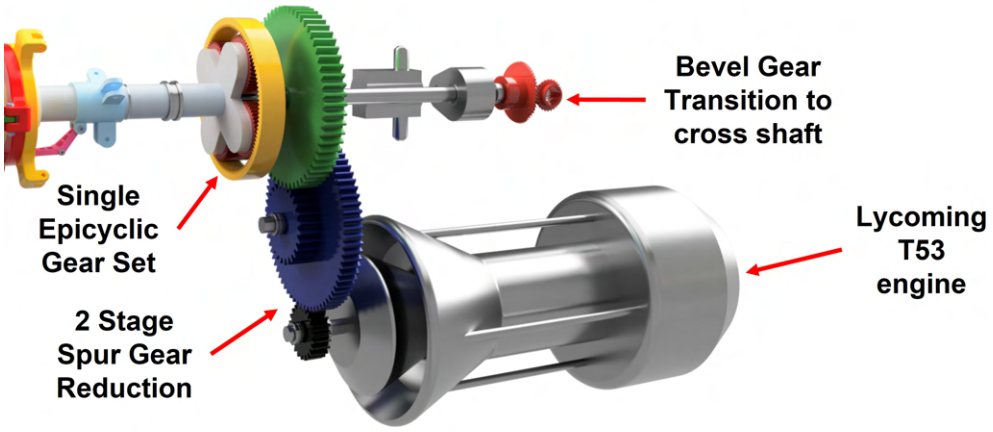


Figure 4.4: *Hermes* gearbox inside nacelle with gears highlighted.

Gear sizing was performed using a combination of Hertzian contact stress analysis and Lewis tooth-root bending stress calculations. These methods were used to establish the minimum module required to ensure that both surface fatigue and bending failure criteria were satisfied under the maximum expected operating loads. By optimizing the gear modules in each stage, *Hermes*' transmission system achieves the necessary speed reduction with substantial strength and durability safety margins while minimizing the overall gearbox mass. This weight reduction is particularly important for offsetting the additional mass associated with the hybrid-electric propulsion architecture without compromising drivetrain reliability or performance.

4.4 Supercritical Cross-Shaft

The XV-15 baseline cross-shaft is 60 mm (2.36 in) in diameter and 9 m (30 ft) long, divided into 8 sections, and operates at 6392 RPM (hover) and 5183 RPM (cruise). The shaft is supported by 10 hangar bearings and multiple dampers. A cross-shaft operating at supercritical speeds is an attractive alternative because it can lead to a lighter design. *Hermes* replaces the baseline cross-shaft with a supercritical design, which operates above its fundamental bending frequency so that unbalanced forces become self-stabilizing. This enables a significantly lighter shaft while still reliably transferring power between the two rotors. For *Hermes*, the cross-shaft is designed to rotate at 6108 RPM in hover and 3565 RPM in cruise.

The design is governed by shaft geometry (length, diameter, wall thickness) and support conditions, which together set the natural frequencies. An iterative process fixes the operating speed (3565-6108 RPM) in the bandwidth between the first and second natural frequencies, then checks fatigue strength and repeats until all constraints are satisfied. The resulting cross-section is 60 mm (2.36 in) radius with a 3 mm (0.1 inches) wall thickness and manufactured from aluminum alloy 7075, selected for its superior strength-to-weight ratio and fatigue tolerance. Each wing section is 2.13 m (7 ft) long, splitting the shaft into two sections per wing and placing the operating frequency safely between the first two natural frequencies. An additional $+10\%/-20\%$ RPM band plus a 15% margin accommodates rotor speed transients like overspeeds. Figure 4.5 shows the frequency band for the supercritical cross-shaft. The normal operating range (3565-6108 RPM) is highlighted in green. Additionally, overspeed is represented in yellow, and the extra margin is in red.

The weight benefit is twofold: a thinner wall reduces shaft mass, and the self-stabilizing behavior reduces the required supports to two mid-span bearing–flex-coupling pairs per wing. The design and placement of supports for one shaft element is shown in Fig. 4.6. Figure 4.7 shows the assembled shaft in *Hermes*.

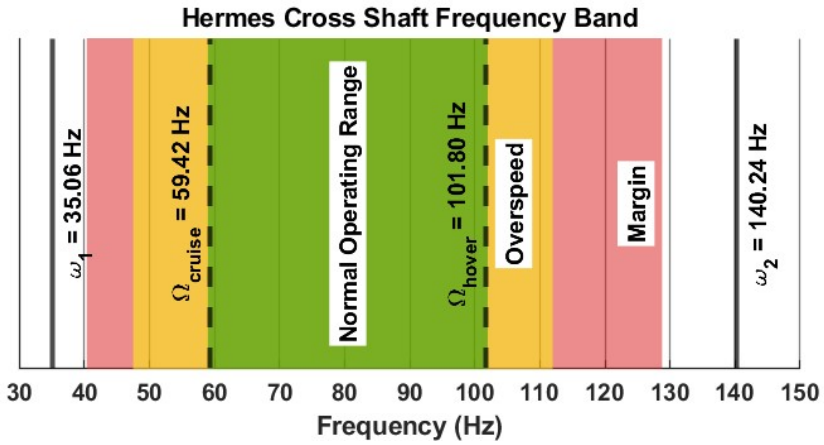


Figure 4.5: *Hermes* cross-shaft first and second natural frequencies with operating RPM band.

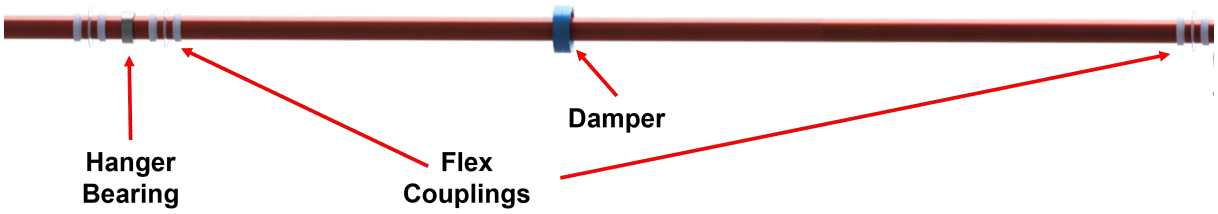


Figure 4.6: Cross-shaft with supporting components.

Together, these yield a ∼50% weight reduction over the XV-15 shaft, about 21 kg (45 lb). Transient crossing of the fundamental frequency is managed with shaft dampers.

4.5 Center Gearbox

In addition to the two turboshaft engines, the hybrid electric system of *Hermes* adds an electric motor, battery, and battery management system. The nacelles do not have room to accommodate these components, therefore they are integrated in the area around the interconnecting shaft gearbox. To support the hybrid electric addition, the central interconnecting shaft gearbox was redesigned to accept an additional power input while maintaining the original orientation. Placing the motor output between a pair of central bevel gears allowed the design to remain simplistic while reducing additional components.

Hermes has the same forward-swept, dihedral wings as the XV-15; therefore, the gears' spatial arrangement are the same as in the XV-15 center gearbox (6.5° forward, for the wing sweep, and 3.5° up). Mechanical power is transferred to and from the electric motor into the cross-shaft rotating at 6108 RPM, first through a set of lightweight planetary gears integrated into the electric motor output lowering the RPM to 3000. The power is then sent through a 1:2 bevel assembly to the cross-shafts, shown in Fig. 4.8. In order to maintain the correct direction of rotation for both sides of the cross-shaft, an idler gear is placed additionally in the left nacelle.

The compact central gearbox is mounted in *Hermes* using a single A-Frame. The gears in the system were designed using AGMA design methodology for the worst-case scenario of a single engine failure. This results in a substantial margin of safety when *Hermes* is operating under normal conditions.

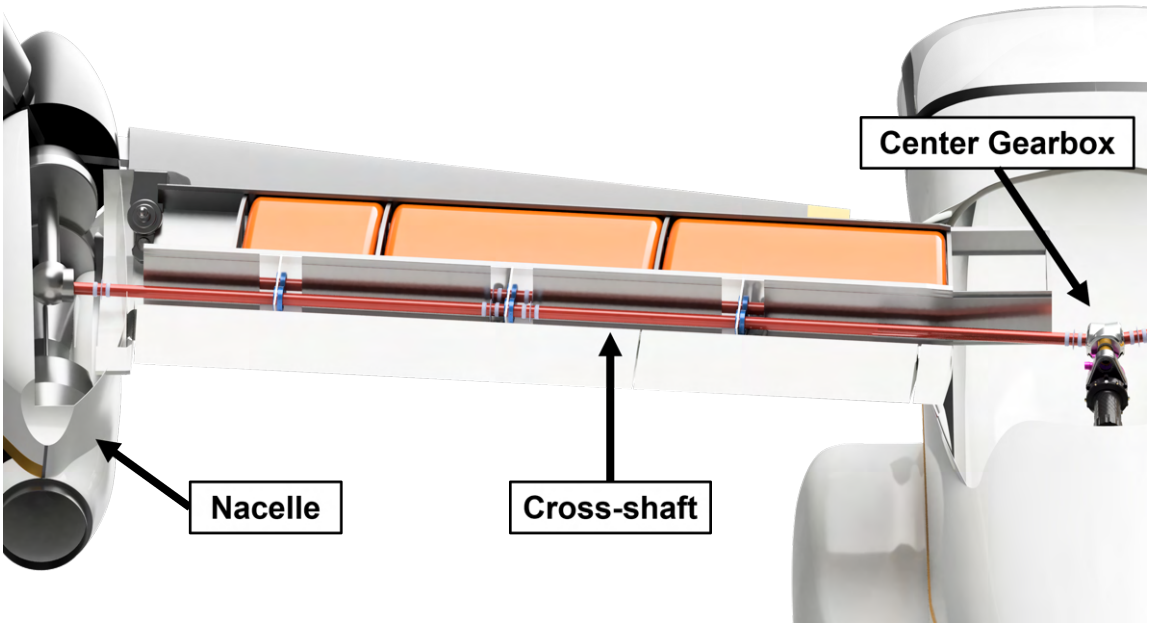


Figure 4.7: Half span of transmission between central gearbox and nacelle.

4.6 Material Properties

Issues around the reliability of the gearboxes in the V22 Osprey have led to a total overhaul of the entire fleet currently active in the military [ref [19]]. It was ruled that the input quill, the part that links the engine to the rest of the gearbox, needed to be replaced. This was done by swapping the gears originally made using PYROWEAR® 53 with an alloy of steel that has undergone a triple-melt process, referred to as VIM-ESR-VAR. PYROWEAR® 53 is an alloy that only undergoes VIM-VAR-VAR.

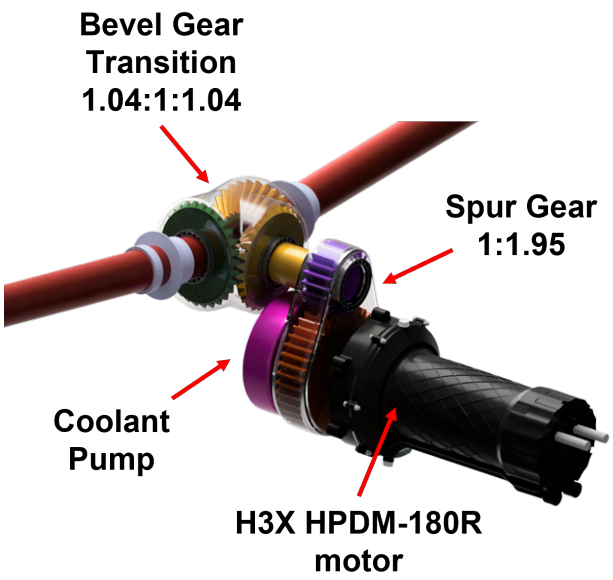


Figure 4.8: *Hermes* central gearbox.

In the first step, vacuum induction melting, the raw materials are melted and alloyed under vacuum, which also removes any dissolved gases that would make tiny pockets in the solidified material. Second, electro-slag removal melts the metal a second time, lifting oxides and other physical impurities out through a chemical filter. Finally, vacuum arc remelting, the alloy is remelted again, drop by drop, into a chilled crucible to reduce chemical separation.

Metals made using the triple-melt process have a uniform crystalline structure, which substantially increases toughness. One such metal, AerMet® 310, is an alloy of iron, cobalt, and nickel with an ultimate stress of 2100 MPa (310 kpsi) [20]. A 75% increase from the original 1200 MPa (175 kpsi) ultimate stress of PYROWEAR® 53 [21]. For the gears in both the nacelle and central gearbox, AerMet® 310 was selected for its excellent strength and durability.

4.7 Auxiliary Components

Several auxiliary components are retained from the baseline design. A sprag (freewheeling) clutch follows each engine output, disconnecting the engine from the drive train in the event of an engine failure. A flywheel on the output side of the clutch stores rotational kinetic energy, smoothing transient RPM drops during engine failure or deceleration.

Each nacelle houses a dedicated oil pump to continuously circulate transmission fluid, ensuring lubrication and thermal management of all gear meshes and bearings. A hydraulic pump is also located in each nacelle to maintain system pressure for the tiltrotor actuators and flight control surfaces.

Downstream of the oil pump, a series of filters and screens remove particulate contamination, both ingested foreign objects and metallic wear debris, before the fluid returns to the sump. A magnetic chip detector (MCD) is installed in the oil circuit to collect ferrous particles. When sufficient material bridges the detector contacts, a cockpit warning is triggered. Some MCDs incorporate a burn-off circuit to clear fine particles; however, a persistent MCD warning indicates significant mechanical damage and requires immediate landing.

5 Hermes Engine Controls

Hermes retains the XV-15's proven mechanical flight control and hydraulic systems without modification. The mechanical control mixing linkages, swashplate actuators, and conversion hardware are unchanged, with nacelle-mounted hydraulic pumps continuing to power the swashplate, conversion actuators, and control surface actuators as in the baseline. To enable the hybrid propulsion architecture, two systems are added: a Full Authority Digital Engine Controller (FADEC) on each turboshaft, and a central Hybrid Management Computer (HMC) that coordinates power delivery across the turboshafts, electric motor, and battery pack.

5.1 Cockpit Controls

The cockpit retains the XV-15 lateral and longitudinal stick, yaw pedals, throttle, and nacelle tilt switch. A single hybrid enable switch on the center console allows the pilot to engage or disengage the automatic hybrid strategy. Beyond this, all power splitting, engine governing, and battery management is handled automatically by the FADEC and HMC without additional pilot input.

5.2 Full Authority Digital Engine Controllers

Each turboshaft is governed by a dedicated dual-channel FADEC, replacing the XV-15's original hydromechanical fuel control units. Digital engine control is required to coordinate turboshaft output with the electric motor and battery in real time, a function not possible with the original mechanical fuel control. The FADEC maintains closed-loop control of fuel flow, turbine inlet temperature (TIT), and turbine shaft speed, and communicates continuously with the HMC to execute the hybrid power strategy.

5.2.1 Rotor Speed Governing Through Conversion

Once three actions are performed: the nacelles fully tilt forward to 0°, the aircraft accelerates past a scheduled airspeed threshold, and the pilot initiates cruise mode, the FADEC reduces rotor RPM from 589 RPM to 343 RPM. When the pilot commands hover mode, the FADEC increases rotor speed back to 589 RPM as airspeed decreases below the velocity threshold, prior to nacelle tilting.

5.3 Hybrid Management Computer

The HMC receives real-time data from several sources: battery state-of-charge, terminal voltage, current, and cell temperatures from the BMS; turboshaft torque and turbine inlet temperature from each FADEC; rotor shaft speed; and DC bus voltage and motor winding temperature from the power electronics. Using these inputs, the HMC issues a torque command to the motor inverter and a power trim request to each FADEC. While the FADECs retain full authority over their respective engines, the HMC operates as a supervisory controller that adjusts the requested engine operating point rather than commanding fuel flow directly. The DC/DC converter on the battery discharge path is also regulated by the HMC to maintain constant bus voltage as cell voltage drops with battery state of charge.

6 Hermes Rotor Hub Design

The XV-15 utilizes a gimbaled rotor hub design with a universal joint that reorients the rotor speed normal to the tip-path plane. Because the input shaft rotates at a constant speed, this reorientation causes the rotor's angular velocity to fluctuate twice per rotor revolution, inducing a 2/rev pylon excitation. The XV-15 was unable to substantially lower its rotor speed in cruise due to this 2/rev pylon vibration.

Hermes replaces the universal joint with a three-bladed, gimbaled, stiff in-plane rotor hub based on the proven Bell Boeing V-22 hub design. Torque is transmitted through three elastomeric drive links arranged as a homokinetic constant-velocity joint, allowing the hub to gimbal freely while maintaining a uniform output speed. This modification directly resolves the 2/rev pylon excitation found in the XV-15 universal joint hub, enabling *Hermes* to reduce rotor RPM from 589 RPM in hover to 343 RPM in cruise and significantly improve cruise aerodynamic performance.

6.1 Hub Selection

Four commonly used hub configurations were evaluated before selecting the final design: articulated, bearingless, hingeless, and gimbaled. Articulated hubs were eliminated as they are the heaviest and would result in large flap deflections in propeller mode. Bearingless hubs were not selected as they cannot achieve the large collective range required between hover and cruise for efficient proprotor operation. Hingeless hubs are a viable, compact, and simple configuration. However, they experience high loads during transition that must be reacted through the hub and wing structure, increasing weight. The gimbaled hub was therefore selected, designed with elastomeric drive link elements to form a constant-velocity joint. With these elements, *Hermes* removes the 2/rev pylon vibration experienced by the XV-15 while retaining the gimbaled hub's ability to flap freely, lowering aerodynamic loads during conversion. The hub assembly in Fig. 6.1 consists of a constant-velocity joint, carbon fiber pitch cases, hub yoke, scissor arms, pitch links, swashplate, and rotor shaft.

6.2 Rotor Hub Assembly

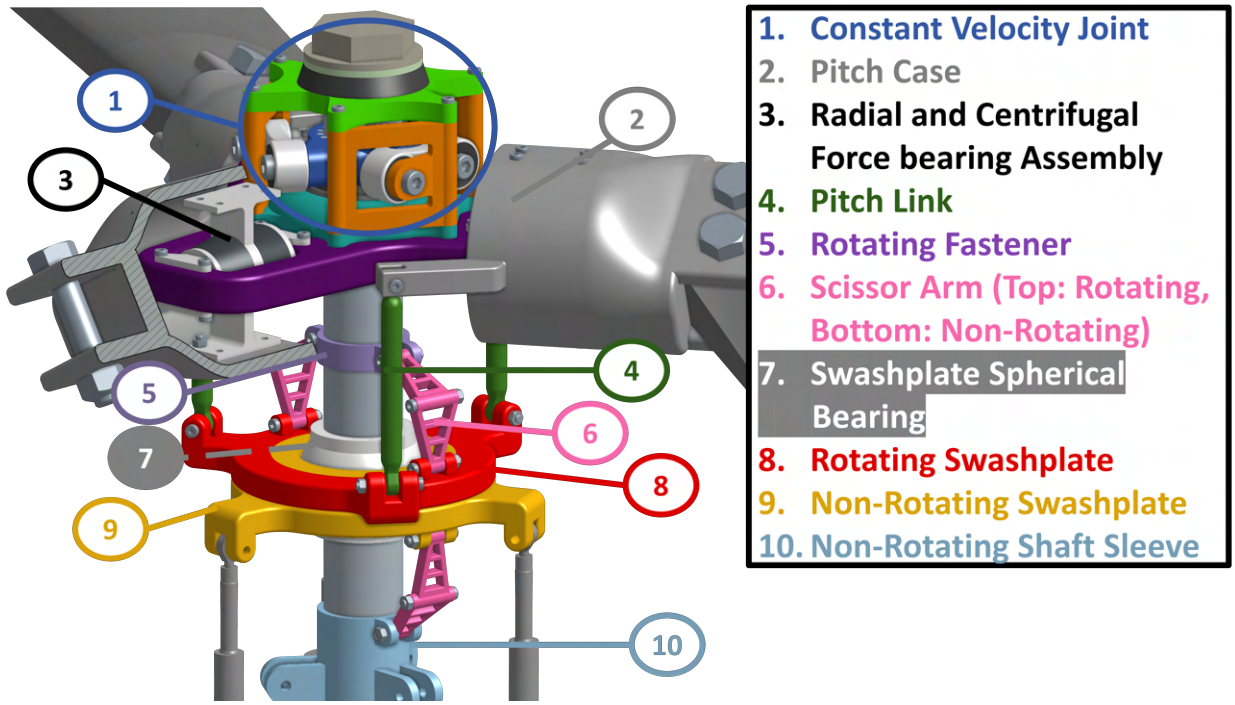


Figure 6.1: Gimbaled rotor hub assembly.

6.3 Constant-Velocity Joint

The constant-velocity joint allows for the transfer of torque from the rotor shaft to the yoke without inducing vibrations. The design of the constant-velocity joint is detailed in Fig. 6.2. The constant-velocity joint starts with the splined drive trunnion connected to the rotor shaft. The drive links are arranged as three sides of a hexagon with one end connected by the trunnion and the other end attached to a pillow block bolted to the yoke. Elastomeric bearings are installed into each end of the drive links. The three drive links transmit torque from the rotor shaft to the yoke and permit hub flapping up to a limit of $\pm 12°$. The elastomeric bearings ensure a nearly constant-velocity output from the joint by enabling oscillating rotational deflections about the axis of the links, allowing the gimbal motion and eliminating the 2/rev vibration. Finally, the spherical elastomeric upper and lower hub springs act as centering bearings and also react the rotor thrust. The hub springs are able to limit the angular misalignment between the yoke and the shaft by deforming in compression. Using proven technology from the V-22 [22], this rotor hub limits flap loads transferred to the hub while resolving the vibratory issue inherent in the XV-15 design.

The proprotor yoke is made of S-2 fiberglass molded to its finished shape in a die. A finishing process is performed on the yoke to bore the attachment holes and central clearance for the shaft, apply anti-fretting coating, and install bushings. The fiberglass yoke is lighter compared to the steel yoke of the XV-15 and transfers force without vibrating due to low mechanical impedance. The yoke is stiff in-plane and each of the three arms house the bearing assemblies with the constant-velocity joint mounted at the center.

The carbon fiber/epoxy pitch case, which attaches the blade to the yoke and pitch links, is manufactured using filament winding of nine tubular layers with the insertion of precut plies and preformed filament wound belts. This allows the pitch case to carry high shear loads from the short spacing between the blade attachment and pitch bearings, as well as the blade root bending loads. The main attachment bolts transmit blade chordwise bending into the pitch case, where they are reacted into radial pitch bearings.

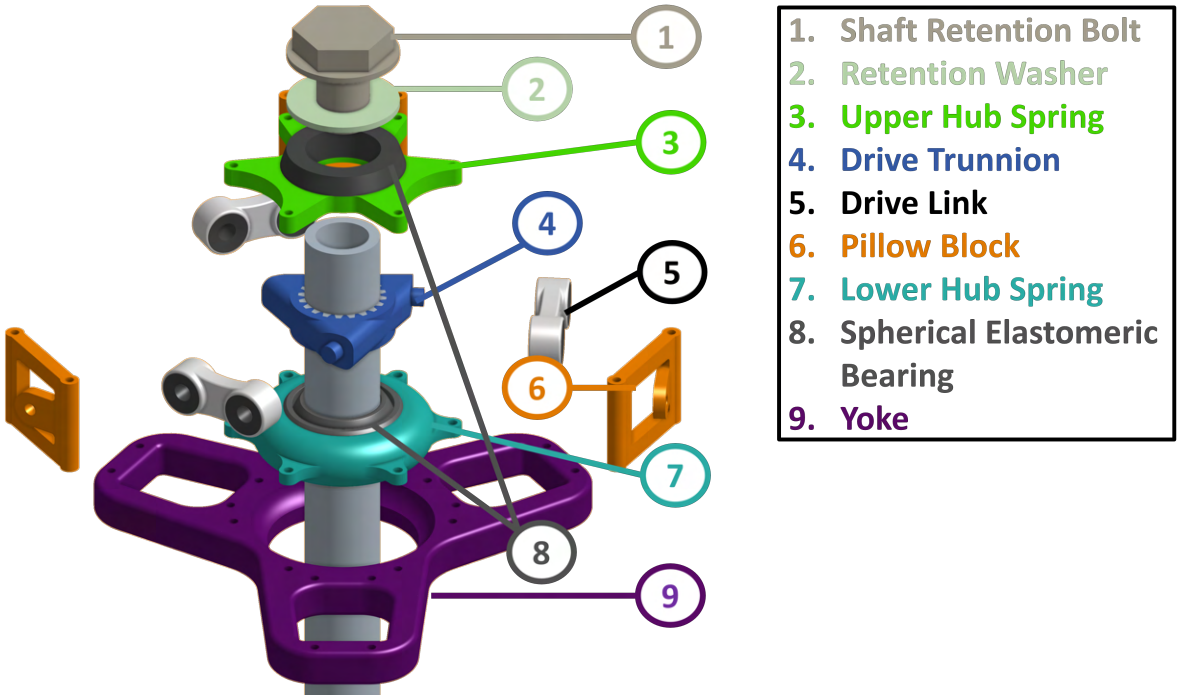


Figure 6.2: Constant-velocity joint exploded view.

6.4 Pitch Link and Pitch Horn

The pitch horn is fixed inboard on the pitch case and houses an integrated ball joint that attaches to the upper pitch link rod end, converting axial swashplate motion into rotational pitch case motion. It is machined from stainless-steel, selected for its high specific strength under the combined cyclic bending and axial loads encountered in both helicopter and airplane operating modes. Aerodynamic pitching moments acting on the blade are reacted as bending stresses across the horn arm and transmitted as axial loads through the pitch link to the swashplate.

The elastomeric pitch bearings, attached to the yoke and pitch cases, are designed to handle blade pitch angle changes, blade bending, and centrifugal forces. The bearing assembly provides a 60° range of pitch articulation. Within this assembly, the outboard conical elastomeric bearing is loaded in compression and resists the substantial centrifugal and flap and lag shear loads from the blade, while the inboard radial elastomeric bearing transfers torsional loads to the yoke. A negative pitch-flap coupling angle, $\delta_3 = -15°$, provides passive stabilization in cruise from high axial inflow. The δ_3 geometry is physically implemented by offsetting the pitch horn ball joint aft of the feathering axis at a set chord-wise distance.

The pitch horn is located at 3.5% of rotor radius, placing it inboard far enough to clear the rotating swashplate scissors for the full hub gimbal travel of ±12° while minimizing the lever arm that transfers blade root bending loads into the pitch case. At this geometry, an axial swashplate translation of 1.5 mm produces 1° of blade pitch change. The 60° pitch articulation range provided by the elastomeric pitch change bearing assembly fully encompasses the operational collective range, with swashplate actuator stroke defining the flight-envelope limits.

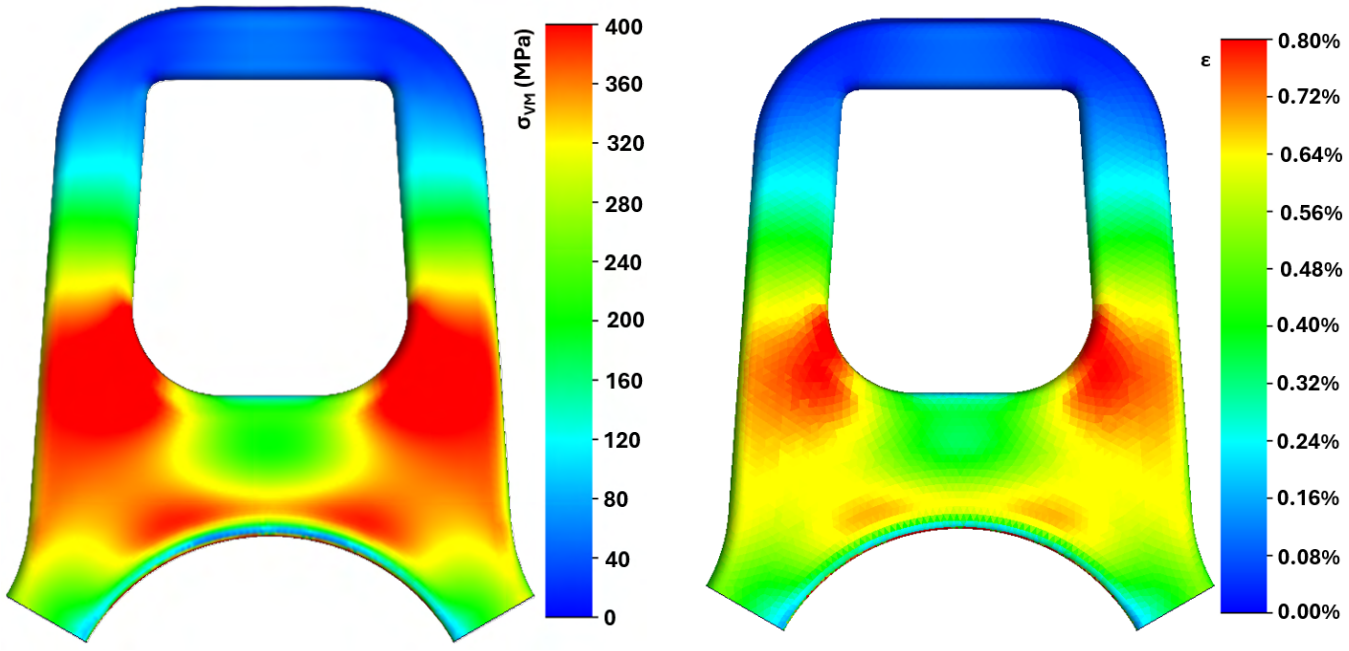
6.5 Swashplate Design

The XV-15 utilizes a set of two pitch links to actuate the blade pitch where above the rotor blade, a lever assembly attaches a short pitch link to the pitch cases and a longer pitch link extends through the rotor

plane to the swashplate. This assembly pitches the blades up when the swashplate translates up the rotor shaft. *Hermes* eliminates the XV-15 hub spider entirely, instead directly connecting the swashplate to the pitch cases with one pitch link. This redesign alters the kinematic gain structure of the rotor control system relative to the XV-15 arrangement and requires re-tuning of control law gains. Particularly, a swashplate translation downward increases the blade pitch on *Hermes*. Three hydraulic actuators provide control to the non-rotating swashplate which is held in place by scissors attached to a non-rotating shaft sleeve. The non-rotating swashplate is attached to a spherical bearing and houses a tapered roller bearing. The rotating swashplate is secured to the tapered roller bearing. Rotating scissors connected to the rotating swashplate and fastener alleviate bending and shear loads on the pitch links.

6.6 Finite Element Analysis

The yoke is the primary structural member carrying load from the rotor into the hub. As a result, special attention was given to predict stresses in the yoke. A finite element analysis (FEA) was conducted on the yoke to ensure a large safety factor when withstanding the loads from the XV-15 blades featured on *Hermes*. FEA was performed using SolidWorks Simulation with unstructured tetrahedral elements. A curvature-based mesh was used, with the characteristic length set at 3.18 mm (0.125 in) to adequately capture stresses carried through fillets. This resulted in a high-quality mesh with the aspect ratio of all elements below three. These mesh settings yielded approximately six-hundred-thousand elements for the full-body model. Courser meshes were also run to identify any singularities present in the stress distributions.



(a) Stress distribution.

(b) Strain distribution

Figure 6.3: Yoke FEA at 2g hover loading condition.

The shaft connection was represented by a fixed boundary condition applied to the interior face of the central cut with 76.2 mm (3 in) radius. A cyclic symmetry boundary condition was applied every 120° of the yoke to significantly reduce computational expense. The faces on the front and back of the yoke had a force of 57.8 kN (13,000 lb) evenly distributed in the direction of the shaft, as well as three 41 kN-m (30,240 lb-ft) torque loads applied along the flapping axis for the respective blade. A 589 RPM-based centrifugal load was also applied. This loading case is representative of a 2g loading during hover, where

the vertical force and torque applied represents the total lift and root bending moment produced by each blade in this condition.

7 Hermes Vehicle Performance

This section details the overall improved performance of *Hermes* over the XV-15.

7.1 Hover Performance

Hermes spends the majority of its mission in airplane mode. However, *Hermes* was designed to hover out of ground effect (HOGE) at 1,219 m / 35°C (4,000 ft / 95°F), and as such, exceeds the hover capability of the XV-15. With no changes made to the vehicle gross weight, T53 engines, airframe design, and blade design, the hover capability of *Hermes* at both ISA and ISA +20°C atmospheric conditions mirrors that of the XV-15. The XV-15 cannot hover out of ground effect under 4K/95 atmospheric conditions even with both T53 engines operating at maximum rated power (MRP). The inclusion of a 180 kW (241 HP) battery and electric motor in the hybrid design considerably increases the power available as shown in Fig. 7.1.

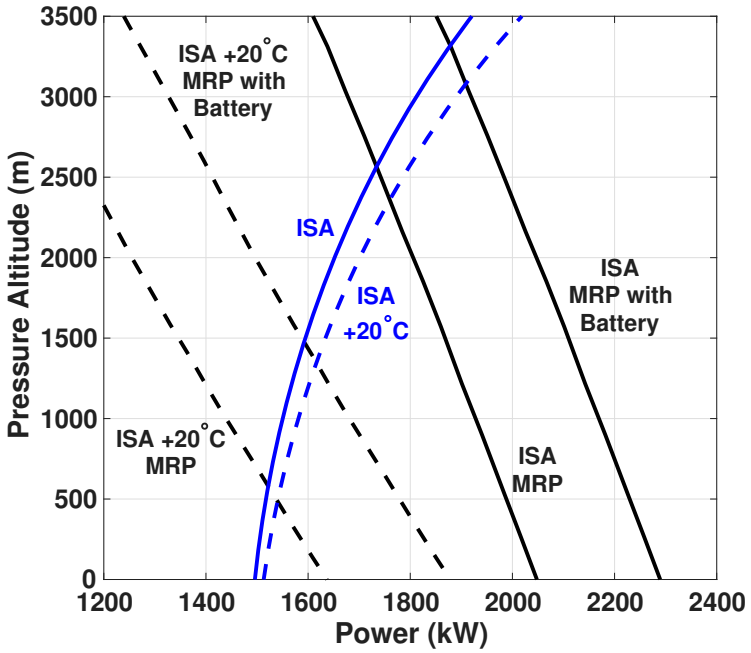


Figure 7.1: *Hermes* hover power required and total maximum rated power (MRP) and battery power available under ISA and ISA +20°C conditions at various pressure altitudes.

The power output of a battery, unlike combustion engines, remains constant with altitude. For the short 5-minute HOGE under 4K/95 conditions, *Hermes* operates the engines at MRP and discharges the battery at 180 kW (245 HP), the maximum output from the electric motor. *Hermes* cannot hover any higher under ISA +20°C conditions. In standard atmospheric (ISA) conditions, *Hermes* has a hover ceiling of 2,560 m (8,400 ft) without battery usage and 3,320 m (10,892 ft) with hybrid utilization.

7.2 Cruise Performance

As tiltrotor aircraft, *Hermes* and the XV-15 both operate across multiple flight regimes, ranging from helicopter mode through the conversion corridor to airplane mode, with various nacelle tilt and wing

flap angles. To model these configurations, aerodynamic lookup tables for lift, drag, and pitching moment coefficients (c_l, c_d, c_m) were generated using CFD for the multi-element wing airfoil section (NACA 64A223) used in the XV-15 and *Hermes* wing at different flap deflections. These tables were incorporated into a BEMT-based trim-solver to account for the wing aerodynamic contribution at each flight condition.

The power required for different nacelle and flap angles is shown for both vehicles in Fig. 7.2. XV-15 flight test data is compared to validate the trim solutions. The solver accurately predicts power required across the full speed range for all flight configurations tested of the XV-15, demonstrating close agreement with flight test data in helicopter, conversion, and airplane mode flight conditions.

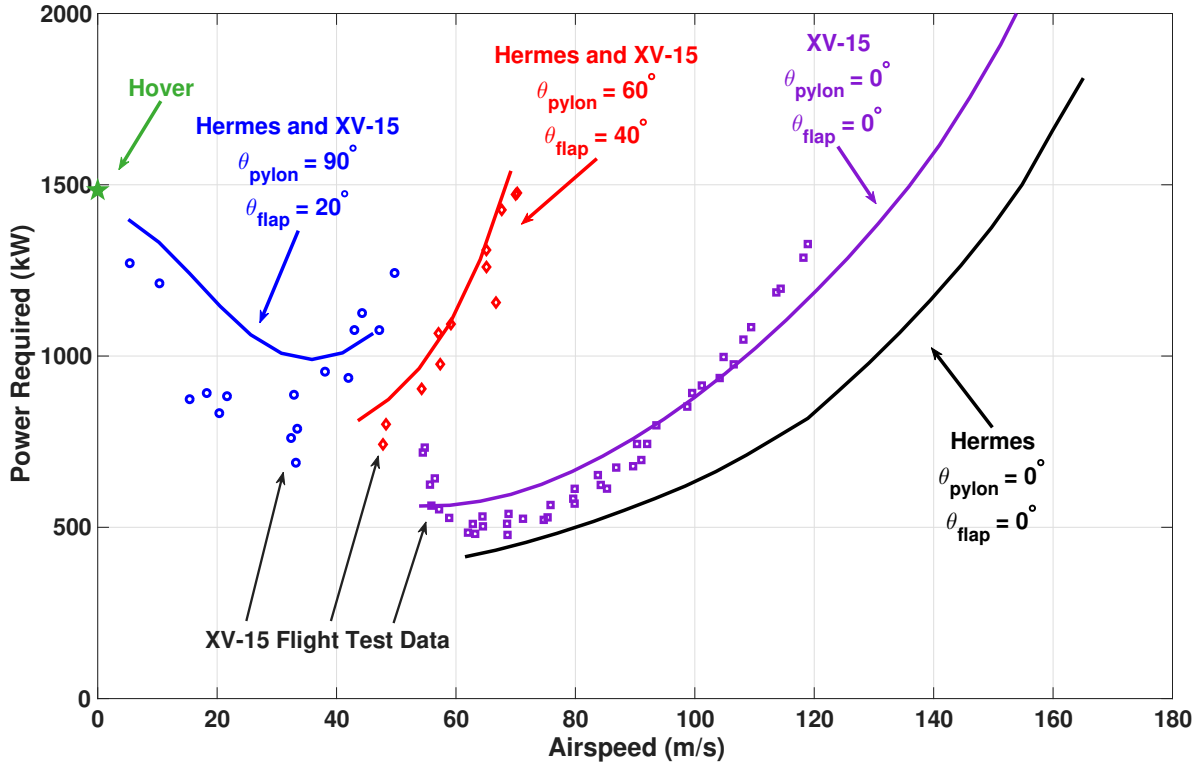


Figure 7.2: Power required in flight of the XV-15 and *Hermes* in helicopter, conversion, and airplane modes. Symbols: XV-15 flight test data, lines: predictions.

The power for *Hermes* is the same as the XV-15 during helicopter and conversion mode when the rotor speed is 589 RPM because the gross weight, rotor aerodynamics, and airframe remain the same. However, due to a reduction in cruising rotor RPM from 517 RPM on the XV-15 to 343 RPM on *Hermes*, the power during airplane mode is reduced for *Hermes*. This rotor RPM reduction primarily decreases rotor profile power. *Hermes* is additionally capable of operating at higher speeds due to this lower cruise power and the supplemental power from the electric motor and battery.

The L/D of the XV-15 and *Hermes* is shown in Fig. 7.3. The reduced power required in airplane mode increases the L/D in airplane mode of *Hermes* compared to the XV-15. *Hermes* has a maximum L/D of 9.3 at an airspeed of 89 m/s (173 kt). The XV-15 has a predicted L/D of 7 at 85 m/s (165 kt), although the flight test data indicates a maximum L/D of 8.3 around 75 m/s (146 kt). Regardless, *Hermes* outperforms the XV-15.

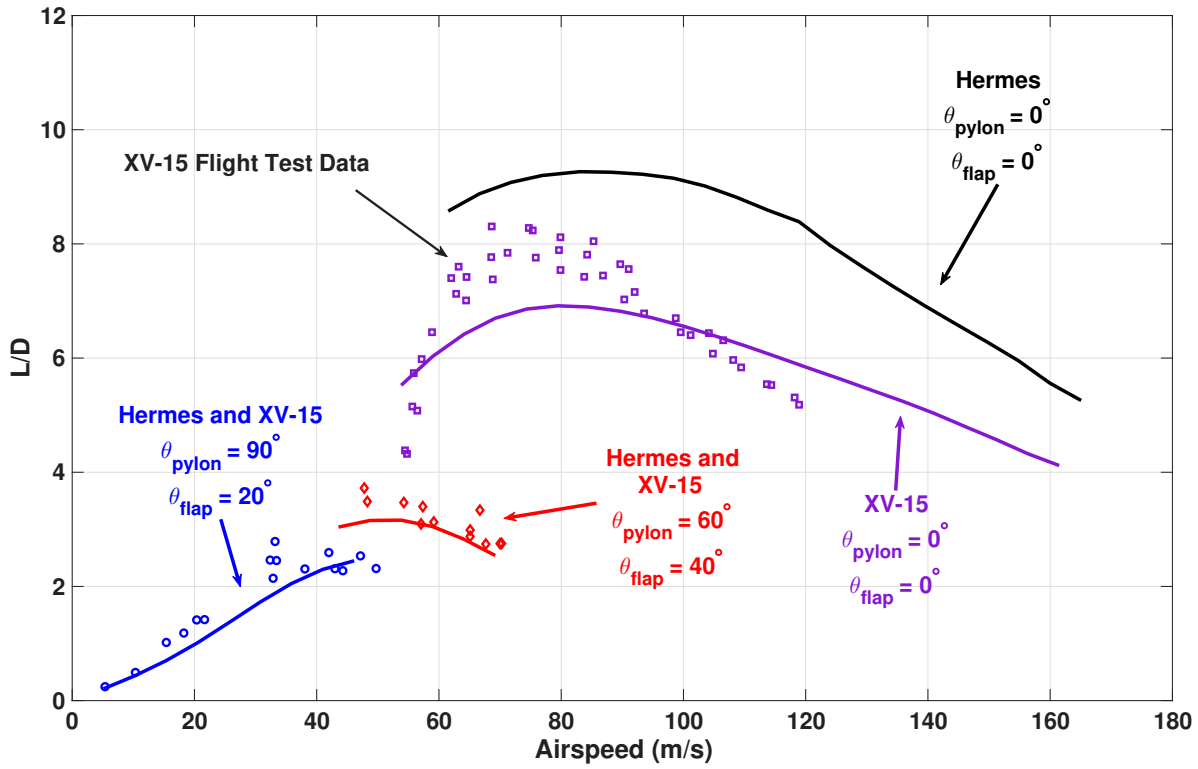


Figure 7.3: L/D of the XV-15 and *Hermes* in helicopter, conversion, and airplane modes. Symbols: XV-15 flight test data, lines: predictions.

The velocities for best range and best endurance are shown in Fig. 7.4 for the XV-15 and *Hermes*. The velocities for both aircraft are comparable, but as before, the power required is lower for *Hermes*.

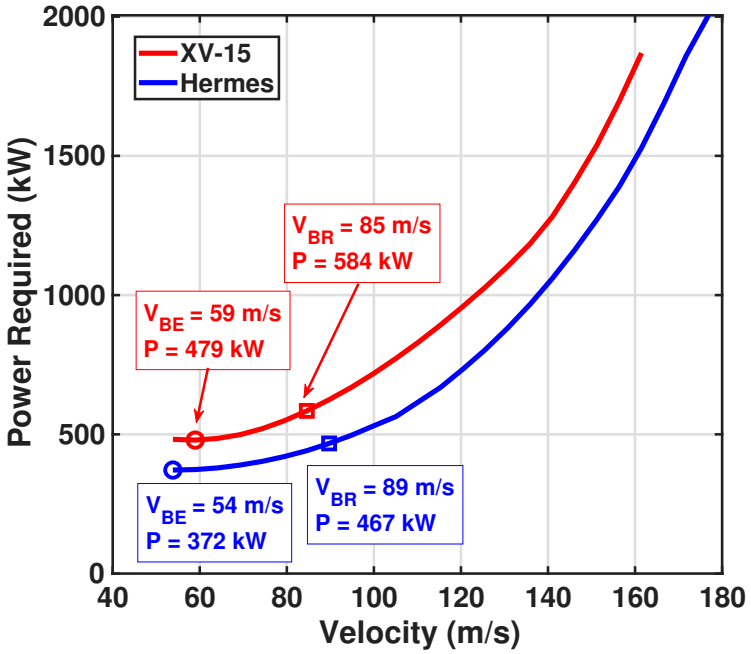
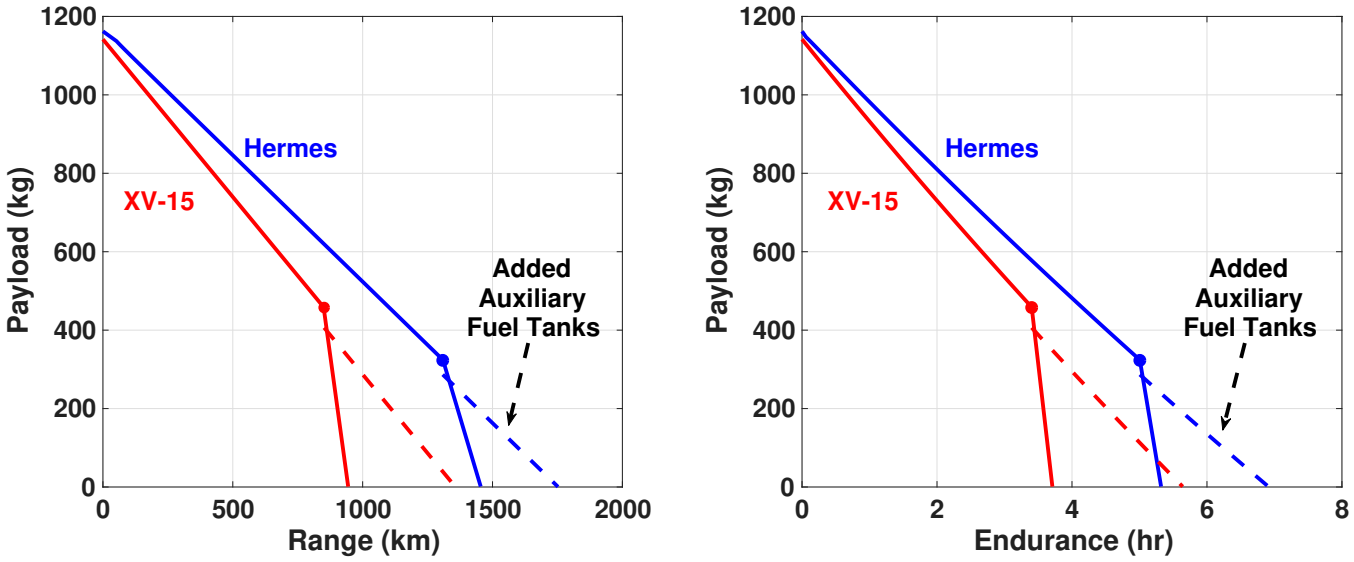


Figure 7.4: Velocities for best endurance and range for the XV-15 and *Hermes*.

The ranges of the XV-15 and *Hermes* are shown in Fig. 7.5(a). Both aircraft operate with two pilots weighing a total of 181 kg (400 lb), not included in the payload weight. *Hermes* outperforms the XV-15

due to operating at a reduced power and slightly higher speed. The larger onboard fuel tank and addition of a battery enable a maximum range of 1,308 km (706 nm) with 328 kg (723 lb) of payload compared to a range of 852 km (460 nm) with 458 kg (1,009 lb) of payload for the XV-15. Maximizing the onboard fuel and reducing the payload to zero adds a small range increase to both aircraft. Supplying auxiliary fuel tanks to maximize fuel weight, thereby also reducing payload weight to zero, improves the range to 1,357 km (733 nm) for the XV-15 and 1,752 km (946 nm) for *Hermes*.



(a) Range (b) Endurance

Figure 7.5: Range and endurance of XV-15 and *Hermes* with two pilots.

The endurance of the XV-15 and *Hermes* are shown in Fig. 7.5(b). Similarly, the endurance of *Hermes* exceeds that of the XV-15. The maximum endurance of *Hermes* with only the onboard fuel tanks is 5.0 hours whereas the XV-15 can only operate for 3.4 hours. Carrying zero payload extends the endurance by 0.3 hours for both aircraft. Supplying auxiliary fuel tanks at the cost of payload capacity expands the endurance to a maximum of 6.9 hours and 5.9 hours for *Hermes* and the XV-15 respectively.

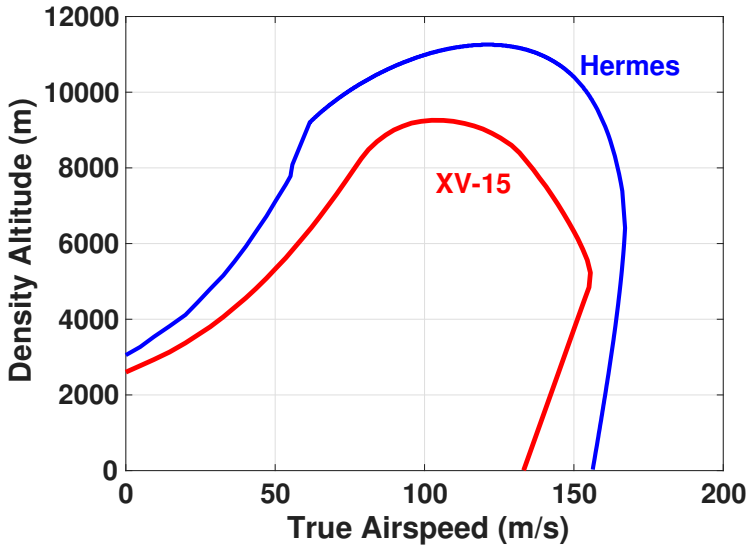
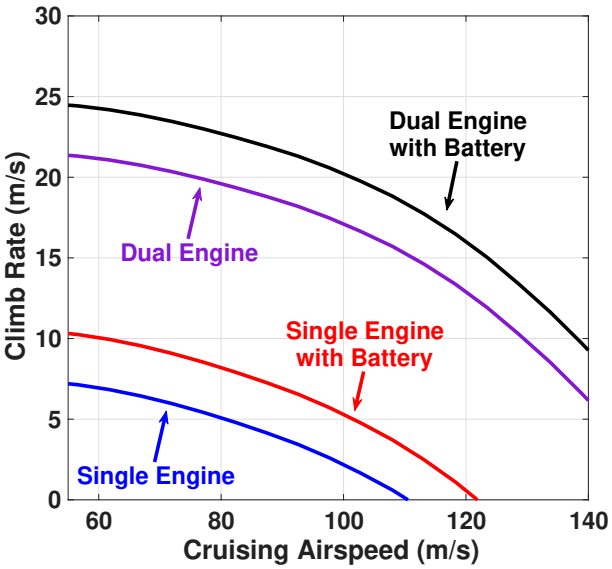


Figure 7.6: Height-velocity envelope for XV-15 and *Hermes*.

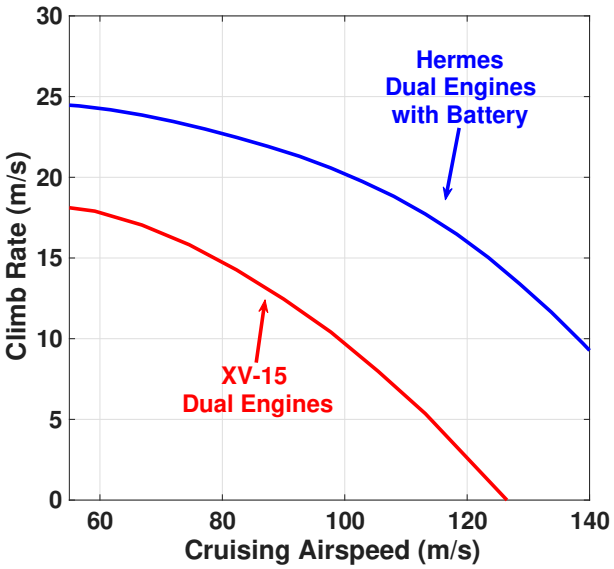
The height-velocity envelope for XV-15 and *Hermes* is shown in Fig. 7.6. The reduction in power required to cruise due to reducing the rotor RPM and the inclusion of a battery to provide additional power raises the height envelope of *Hermes* over the XV-15. The XV-15 is also torque limited by the drivetrain, preventing speeds greater than 156 m/s (303 kt). At an altitude of 3,048 m (10,000 ft), the required altitude for the cruise segment in the RFP mission, the XV-15 cannot exceed 147 m/s (286 kt).

7.3 Climb Performance

The rate of climb for *Hermes* in airplane mode is shown in Fig. 7.7(a). Single engine operation is an option to minimize power and fuel consumption at the cost of reduced cruising and climbing speed. Operating both engines at maximum continuous power (MCP) and discharging the battery enables exceptionally fast climb rates as high as 25 m/s (4,840 ft/min). With the hybrid architecture, the climb segment can be utilized to recharge the battery. Comparing with the XV-15 as shown in Fig. 7.7(b), *Hermes* can climb at substantially faster rates, and at very high speeds, past 127 m/s (246 kt). For the RFP mission, *Hermes* completes the climb segment in 10.6 minutes at a climb rate of 4.8 m/s (943 ft/min) and climb speed of 64 m/s (125 kt) to avoid wing stall. The battery is recharged during the climb segment and therefore does not assist the engines to climb.



(a) Climb rate of *Hermes* at sea level with various combinations of battery and engine usage.



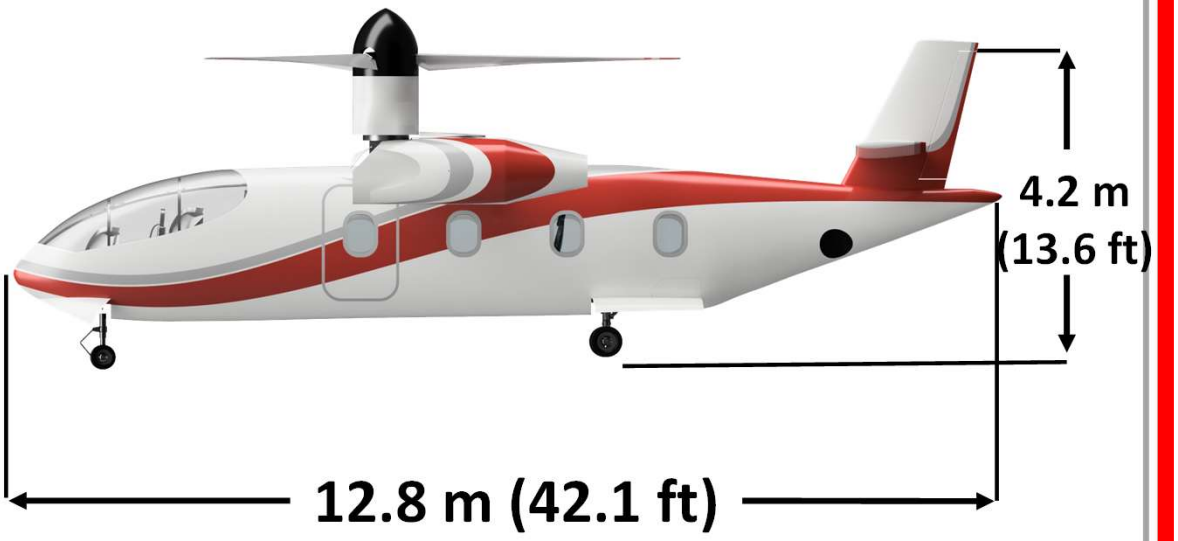
(b) Climb rate of *Hermes* and XV-15 at sea level at maximum continuous power (MRP).

Figure 7.7: Climb rate of XV-15 and *Hermes* with varying power usage.

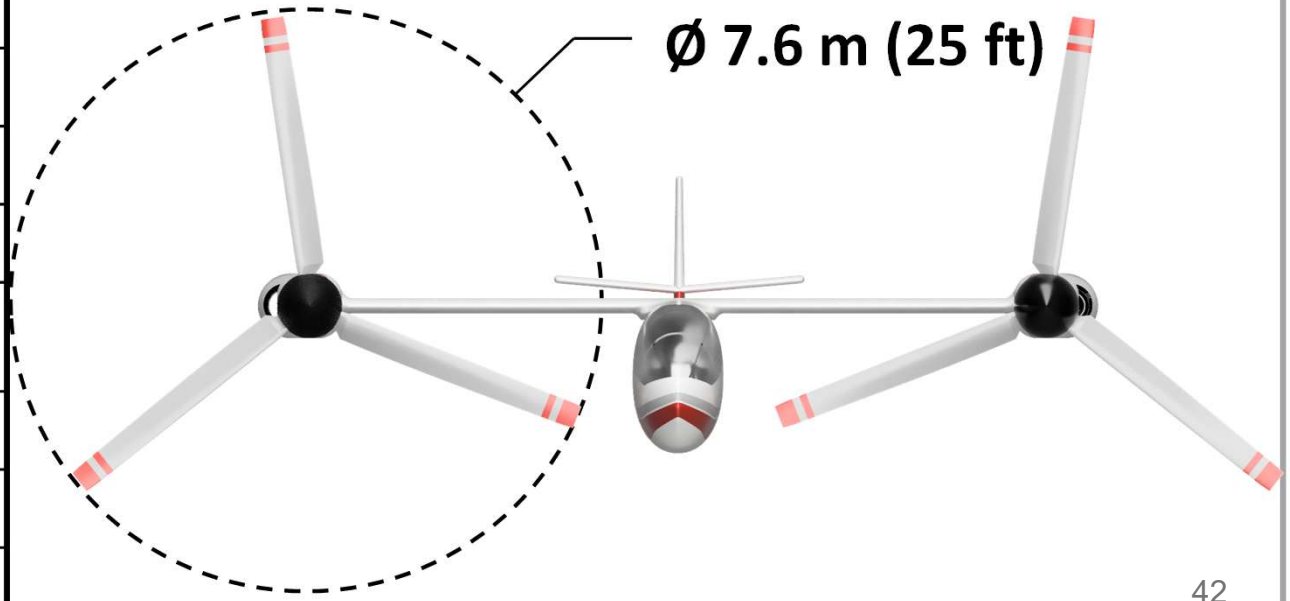
The phase 1 constrained hybridization of XV-15 into *Hermes* yields improvements to hover performance, cruise speed, range, and endurance with minor changes to empty weight.

Mercury Overview, Phase 2

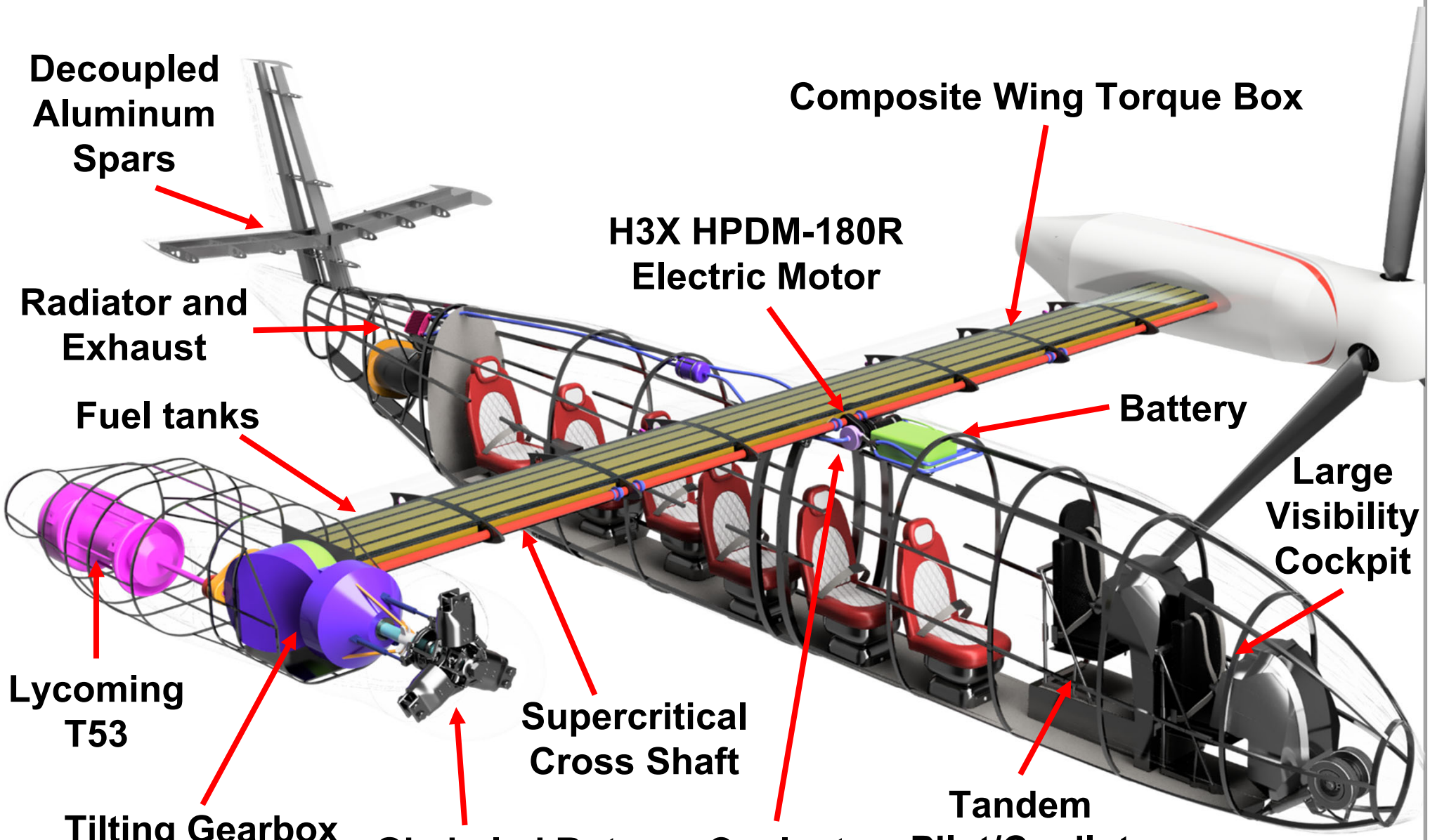




Characteristics	Value
GTOW	4939 kg (10891 lb)
Payload	726 kg (1600 lb)
Fuel Weight	3599 kg (1355 lb)
Turboshaft Power	1341 kW (1798 hp)
Electrical Power	180 kW (241 hp)
Range	1063 km (574 nm)
Max Speed	180 m/s (350 kts)



Detailed Internal Layout



8 Mercury Hybridization

The next portion of the report documents the phase 2 minimally constrained hybrid tiltrotor design, *Mercury*.

8.1 Hybrid Configuration Selection

The hybrid configuration selection procedure for *Mercury* followed the same process as *Hermes*. A parallel hybrid architecture utilizing a mechanically driven system is selected over an electrically driven system to maintain high operational reliability without adding considerable weight from electric components.

Mercury, through weight and aerodynamic improvements, requires substantially less power to fulfill the RFP mission. Four different configurations were considered for *Mercury*.

- One engine, one battery and motor (1E)
- Two engines, one battery and motor, engine cycling on and off during cruise (2E)
- Two engines, one battery and motor, engine throttling during cruise (2E-T)
- One T53 engine and one downscaled engine, one battery and motor, smaller engine turning on and off during cruise (2E-1B1S)

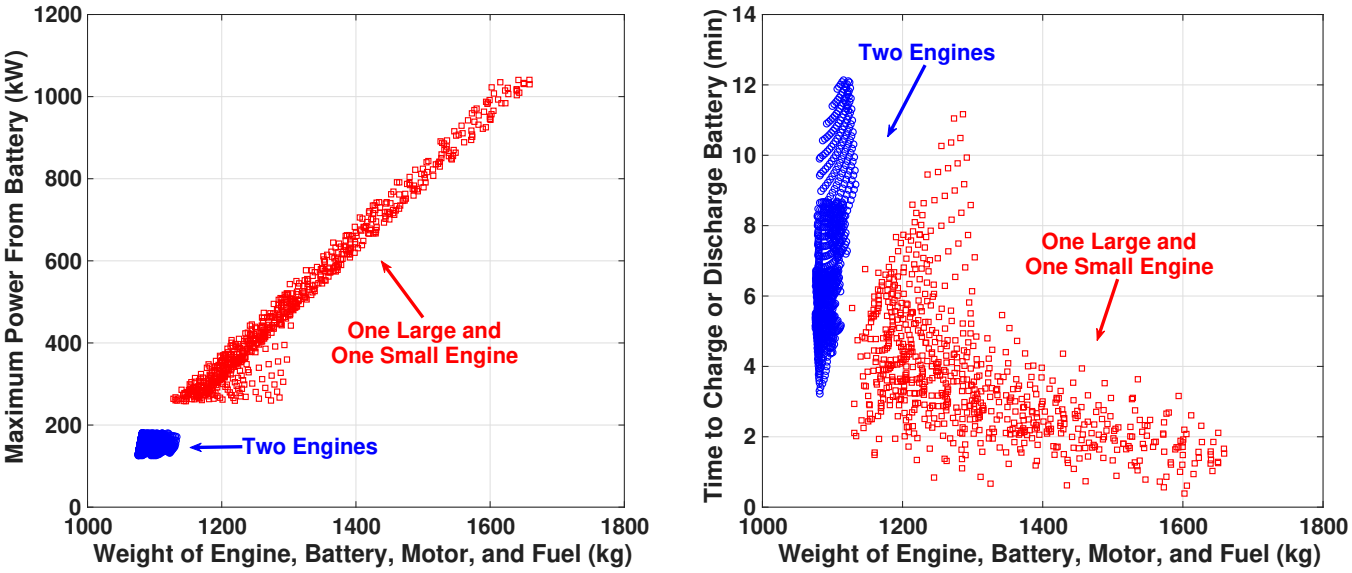
Despite the lower power requirements, a singular T53 engine, configuration 1E, remains insufficient in providing the necessary power to carry out the mission. Augmenting the engine with a large battery contributed a significant weight increase. Requiring 1160 kW (1555 HP) to hover out of ground effect (HOGE) at 1219 m / 35°C (4000 ft / 95°F) atmospheric conditions, the battery needs to provide a minimum of 460 kW (625 HP) of power resulting in a 184 kg (406 lb) battery. Additionally, *Mercury* needs 1047 kW (1404 HP) for one hour during the cruise segment, which requires a battery of at least 247 kWh of energy. This energy demand amplifies the battery weight to 988 kg (2200 lb). These combined battery and motor demands necessitate a two engine system.

Given the reduced power requirements compared to the XV-15, *Mercury* can afford to reduce the maximum power output from the engines. Configuration 2E attempts to downscale the two engines and cycle one on and off during cruise to charge and discharge the battery. Installing two T53 engines without downscaling is also an option if more charging power is desired. However, regardless of downscaling, this configuration necessitates a large battery power demand. If the available engine power is slightly higher than cruise power, turning off one engine demands a large battery discharge power. If the available engine power is substantially larger than cruise power, turning on one engine will charge the battery at a very high rate. This high battery power requirement significantly increases battery and electric motor weight, and therefore, will not minimize the vehicle gross weight.

The third configuration, 2E-T, equally downscales the two engines and equally throttles the engines to charge and discharge the battery during cruise. The fourth configuration, 2E-1B1S, uses one downscaled engine and one T53 engine. The smaller engine is turned on and off during cruise to charge and discharge the battery. These two configurations minimize the difference in power between cruise power and available engine power, and thus lower the weight of the battery and electric motor.

An initial sizing of these two configurations found the 2E-T configuration was the better option for the mission. Figure 8.1(a) shows the maximum power required from the battery, and the weight of the engines, battery, electric motor, and fuel to fulfill the mission for both configurations. Each point plotted represents a vehicle design with a certain combination of features including which of the two engine configurations, the number of charge/discharge cycles, the power share ratio during cruise, and the battery power during hover. Grouping all designs with the same engine configuration together, two engines (2E-T) adds the least weight to the vehicle and requires substantially less power from the battery compared to one big and one

small engine (2E-1B1S). Figure 8.1(b) shows the minimum time spent charging or discharging the battery during the cycling process in cruise in relation to the weight. In general, the 2E-T configuration spends more time during each charge and discharge cycle, dropping the C-rate. This time spent charging and discharging directly affects the rate at which the engine power needs to be modulated. Throttling engines can be accomplished relatively quickly and safely. Cycling an engine on and off contributes additional wear on the engine and requires more time to ramp up [23]. The reduced battery power and C-rate further decrease the amount of cooling required to operate the battery and electric motor. Based on the low weight, and lower charging and discharging C-rates, the 2E-T configuration, consisting of a small battery and 2 throttling turbine engines, was selected.



(a) Battery power and weight required for each configuration.

(b) Battery charging/discharging time and weight required for each configuration.

Figure 8.1: Comparison of two hybrid configurations with each point representing a set of design parameters for each configuration.

8.2 Selection of Battery and Engine Sizes

Selecting the 2E-T configuration, additional detailed analysis was conducted to precisely select the engine, battery, and motor size to minimize vehicle weight. The battery power during hover and number of charge/discharge cycles during cruise were the primary parameters impacting the vehicle gross weight. Figure 8.2 shows the required weight of the engines, electric motor, battery, and fuel to fulfill the mission in relation to these two parameters. Three cycles contributes a greater weight increase compared to four and five cycles. Utilizing fewer cycles increases the battery capacity needed to power the one hour cruise segment. Figure 8.3(a) shows the battery charging C-rates during cruise in relation to the battery power output in hover for three, four, and five battery charge/discharge cycles. The battery C-rates coalesce together for 4 and 5 cycles for higher battery powers in hover. The same trend is observed for the discharge C-rates shown in Fig. 8.3(b). To minimize weight and maintain reasonable C-rates to prevent excessive heating from the battery and motor, *Mercury* selects to use a 162 kW battery with appropriately downscaled turbine engines and completes four battery charge/discharge cycles during cruise.

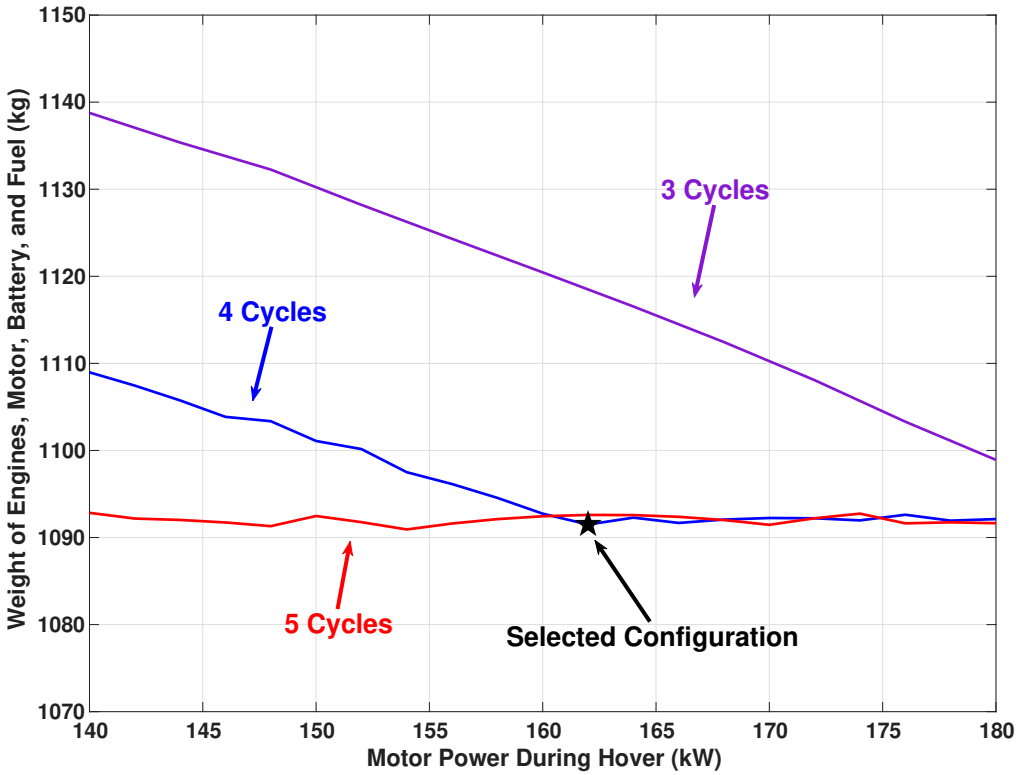
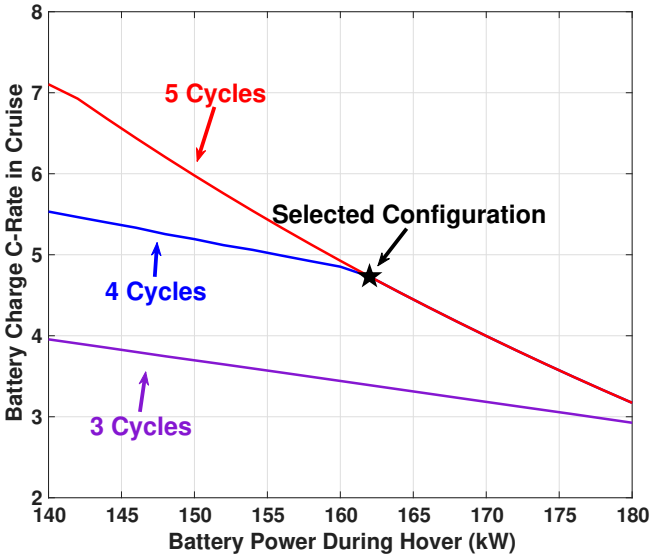
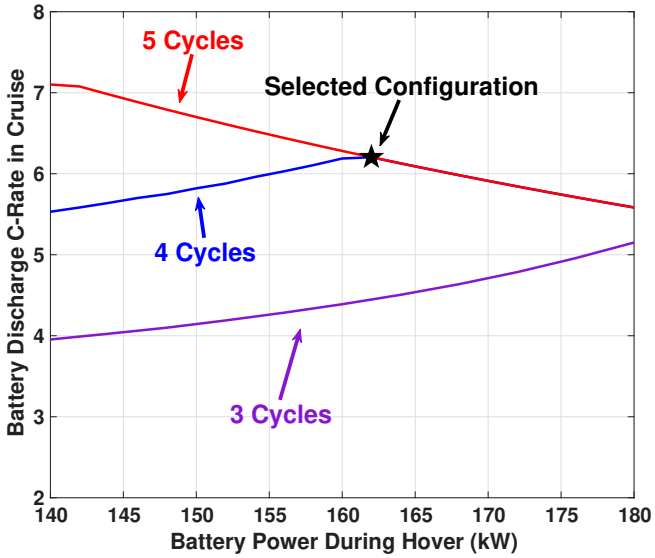


Figure 8.2: Required weight of hybrid propulsion components resulting from the amount of electrical power needed to hover for multiple charge/discharge cycles in cruise.



(a) Battery charge C-rates during cruise for multiple charge/discharge cycles.



(b) Battery discharge C-rates during cruise for multiple charge-discharge cycles.

Figure 8.3: Battery charge and discharge C-rates resulting from the amount of electrical power needed to hover for various charge-discharge cycle counts.

8.3 Battery and Motor Selection

Mercury uses the H3X HPM-180R electric motor due to its low motor weight, integrated inverter, and lightweight reduction gearbox. Requiring a maximum battery power of 162 kW, *Mercury* needs a battery pack with a capacity of at least 18 kWh based on RFP specifications. Considering the same 21700 NCA cells, the system configuration consists of a 250S5P pack. This pack is organized into five 50S5P modules to simplify the manufacturing process as shown in Fig. 8.4. Each module is enclosed in a CS-29.1353-compliant casing to prevent hazardous gas leakage. Battery specifications are summarized in Table 8.1.

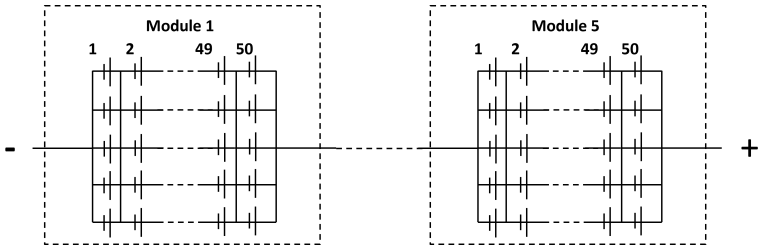


Figure 8.4: Mercury battery pack design.

Table 8.1: *Mercury* Battery specifications: cell, module, and pack

(a) Cell		(b) Module		(c) Pack	
Nominal Voltage	3.6 V	Cells/Group	5	Total Modules	5
Capacity	4 Ah	Groups/Series	50	Total Cells	1500
Maximum Discharge Rate	16 C	Cells/Module	300	Nominal Voltage	900 V
Cathode	NCA	Nominal Voltage	180 V	Capacity	20 Ah
		Capacity	24 Ah	Mass	85.2 kg
		Energy	3.6 kWh	Energy	18 kWh
				Energy Density	250 Wh/kg
				Power Density	2500 W/kg

8.4 Battery and Motor Cooling

The cooling system in *Mercury* shares the same components and design as *Hermes*. At peak power output in hover, the battery and motor produce 36.8 kW of heat. Throughout the mission, *Mercury* maintains battery and motor operating temperatures no more than 70°C (158°F) and 60°C (140°F) respectively. The operating conditions as well as the cooling system components are outlined in Table 8.2.

The cooling system is shown in Fig. 8.5. The battery and motor are connected in parallel, and the radiator and fan are placed in the tail of the fuselage. Placing the fan and radiator near the battery and motor intrudes into the cabin and limits passenger space. Thus, long coolant pipes are required, slightly increasing weight of the cooling system, the amount of coolant, and pump pressure required. To remove 36.8 kW of heat, the coolant (de-ionized water) flow is 35.2 L/min (9.3 gal/min). The flow rate is delivered by an AMT 5020-98 centrifugal pump operating at 3000 RPM and set to a pressure of 250 kPa (36.3 psi), circulating the coolant in 13 seconds. The pump is powered by the engines and motor through the central gearbox. An aluminum tube-and-fin heat exchanger is used as the radiator with dimensions of 240 mm × 240 mm × 25 mm. A Sparrow PF161V fan, powered by an independent motor, supplies 1.14 m^3/s (2415 CFM) of air to the radiator.

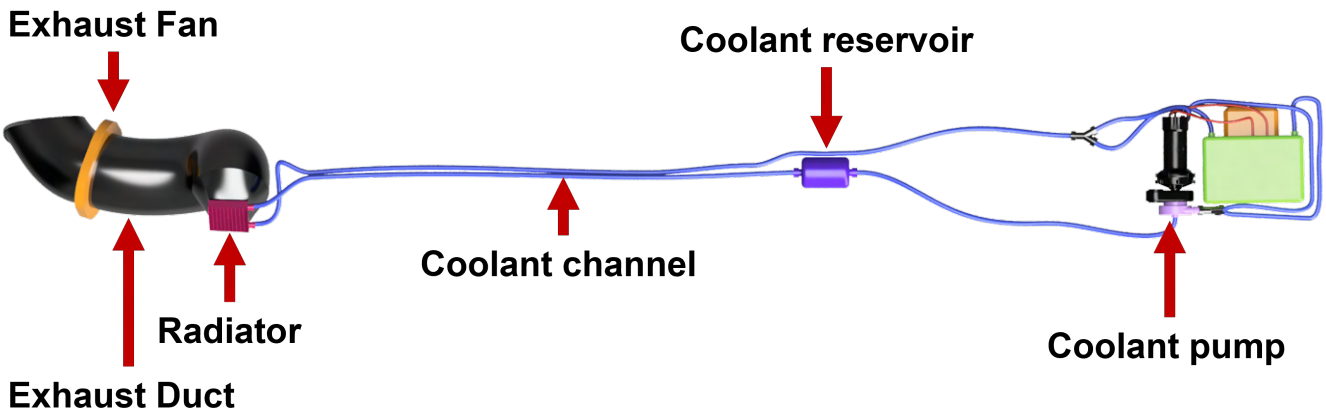


Figure 8.5: *Mercury* liquid cooling system for battery and motor.

Table 8.2: *Mercury* Cooling System

Components		Value	
Peak Waste Heat		36.8 kW	125000 BTU/hr
Battery Temperature Limit		70°C	158°F
Radiator			
	Weight	3.7 kg	8.2 lb
	Material	Aluminum	
Fan			
	Weight	9.1 kg	20 lb
	Power	250 W	0.33 HP
	Flow Rate	1.14 m^3/s	2415 CFM
Coolant		De-ionized Water	
	Weight	12.3 kg	27.1 lb
	Pump Flow Rate	35.2 L/min	9.3 gal/min
	Pump Pressure	250 kPa	36.3 psi
	Pump Power	1.1 kW	1.5 HP

8.5 Fuel System

The fuel system in *Mercury* has a combined fuel capacity of 640 kg (1410 lb) across seven fuel bladders within the wing, only four of which are shown in Figure 8.6. Fuel tank 1 spans the width of the fuselage and extends into both sides of the wing. The fuel system is designed with the same emphasis on safety as *Hermes*: each fuel bladder spans between two ribs within the wing box spar and are interconnected using tubes with frangible couplings, effectively forming one single fuel tank with seven redundant compartments. The fuel bladders are filled through a fuel cap on the second outboard bladder, and an electrically-powered fuel pump housed in the nacelle is used to feed the fuel to the engine. In the case of main fuel pump failure, a backup engine-driven pump is activated.

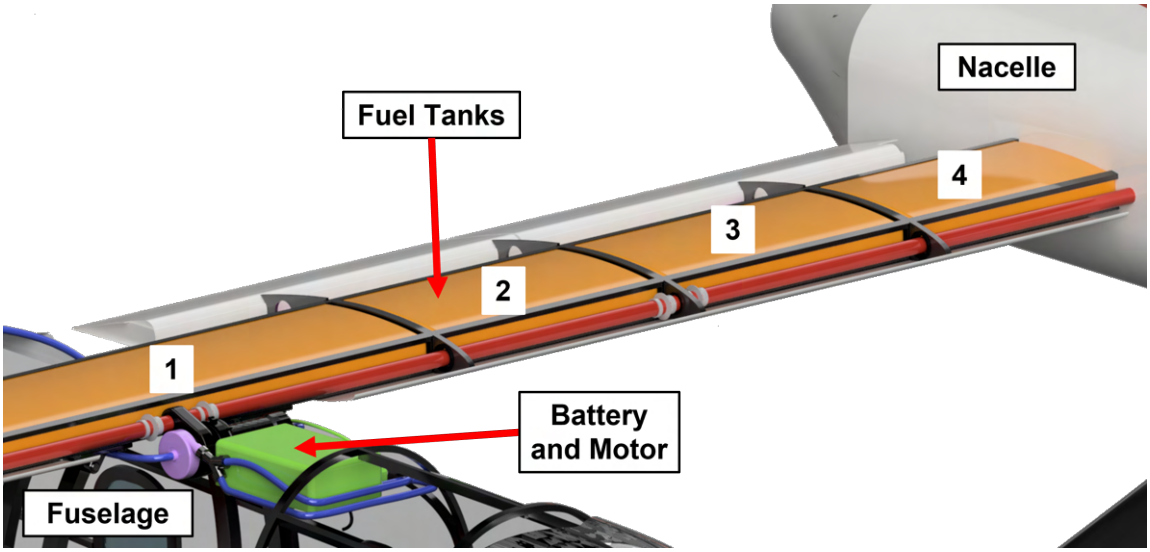


Figure 8.6: *Mercury* fuel bladders (orange).

8.6 Mission Configuration

The mission operating conditions for *Mercury* are specified in Table 8.3. The mission expends 553 kg (1220 lb) of fuel. *Mercury* carries an additional 62 kg (136 lb) of fuel in accounting for a 10% reserve. In total, 615 kg (1355 lb) of fuel is required to fulfill the RFP mission spanning 86 minutes. The majority of the fuel, 408 kg (899 lb), is consumed during the cruise segment.

Mission Segment	**Atmospheric Conditions**	**Time**	**Speed**	**Power Required**	**Fuel Use**
		min	m/s (kt)	kW (HP)	kg (lb)
HOGE	1219 m / 35°C 4000 ft / 95°F	5	0	1160 (1555)	36 (80)
Climb	ISA	5.5	64 (125)	1014 (1359)	39 (87)
Cruise	ISA 3048 m / 10000 ft	60.7	156 (303)	1047 (1404)	408 (898)
Descent	ISA	10	64 (125)	448 (601)	33 (72)
HOGE	ISA Sea Level	5	0	949 (1300)	37 (82)
Reserve	-	-	-	-	62 (136)
Total	-	86.2	-	-	615 (1355)

Table 8.3: Mission parameters for *Mercury*

Battery usage throughout the mission is outlined in Table 8.4. During the mission, the battery is discharging in the entire initial hover segment, four times in cruise, and the entirety of the final hover segment. The battery is recharged during the climb segment, three times in cruise, and during the descent segment when excess power from the engines is redirected into the battery for later use. The battery outputs 162 kW (220 HP), its highest rating, during the initial hover segment, providing 14% of hover power required. The climb segment recharges the battery at 148 kW (201 HP) within 5.5 minutes. Setting the engines to nearly MCP to recharge the battery and climb as fast as possible, reduces overall fuel consumption because the

specific fuel consumption is low. The cruise segment throttles the engines between the maximum continuous power (MCP) of 1,127 kW (1,532 HP) to 942 kW (1,281 HP), a 19.6% reduction. At MCP, the engines are recharging the battery with 80 kW (109 HP) of excess power, and at reduced throttle, the battery is discharging at 105 kW (143 HP) to supplement the reduced engine power, providing 10% of required cruise power. The descent segment recharges the battery for use in the final hover segment. The turboshaft engines alone can power the entirety of the cruise segment, but utilizing the hybrid system reduces fuel consumption. The complete distribution of power required, operating power from the engine, and battery usage is depicted in Fig. 8.7.

Mission Segment	**Time per Cycle**	**Number of Cycles**	**C-rate**	**Battery Power**	**Power Share Ratio**	**State of Charge**
	min			kW (HP)	%	%
HOGE, Discharge	5	1	9.5	162 (220)	14	21
Climb, Charge	5.5	1	8.2	148 (201)	15	100
Cruise, Charge	10.03	3	4.4	80 (109)	8	100
Cruise, Discharge	7.65	4	6.2	105 (143)	10	21
Descent, Charge	10	1	4.4	80 (109)	18	100
HOGE, Discharge	5	1	9.5	162 (220)	17	21

Table 8.4: *Mercury* battery usage during the mission.

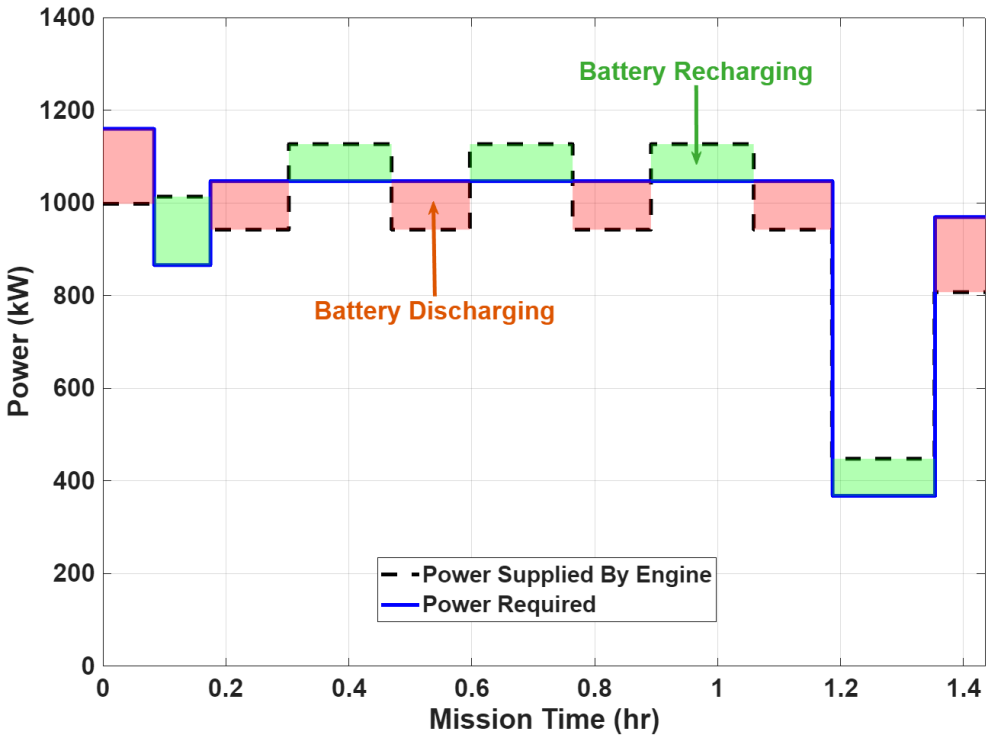


Figure 8.7: *Mercury* mission power required and power supplied from the engines.

9 Mercury Rotor Design

The proprotor is the most aeromechanically challenging component of a tiltrotor, as it must perform efficiently as both a helicopter rotor in hover and as a propeller in cruise. These two operating conditions impose fundamentally opposing design requirements: hover favors a low twist and low disk loading, while cruise demands a high twist and high disk loading. The RFP mission requirements specify hover at 1,219 m / 35°C (4,000 ft / 95°F or 4K/95) and cruise at 156 m/s (260 KCAS, 303 KTAS) at 3,048 m (10,000 ft) ISA. The XV-15 baseline rotor, retained in *Hermes*, shows degradation in performance under these flight conditions, which motivated detailed rotor optimization for the phase 2 aircraft, *Mercury*. The rotor design navigates this hover-cruise trade-off through a two-step optimization strategy. In accordance to the RFP, the rotor diameter and blade count for *Mercury* were constrained to match the XV-15 baseline: three blades of diameter 7.62 m (25 ft).

9.1 Blade Aerodynamic Design

Hermes retained the XV-15 baseline proprotor, with five NACA 64-series airfoil sections distributed along the blade span. The thick inboard sections provide the structural strength required to carry the large centrifugal and flapwise bending loads, while the thinner outboard and tip sections are suited for aerodynamic efficiency in the high-Mach cruise environment. The blade airfoil distribution for *Hermes* is summarized in Table 9.1.

Table 9.1: *Hermes* / XV-15 rotor blade airfoil sections.

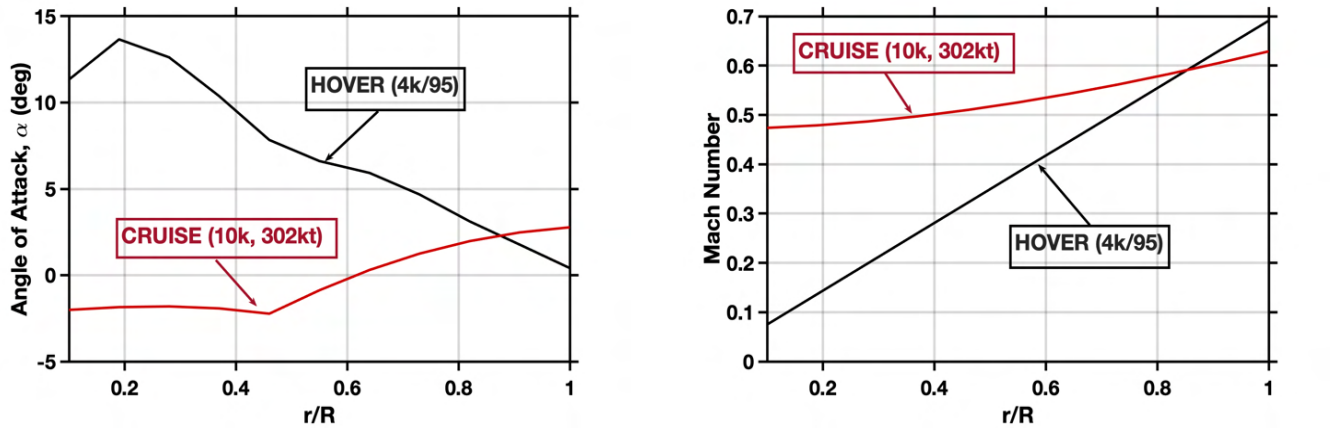
r/R	Airfoil	t/c (%)	Spanwise Role
0.09	NACA 64-935	35	Root structural transition
0.17	NACA 64-528	28	Inboard
0.51	NACA 64-118	18	Mid-span
0.80	NACA 64-(1.5)12	12	Outer
1.00	NACA 64-208	8	Tip

The spanwise distributions of sectional angle of attack and Mach number for the *Hermes*/XV-15 baseline rotor were determined using BEMT for both airplane mode cruise at 156 m/s (303 kt) and 3,048 m (10,000 ft) ISA, and hover at 4K/95, and are shown in Fig. 9.1. In cruise, the inboard sections (r/R $\approx$ 0.09–0.40) operate at low angles of attack ($\alpha \approx -3.5°$ to $-1.0°$) and low sectional Mach numbers ($M \approx 0.45$–0.5). The outboard and tip sections (r/R $\approx$ 0.60–1.00) carry the majority of the propulsive load, operating at positive angles of attack ($\alpha \approx 0°$ to $+2°$) and higher Mach numbers ($M \approx 0.5$–0.65), with the advancing side ($\psi = 90°$) reaching the highest values. In hover, the inboard sections operate at the highest angles of attack ($\alpha \approx 10°$–$13°$) due to lower local velocity and high induced inflow, while the tip sections operate near $\alpha \approx 2°$–$3°$ at Mach numbers approaching $M \approx 0.65$.

The proprotor aerodynamic design for *Mercury* proceeded in two sequential steps: airfoil section optimization followed by blade planform optimization. A similar two-step optimization methodology was applied in the design of the V-22 proprotor [24].

9.1.1 New AGRC-Series Airfoil Design

In the first step, four of the five blade sections NACA 64-208 (tip), NACA 64-(1.5)12 (outer), NACA 64-118 (mid), and NACA 64-528 (inboard) were individually redesigned using CST (Class-Shape Transformation) [25] parameterization, while the root section NACA 64-935 was retained unchanged owing to



(a) Sectional Angle of Attack.

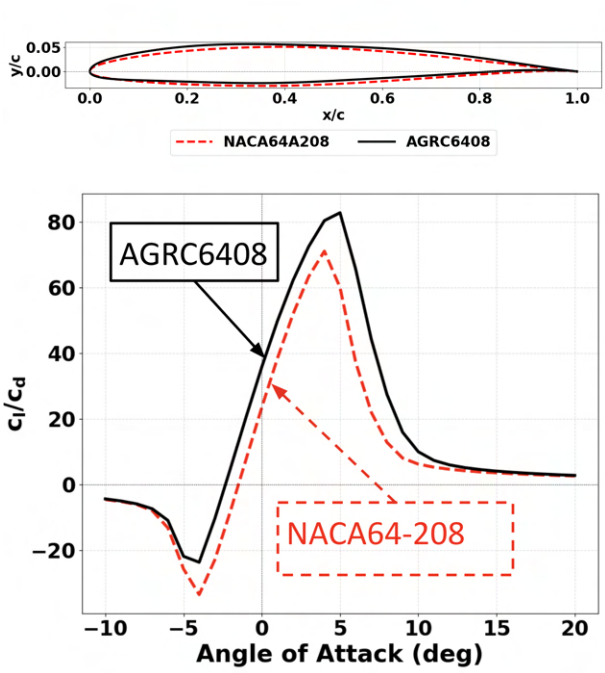
(b) Sectional Mach Number.

Figure 9.1: Spanwise sectional angle of attack and Mach number in hover and cruise modes of the *Hermes*.

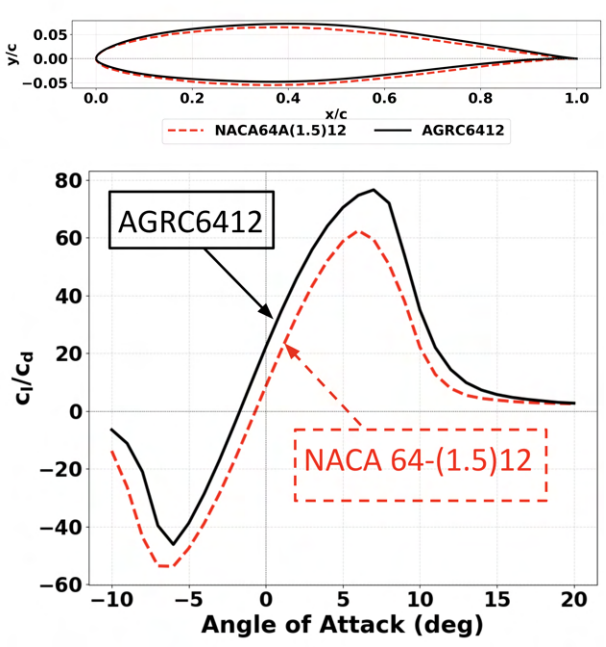
its predominantly structural role and negligible aerodynamic contribution at the blade root. A Genetic Algorithm [26] was employed to search the design space over 50 generations with a population size of 80, requiring 3,200 surrogate evaluations per section, in combination with the Alfred Gessow Rotorcraft Center (AGRC) Airfoil Surrogate [27], a neural network-based surrogate that evaluates aerodynamic polars in milliseconds in place of direct CFD calls, making this evaluation budget computationally tractable. The objective for each section was to maximize c_l/c_d at its respective operating angle of attack and Mach number as determined from the BEMT. The four optimized sections are designated AGRC-6408 (tip), AGRC-6412 (outer), AGRC-6418 (mid), and AGRC-6428 (inboard), retaining the NACA 64-series family lineage. The geometry modifications alter the camber and thickness distribution of each section, directly influencing the pressure recovery and boundary layer behavior, which in turn shifts the lift curve and reduces profile drag, improving c_l/c_d. The airfoil geometries and the corresponding c_l/c_d improvement for each section are shown in Fig. 9.2. The aerodynamic performances of all baseline and optimized airfoil sections were evaluated using the in-house Hamiltonian Strand Navier-Stokes CFD solver (HAM2D) [28].

9.1.2 Blade Planform Optimization

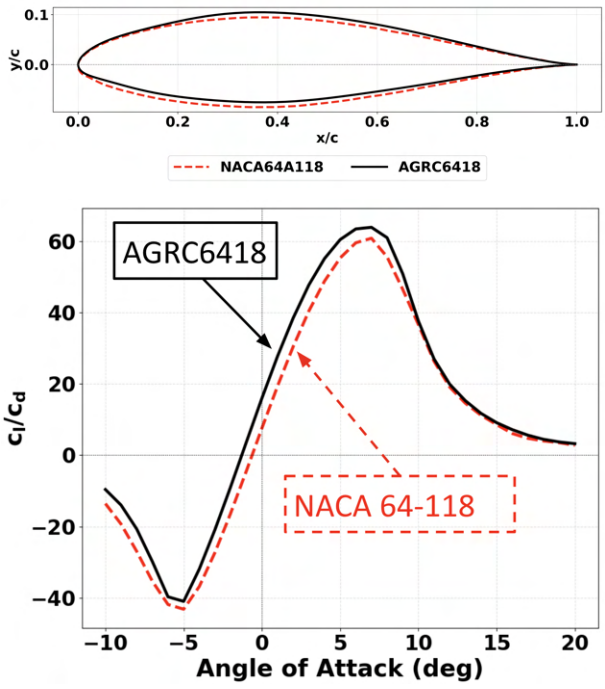
In the second step, different blade geometries were generated by varying the sectional taper, twist distribution, and airfoil transition locations. The optimal blade planform was then identified using a Non-dominated Sorting Genetic Algorithm (NSGA-II) [29] with a population size of 40 over 40 generations, requiring a total of 1,600 evaluations, each solving the BEMT with vehicle trim closure to convergence. The objective function at each design point was evaluated using the BEMT with vehicle trim closure, ensuring the planform is optimized for trimmed flight rather than isolated rotor performance. The rotor solidity was constrained to the XV-15 baseline, $\sigma = 0.089$, within the optimization. The two objectives were Figure of Merit (FM) in hover at 4K/95 and propulsive efficiency, η_p, in airplane mode cruise at 156 m/s (303 kt), 3,048 m (10,000 ft) ISA. The knee-point design on the resulting Pareto front was selected as the final blade geometry, balancing hover and cruise performance. The Pareto front is shown in Fig. 9.3, and comparisons of the optimized twist and taper against *Hermes* are shown in Fig. 9.4. The *Mercury* proprotor blade planform is shown in Fig. 9.5, illustrating the tapered chord distribution and the four optimized AGRC airfoil sections. The performance improvement achieved through the two-step optimization is reflected in both primary flight conditions. In hover, the FM improved from 0.79 for *Hermes* to 0.84 for *Mercury*. In cruise, the propulsive efficiency increased from 0.81 to 0.83.



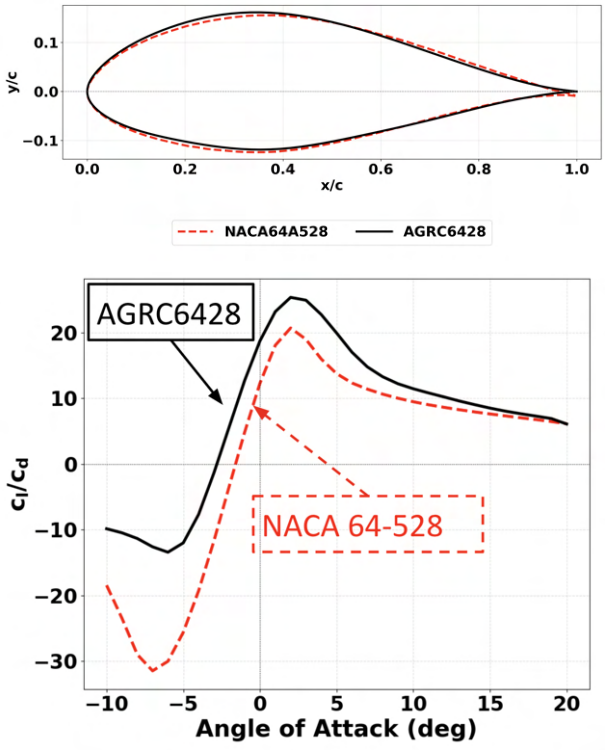
(a) Tip: NACA 64-208 vs. AGRC-6408 geometry and c_l/c_d vs. α.



(b) Outer: NACA 64-(1.5)12 vs. AGRC-6412 geometry and c_l/c_d vs. α.



(c) Mid: NACA 64-118 vs. AGRC-6418 geometry and c_l/c_d vs. α.



(d) Inboard: NACA 64-528 vs. AGRC-6428 geometry and c_l/c_d vs. α.

Figure 9.2: Geometry and aerodynamic performance of baseline and optimized rotor blade airfoils.

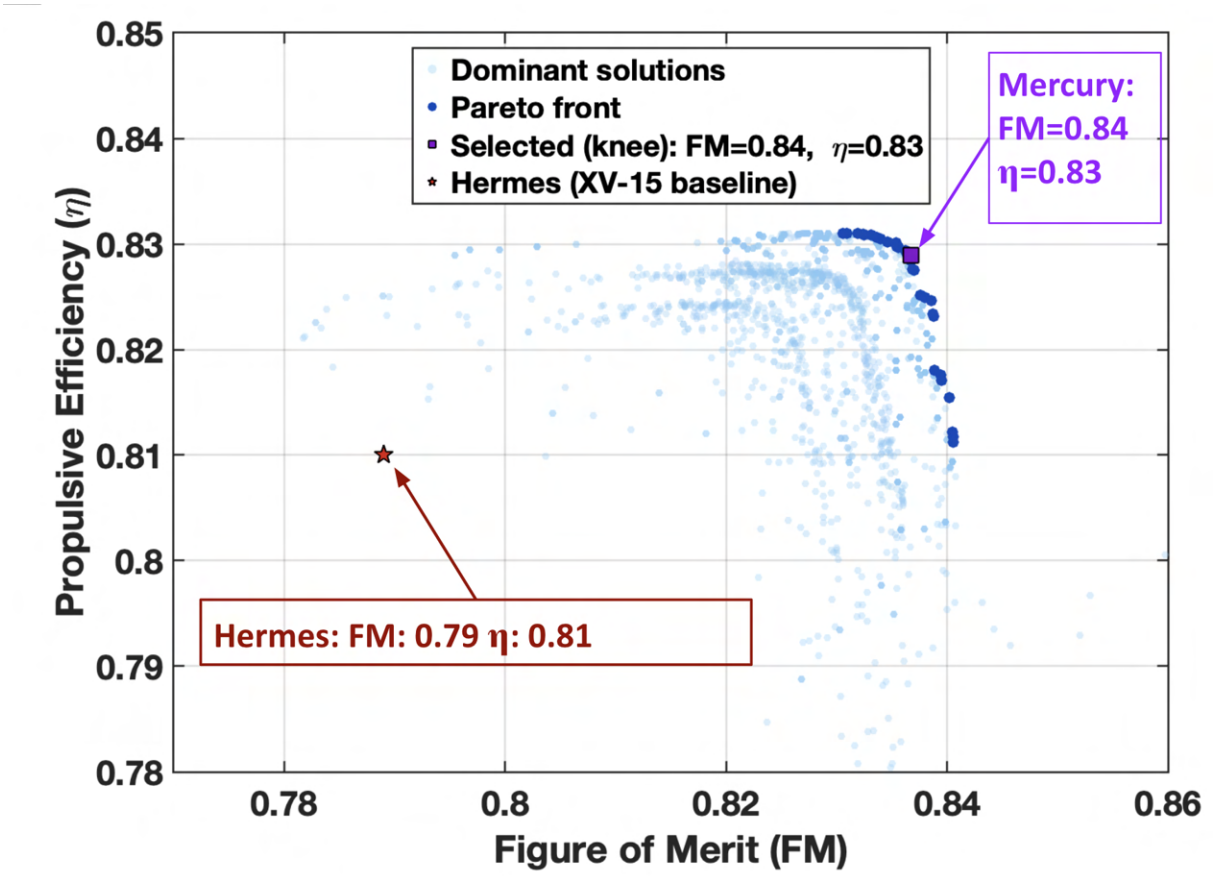
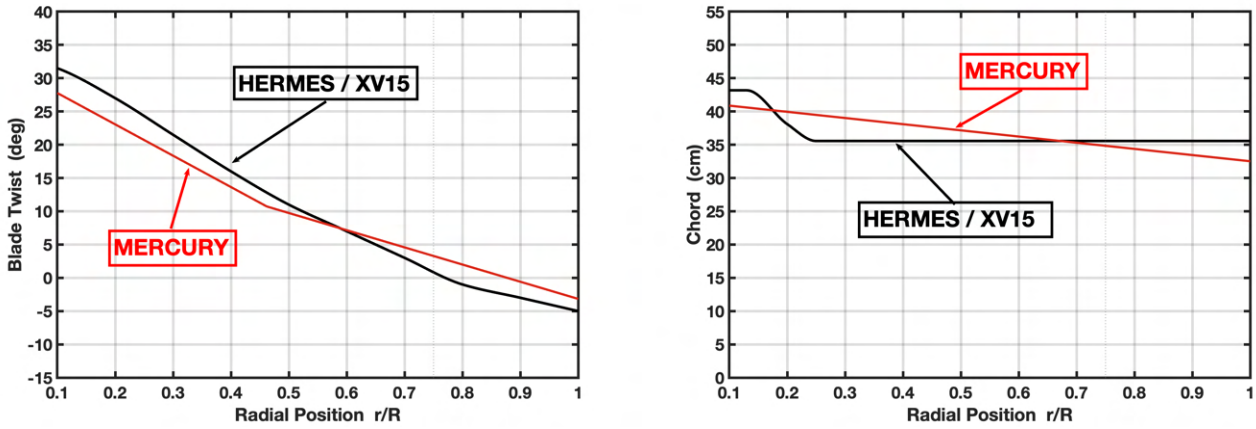


Figure 9.3: *Mercury* proprotor planform optimization Pareto front.



(a) Twist distribution.

(b) Chord distribution.

Figure 9.4: *Hermes* and *Mercury* proprotor twist and chord distribution.

9.2 Blade Structural Design

The *Mercury* proprotor blades are constructed from carbon fiber/epoxy composite, with a D-spar and skin designed to carry the centrifugal and aerodynamic loads in flight. The gimbaled stiff in-plane configuration eliminates ground and air resonance without the need for lag dampers.

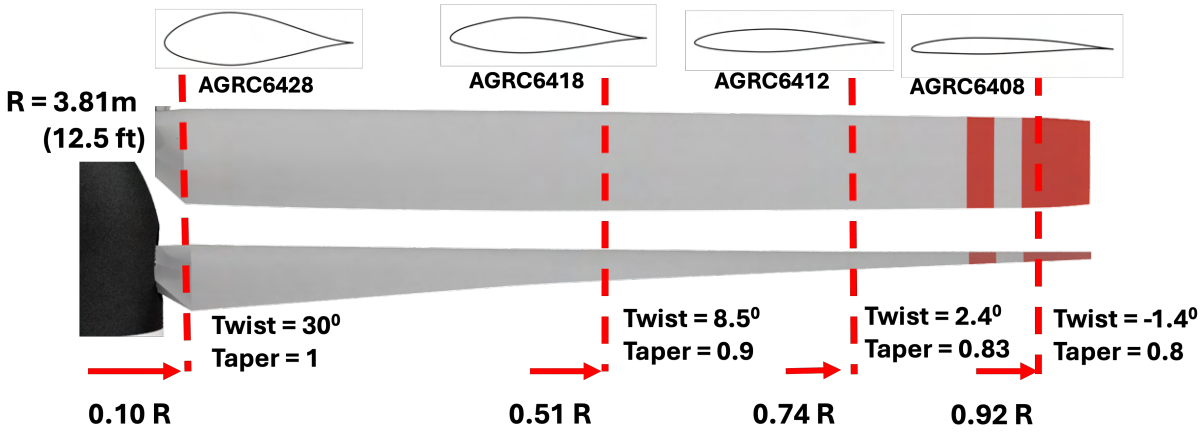


Figure 9.5: *Mercury* proprotor blade planform with airfoil section transitions.

9.2.1 Structural Design Approach

An in-house finite element cross-sectional analysis tool was used to design and compute blade stiffness and inertial properties along the blade span considering varying airfoils, skin and spar ply orientations, taper and twist, leading edge masses, and ply drop-offs. The tool generates finite element meshes at each cross-sectional station, incorporating composite ply layups, ply thicknesses, and the precise airfoil and spar geometries to compute the sectional flap stiffness (EI_N), chordwise stiffness (EI_C), torsional stiffness (GJ), and mass distribution directly. The design parameters included the shape and location of the spar, spar and skin layups, leading-edge weight mass, and material properties for all blade components. To prevent pitch-flap instability, leading-edge weights are included to maintain the blade center of gravity at the quarter-chord (0.25c). The resulting spanwise properties were used to compute the blade natural frequencies and generate the fan plot. The structural design was carefully tailored so that the flap, lag, and torsional frequencies avoid per-rev crossings at all flight conditions.

9.2.2 Internal Blade Structure

A cross-sectional view of the blade internal structure is shown in 9.6. The primary structural member is a composite D-spar composed of 7 unidirectional T300 graphite/epoxy plies in the following layup: [0/90/0/0/0/90/0]. The [0°] fibers carry the dominant centrifugal and spanwise bending loads, while the [90°] plies are intermixed to suppress interlaminar delamination. The D-spar extends chordwise from the leading edge to 0.28c. The blade skin consists of two plies of T300 graphite/epoxy in a balanced $[\pm 45°]_2$ layup, providing the majority of the torsional stiffness. The center of gravity of the blade cross section was placed at the quarter chord (0.25) using leading edge tungsten weights. These weights are split into separate elements to prevent any spanwise stiffness contribution. Rohacell 51 foam fills the interior of the D-spar and forward blade cavity. Rohacell 31 foam of lower density fills the aft cavity to preserve the aerodynamic profile without introducing a rearward mass offset. A 4% chord unidirectional E-glass/epoxy wedge runs along the trailing edge of the blade to providing sufficient surface area to bond the upper and lower skins and resist delamination. Fiber-reinforced composite materials were chosen for the blade structure because of their superior specific strength, fatigue characteristics, and capability to conform to complex geometries. Rohacell foam was chosen over a metal honeycomb core structure due to its lower cost and ease of machining. Unlike Rohacell, cutting metallic honeycomb structures often requires extensive post-processing to conform to the blade skin. A thin copper mesh is wrapped over the blade skin to create a path for current to flow to the rotor hub in the event of a lightning strike, in accordance with

14 CFR 25.581 [30]. A stainless steel strip is placed on the leading edge for abrasion resistance.

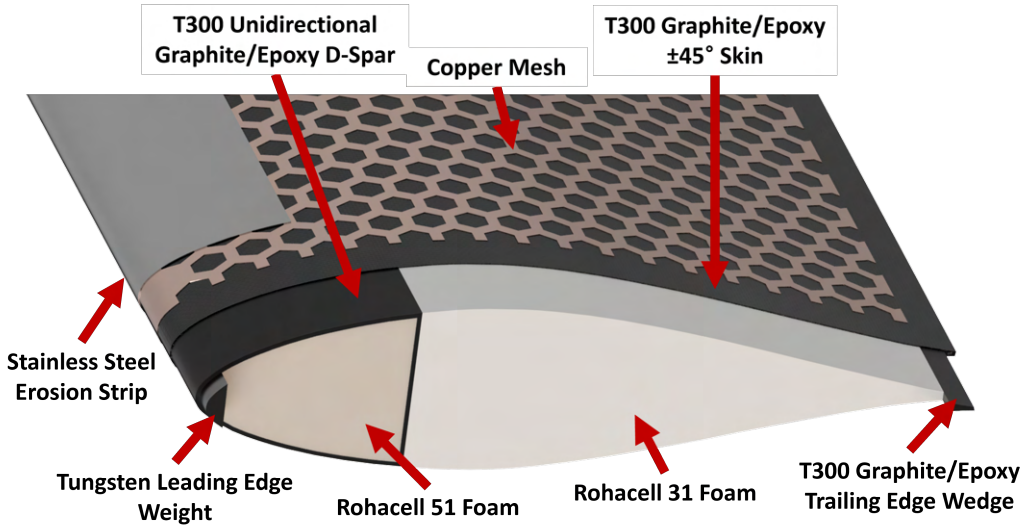


Figure 9.6: Proprotor blade cross-section.

9.2.3 Blade Root and Hub Attachment

The blades attach to a gimbaled hub, which removes the one per rev flap bending moment from the blade root, reducing mean root stresses relative to a hingeless design. Centrifugal loads are transferred through titanium bushings at the blade root insert into the hub retention bolts. The D-spar graphite epoxy plies wrap continuously around the titanium insert, maintaining fiber continuity from the root attachment into the outboard sections of the blade. The D-spar near the root shortens in the chordwise direction, lowering chordwise stiffness to place the first lag frequency at 1.6/rev, reducing in-plane blade loads.

9.2.4 Blade Manufacturing

The D-spar and titanium root insert are manufactured as a continuous assembly to maintain fiber continuity. The leading-edge Rohacell 51 foam is first machined to the internal D-spar geometry. Tungsten leading-edge weight segments are inserted flush into pre-cut foam slots along the blade span. T300 graphite/epoxy fiber tows are then applied using automated fiber placement, sweeping continuously from tip to root and back, wrapping around the titanium root insert and following the inboard spar taper profile. This automated process enables accurate capture of the high blade twist, multi-section airfoil transitions, and the varying spar shape inboard. The complete spar and insert assembly is then cured in a mold.

Following spar cure, the aft Rohacell 31 foam core is machined to the airfoil profile and bonded to the rear of the D-spar. The trailing-edge E-glass/epoxy wedge plies are then applied using automated fiber placement (AFP). The two [±45°] graphite/epoxy skin plies are wrapped continuously over the full blade assembly. Due to the high blade twist and airfoil section transitions, draping techniques are employed to ensure a wrinkle and void-free laminate. A preformed stainless steel erosion strip and copper mesh are placed over the leading edge and blade skin surface respectively. The blade is then placed in a mold with a shallow recess at the leading edge to accommodate the erosion strip. Final curing is completed in an autoclave.

9.2.5 Three-Dimensional Stress Analysis

A three-dimensional structural analysis of the blade was performed using the US Army/University of Maryland solver X3D [31] to capture dynamic stress distributions and verify structural integrity of the blade. This solver employs three-dimensional finite elements to model the structure from first principles. Results are shown for hover at gross takeoff weight (GTOW) with a trimmed collective of 9°. Figure 9.7 shows the axial (bending) stress distribution along the blade. Three cross-sections are highlighted at 25% R, 50% R, and 75% R, corresponding to three distinct airfoil profiles. The highest stresses are observed in the D-spar near the root. Elevated stresses are also present at the trailing edge across the span due to high geometric twist of the blade. The maximum tensile stress in the spar is approximately 450 MPa, giving the blade a factor of safety greater than 4.

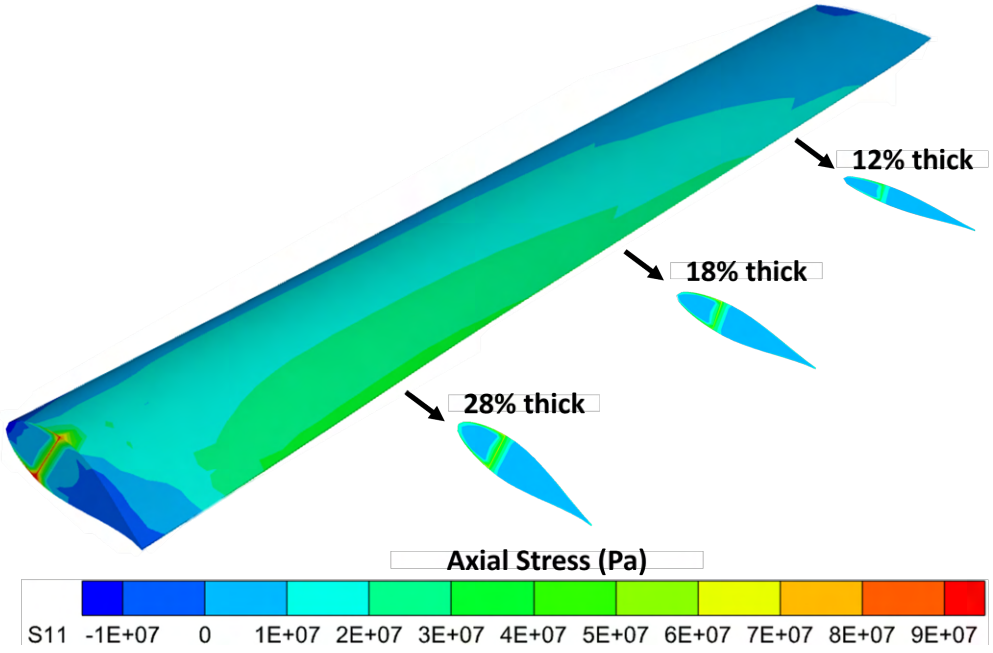
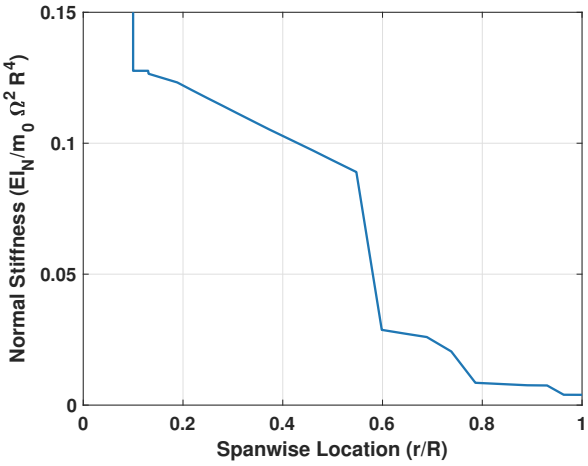


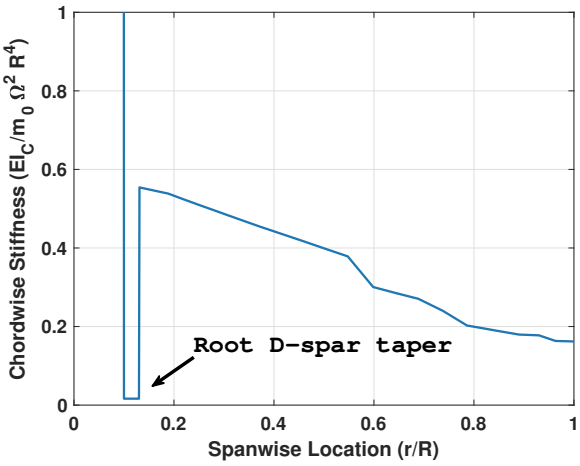
Figure 9.7: Rotating bending stresses on *Mercury* blade in hover.

9.2.6 Blade Sectional Properties

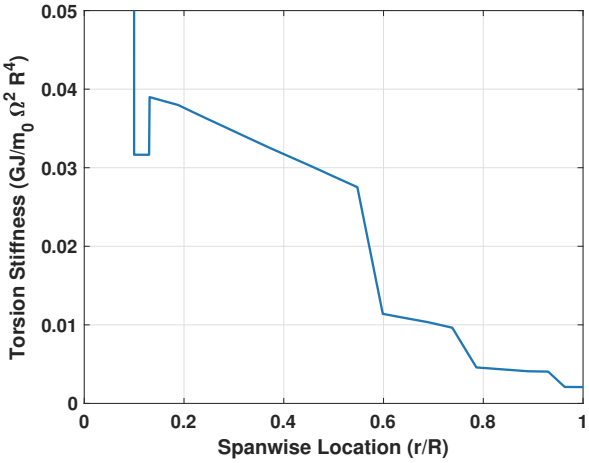
Each blade weighs 16.1 kg (35.4 lb). The non-dimensional flap stiffness, chordwise stiffness, torsional stiffness, and mass distributions are shown in Fig. 9.8. The blade attachment is at 10% R, and the stiffness and mass properties inboard of this station are dominated by the hub. Outboard of the root cutout, the skin, spar, and leading-edge weights determine the sectional properties, with spanwise variations due to airfoil section changes and blade taper. The large reduction in chordwise stiffness from the inboard D-spar taper sets the first lag frequency to 1.6/rev.



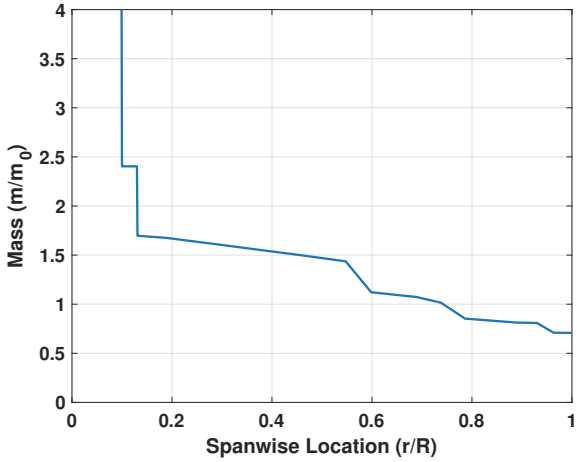
(a) Flap stiffness distribution.



(b) Chordwise stiffness distribution.



(c) Torsional stiffness distribution.



(d) Mass distribution.

Figure 9.8: Non-dimensional blade sectional property distributions.

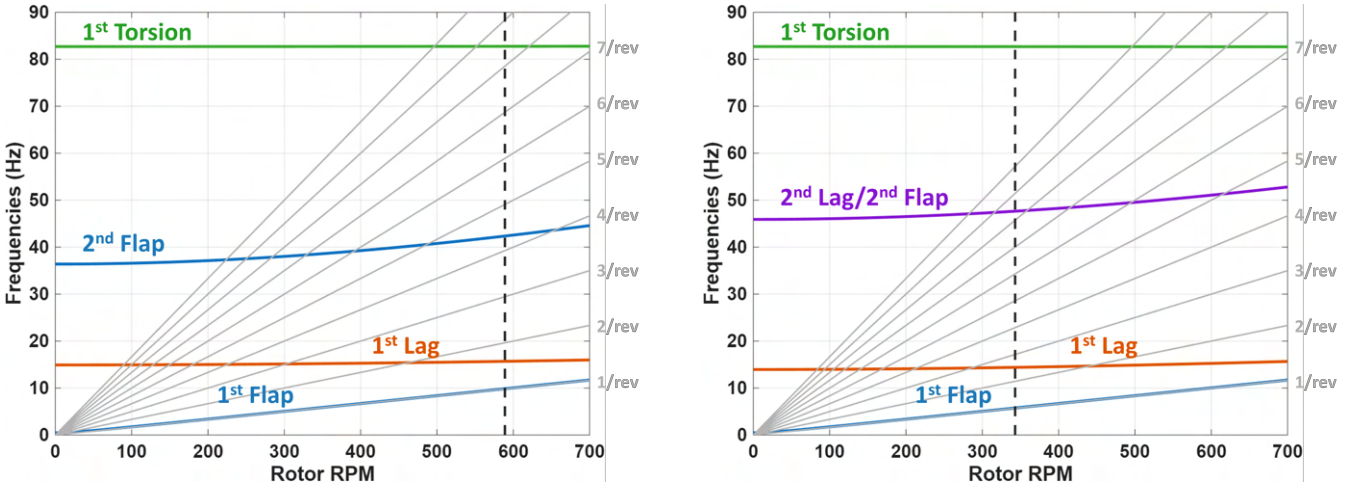
Fan plots are shown for hover (9.2° collective) and cruise (56.1° collective) in Fig. 9.9. As collective increases, flap stiffens and lag softens. The large blade twist couples the modes significantly, the dominant contribution is listed first (Table 9.2 and 9.3). The first mode corresponds to the 1/rev gimbaling action of the hub. All blade modes are adequately separated from per-rev crossings across the full operating RPM range.

Mode	Freq. (/rev)
1st Flap (Gimbal)	1.00
1st Lag	1.60
2nd Flap	4.32
1st Torsion	8.43

Table 9.2: Blade natural frequencies in hover, 9.2° collective, 589 RPM.

Mode	Freq. (/rev)
1st Flap (Gimbal)	1.01
1st Lag	2.52
2nd Lag/2nd Flap	8.34
1st Torsion	14.46

Table 9.3: Blade natural frequencies in cruise, 56.1° collective, 343 RPM.



(a) Hover fan plot, 9.2°collective.

(b) Cruise fan plot, 56.1°collective.

Figure 9.9: *Mercury* fan plots at hover and cruise operating conditions.

9.3 Rotor Aeroelastic Stability

The *Mercury* gimbaled proprotor is free from the four classical rotor aeroelastic instabilities: ground resonance, air resonance, flap-lag flutter, and pitch-flap flutter.

Ground and air resonance are dynamic instabilities caused by coupling between the rotor regressive lag modes and the fuselage structural modes, on the ground and in flight respectively. *Mercury*'s gimbaled proprotor is stiff in-plane, placing the lag frequency above the 1/rev, eliminating the possibility of regressive lag mode coalescence with fuselage modes. Therefore, *Mercury* is free from ground and air resonance, and additional lag dampers are not required.

Flap-lag flutter arises from Coriolis and aerodynamic coupling between the flap and lag degrees of freedom, and is exacerbated by high blade loading. The gimbaled hub introduces a $\delta_3 = -15°$ coupling that separates the flap and lag frequencies, eliminating flap-lag instability [32] at high forward speeds. The stiff in-plane design with separated flap and lag frequencies and large blade twist ensures that no flutter boundary exists within the operating blade loading range. Aerodynamic lag damping increases substantially in cruise, providing additional margin in forward flight.

Pitch-flap flutter is a dynamic instability driven by lift and centrifugal coupling about the blade pitch axis. Pitch divergence, the static counterpart, results from an offset between the aerodynamic center and the blade center of gravity. Both instabilities are eliminated by placing the blade chordwise center of gravity at the quarter-chord, coincident with the pitch axis and aerodynamic center. A high first torsional frequency above 8.4/rev provides additional margin against pitch-flap coupling across all operating rotor speeds.

9.4 Rotor Hub

Mercury retains the same gimbaled, stiff in-plane rotor hub developed for *Hermes*, described in detail in Section 6. The hub is based on the proven Bell Boeing V-22 design to replace the XV-15 universal joint with a constant-velocity joint formed by three elastomeric drive links. The drive links transmit torque while accommodating hub flapping up to 12°, forming a homokinetic constant-velocity joint that eliminates the 2/rev output velocity variation of the XV-15 universal joint and corresponding 2/rev pylon excitation. This enables *Mercury* to operate at 343 RPM in cruise, a 42% reduction from the hover rotor speed of

589 RPM, contributing to a 5.9% improvement in propulsive efficiency versus the XV-15, from $\eta_p = 0.78$ to $\eta_p = 0.83$.

10 Mercury Transmission

The most significant change in *Mercury's* transmission is the addition of a tilting mechanism for the rotor. This allows just the rotor to tilt vertically for hover rather than the entire nacelle, inspired from Bell's V-280 and Leonardo Helicopter's NGCTR tiltrotor designs. *Mercury's* rotor tilting mechanism consists of a series of bevel gears that pivot about a central axle, as shown in Fig. 10.1.

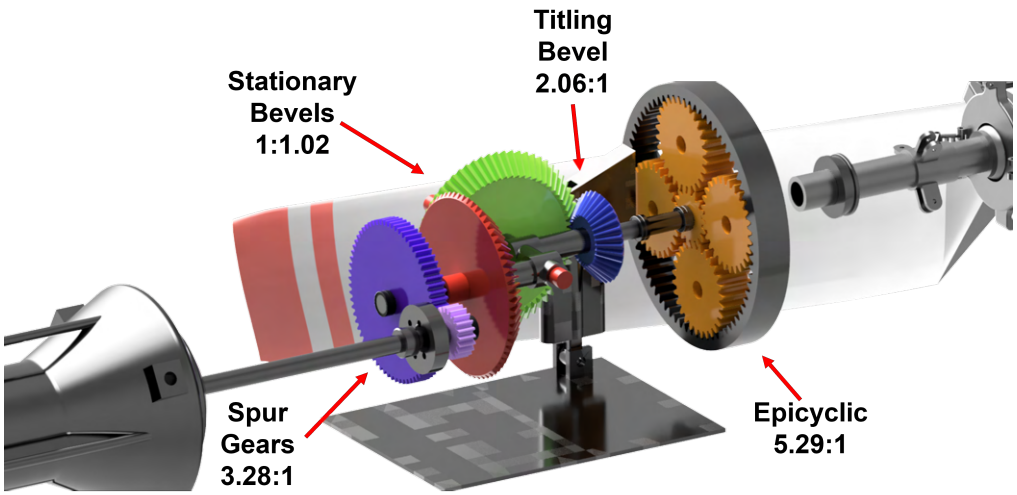


Figure 10.1: *Mercury* nacelle gearbox in cruise.

10.1 Gear Sizing

Similar to *Hermes*, the first reduction stage of *Mercury* steps the 20,000 RPM engine output down to 6,334 RPM (ratio 3.16:1) in hover. Maintaining high shaft speed at the tilting mechanism minimizes the torque reacted by the central bevel gears. The central bevel train applies a slight speed increase to 6,431 RPM using a hunting-tooth ratio (tooth counts with no common factors) to distribute contact wear uniformly across all mating tooth pairs. A secondary bevel gear, free to rotate about the tilt axis, provides a 2.06:1 reduction to 3,118 RPM while kinematically accommodating nacelle rotation during conversion. A final planetary stage performs the reduction to 589 RPM in hover (5.3:1), yielding an overall gearbox ratio of 34:1. The nacelle transmission is shown in Fig. 10.2.

10.2 Cross Shaft

Mercury's cross shaft dimensions are the same as *Hermes*, with a diameter of 60 mm (2.36 in). It now rotates at a slightly faster 6,431 RPM in hover and 3,745 RPM in cruise. This change slightly increases the frequency band, but remains well within safe margins as shown in Fig. 10.3.

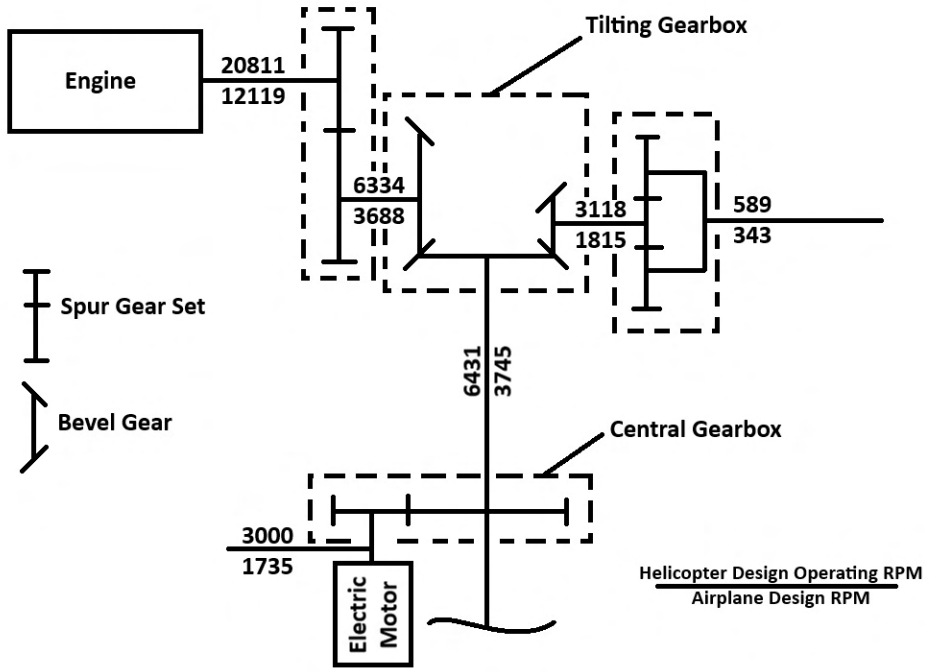


Figure 10.2: *Mercury*'s drive system architecture diagram.

Table 10.1: *Mercury's* Transmission Stage Gear Ratios

Gearbox		Teeth	Gear Module	Ratio	Efficiency
1st stage - Spur	Input	21	5	3.285	97%
	Output	69			
2nd stage - Bevels	From 1st Stage	65	5	0.984	97%
	To Cross Shaft	66		2.062	
	To Rotor - Rotating	32			
3rd stage - Planetary	Sun (Input)	17	7	5.294	98%
	Planet (Output)	28			
	Ring (Fixed)	73			

10.3 Central Gearbox

The central gearbox in *Mercury* is even simpler than in *Hermes* and the XV-15, as the straight wings allow the shaft to run directly from one nacelle to the other. Electric motor power is included using a pair of spur gears, shown in Fig. 10.4.

10.4 Gearbox Casing and Mounting

Unlike the fixed-nacelle casings on *Hermes*, *Mercury's* tilting rotor assembly requires a split-case architecture to accommodate the angle between the fixed wing structure and the rotating nacelle during conversion. The stationary and rotating casing halves interface at a precision-machined cylindrical surface, permitting

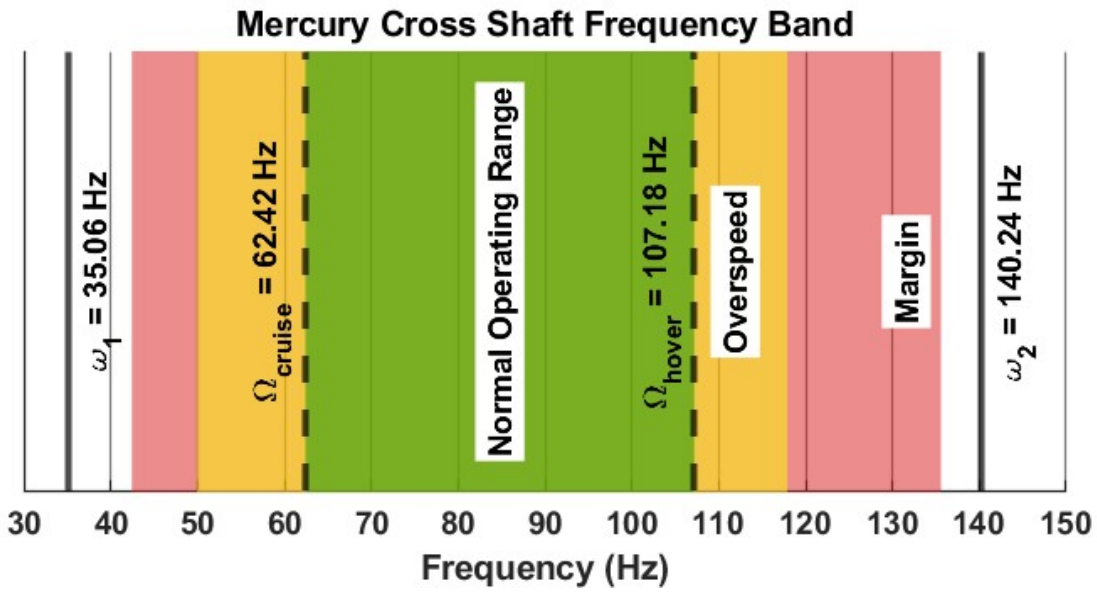


Figure 10.3: *Mercury* cross shaft first and second natural frequencies with operating RPM band.

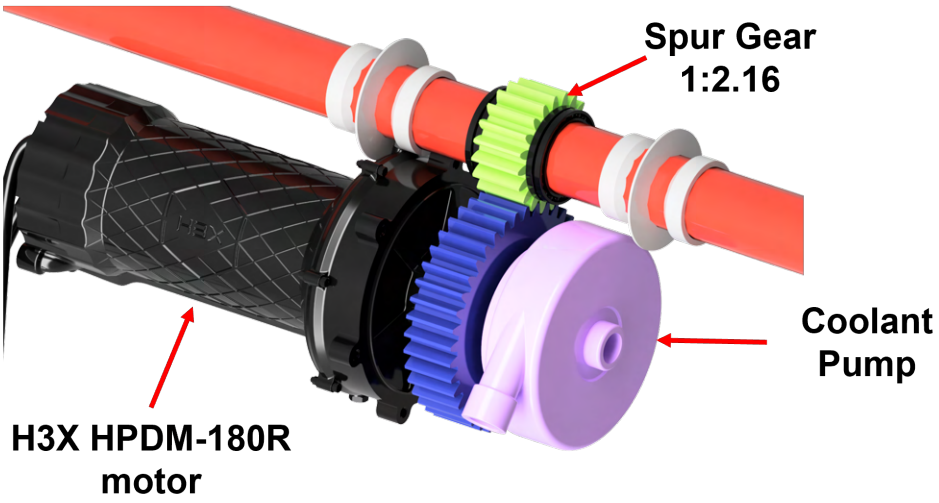


Figure 10.4: *Mercury* central gearbox cutaway, with highlighted spur gears and coolant pump.

rotation about the tilt axis while maintaining structural continuity. The moving and non-moving halves of the gearbox casing are joined together using a garter-spring-tensioned lip seal to contain oil inside and prevent leaks. The casing is designed as a stressed member, reacting rotor thrust, in-plane forces, and bending moments directly into the wing. This dual-use as a structural member is due to space limitations requiring a direct connection of the rotor lift rods to the gearbox casing.

11 Mercury Wing Design

The wing provides all vehicle lift in airplane mode. However, aeroelastic instabilities at high cruise speeds are common amongst tiltrotors, occurring when rotor fixed-frame frequencies coalesce with wing frequencies, a phenomenon known as whirl-flutter. The wing structure also carries the proprotor loads, engine,

fuel, and contains the interconnecting cross-shaft. For these reasons, tiltrotor wings are typically 20–26 % thick.

The structural design must withstand a 3.5 g limit load factor with a factor of safety of 1.5 in accordance with US Federal Aviation Regulations. This section describes the aerodynamic and structural design of the wing for *Mercury*, a 13% thick wing enabling a 17% improvement in wing L/D while remaining free from whirl flutter and carrying 3.5 g maneuver and 2 g hover loads with a factor of safety greater than 1.5.

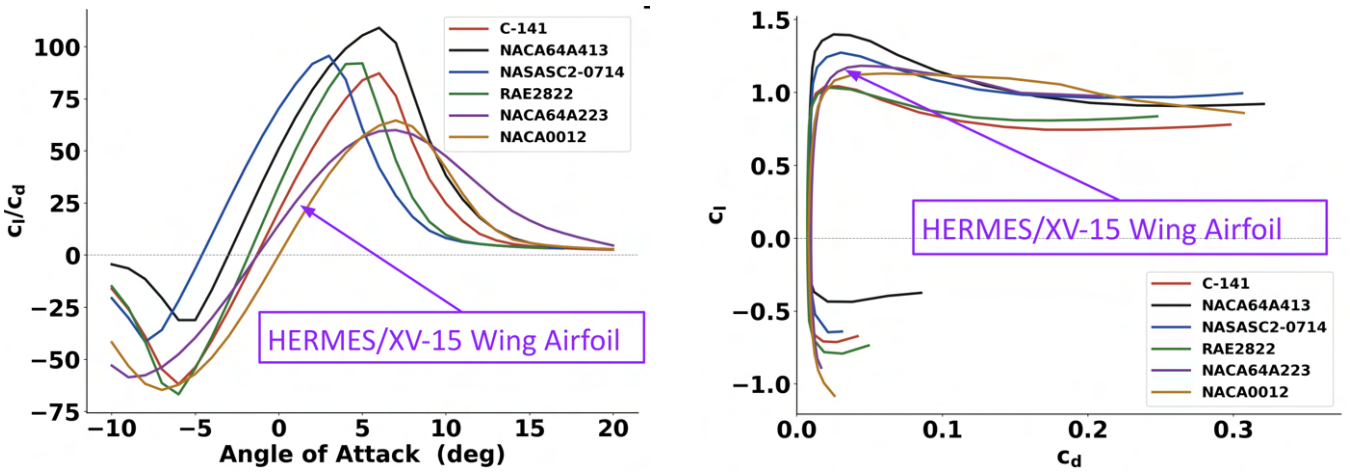
11.1 Wing Aerodynamic Design

This section details the aerodynamic design of the wing for *Mercury*, with the aim of improving aerodynamic efficiency over the *Hermes*/XV-15 baseline.

11.1.1 Wing Airfoil Design

The *Hermes* wing uses the 23 % thick NACA 64A223 airfoil, as in the XV-15 baseline, as required by phase 1 of the RFP. The relatively high thickness-to-chord ratio served two purposes: it provided the structural stiffness needed to suppress whirl-flutter instabilities, and allowed fuel to be stored within the wing structure.

For *Mercury*, initial studies were conducted based on wind-tunnel test data at the University of Maryland (UMD) and in-house comprehensive analysis to determine the minimum thickness-to-chord ratio at which whirl flutter remained suppressed at cruise altitude. These analyses showed that a 13% thick airfoil with proper tailoring of pylon properties was sufficient, opening the possibility of a thinner, lower-drag wing section. A comparison of candidate airfoils with t/c ratios in the range of 12-14 % was therefore carried out, with selection criteria based on the lift coefficient required during cruise, and the width of the drag bucket surrounding the operating cruise c_l to minimize sensitivity to off-design conditions. Five candidate airfoils with a thickness-to-chord ratio of approximately 12-14 % were evaluated at the cruise Mach number of $M = 0.47$ using the in-house Hamiltonian Strand Navier-Stokes CFD solver (HAM2D): C-141 (Lockheed airfoil), NACA 64A413, NASASC2-0714, RAE 2822 (Royal Aircraft Establishment airfoil), NACA 0012, and the XV-15 baseline NACA 64A223. The sectional c_l/c_d versus angle of attack and the drag polar for each candidate are shown in Fig. 11.1.



(a) c_l/c_d vs angle of attack.

(b) c_l vs c_d.

Figure 11.1: Aerodynamic comparison of candidate wing airfoil sections evaluated using CFD.

The NACA 64A223 baseline, at 23 % thickness, has the lowest peak c_l/c_d of approximately 60, which is lower than all thinner airfoils considered, confirming that transitioning to a thinner section for *Mercury*'s wing is beneficial. Among the 13 % thick candidates, NACA 64A413 achieved the highest peak c_l/c_d of approximately 109 at $\alpha \approx 6°$, along with the highest peak c_l of 1.40 at minimum c_d. While NASA SC2-0714 showed a competitive drag polar, it stalled more abruptly and produced a lower sustained c_l at higher drag values. NACA 64A413 was therefore selected as the baseline section for further optimization, also benefiting from its membership in the NACA 64 airfoil family consistent with the existing XV-15 blade sections.

The selected NACA 64A413 profile was then used as the starting geometry for a shape optimization study. A Genetic Algorithm was used to search the design space, with aerodynamic performance evaluations carried out by the AGRC airfoil surrogate in place of direct CFD calls, enabling a large number of candidate geometries to be assessed at low computational cost. The optimization objectives were to maximize c_l/c_d at the cruise operating angle of attack, widen the drag bucket to improve tolerance to off-design operating conditions, and maintain a pitching moment coefficient c_m close to that of the baseline NACA 64A413 to avoid significant changes to the wing structural loads. Manufacturability of the wing was also considered during the optimization. Airfoil sections with highly convex camber lines, sharp leading edges, and features that increase tooling complexity and fabrication cost were excluded. The geometric constraints applied to the optimizer parameters ensured that only smooth, practical airfoil shapes were generated throughout the design space. The resulting optimized section, designated AGRC-W413, achieved a peak c_l/c_d of 118 at $\alpha = 6°$, representing an improvement of approximately 8 % over the baseline, with a minimum c_d reduction of approximately 5 % and a noticeably wider drag bucket. The pitching moment remained within 3 % of the baseline values across the operating angle of attack range. The geometry and aerodynamic performance comparison between NACA 64A413 and AGRC-W413 are presented in Fig. 11.2.

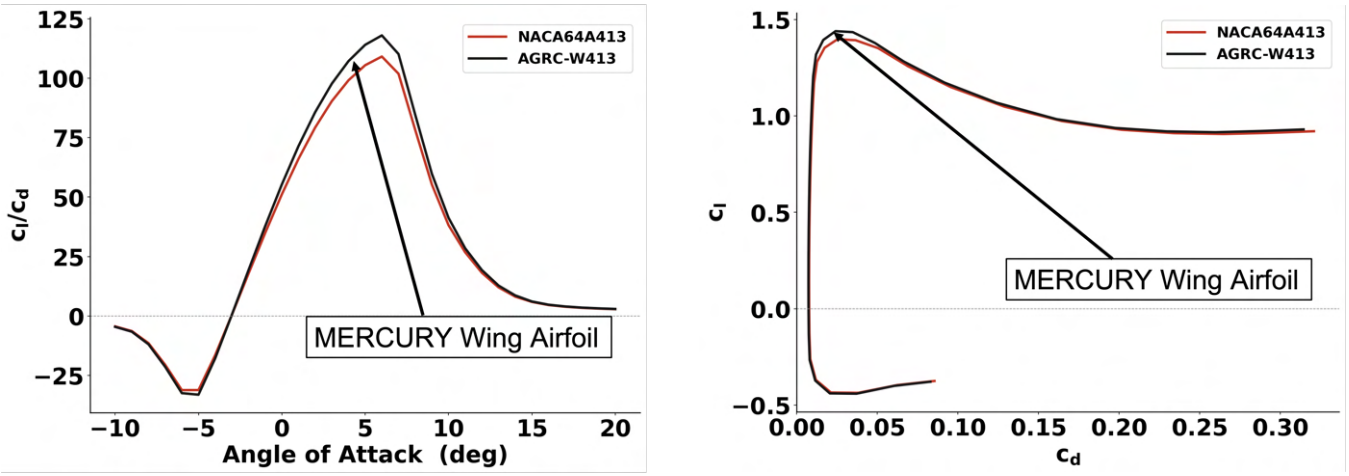
11.1.2 Wing Geometry

The *Hermes* wing retained all geometric parameters of the XV-15 baseline, as required by the RFP. For *Mercury*, comprehensive analysis showed that the proprotor blade flap amplitude was sufficiently small that the risk of blade-wing contact was eliminated, and the forward sweep was therefore removed. The dihedral was also set to zero to simplify the cross-wing transmission shaft arrangement and improve manufacturability. Roll stability for *Mercury* is instead provided by a dihedral angle incorporated into the horizontal stabilizer. The geometric parameters for both configurations are summarized in Table 11.1.

Table 11.1: Wing parameters for *Hermes* and *Mercury*.

Parameter	***Hermes/XV-15***	***Mercury***
Area	15.70 m^2 (169.0 ft^2)	15.70 m^2 (169.0 ft^2)
Span	9.80 m (32.17 ft)	9.80 m (32.17 ft)
Chord	1.60 m (5.25 ft)	1.60 m (5.25 ft)
Aspect ratio	6.12	6.12
Incidence	3.0°	3.0°
Dihedral	2.0°	0.0°
Sweep ($c/4$)	−6.5°	0.0°
Wing L/D	15	17.5
Airfoil section	NACA 64A223	AGRC-W413

The wing surface pressure coefficient c_p and streamlines from in-house Hamiltonian Path and Strand Grid



(a) c_l/c_d vs angle of attack.

(b) c_l vs c_d.

(c) Airfoil geometry: NACA 64A413 vs AGRC-W413.

Figure 11.2: Comparison of NACA 64A413 and AGRC-W413 wing airfoils.

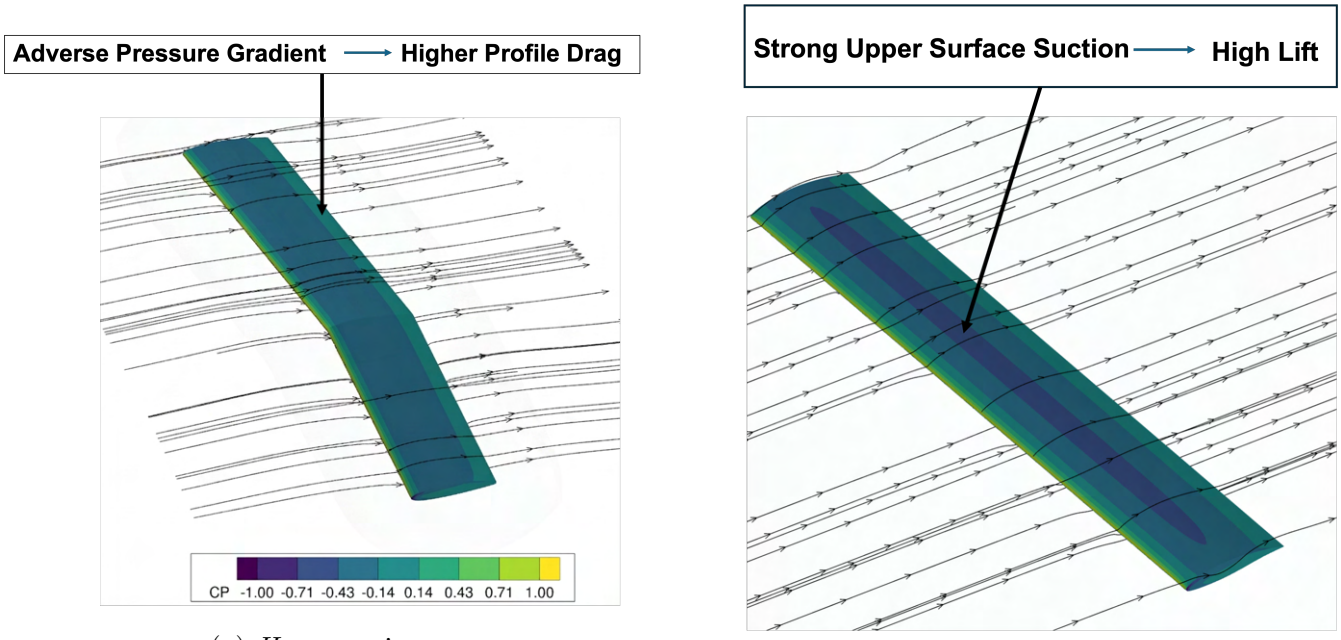
based CFD solver (HAMSTR) at cruise conditions are shown in Fig. 11.3. *Mercury* exhibits more uniform streamlines and smoother pressure recovery along the trailing edge compared to *Hermes*, indicating better flow attachment and lower profile drag in cruise.

11.2 Wing Structural Design

The *Mercury* wing is primarily comprised of a single continuous torque box spanning nacelle to nacelle. Unlike conventional fixed-wing aircraft, tiltrotor wings are sized to meet stiffness requirements rather than strength requirements. The torque box is designed to provide the necessary beamwise bending, chordwise bending, and torsional stiffness to delay the onset of whirl flutter beyond the limit airspeed of 180 m/s (350 kt), and to sustain 3.5g maneuver loads in airplane mode and 2g hover and transition loads. Figure 11.4 shows the torque box with ribs and enclosed fuel bladders, without the outer skin.

11.2.1 Torque Box Sizing and Stiffness

The torque box is comprised of front and rear vertical webs located at 13% and 50% of the chord, respectively, connected by upper and lower skins to form a closed thin-walled section. The front chordwise position was set to ensure adequate space for the 60 mm (2.36 in) diameter cross shaft, bearings, shaft dampers, and flex couplers. This closed section is essential for increasing torsional stiffness required to prevent whirl flutter. Four spar caps are placed at the web-skin junctions to increase beamwise bending



(a) *Hermes* wing.

(b) *Mercury* wing.

Figure 11.3: Wing surface c_p distribution and streamlines at cruise.

stiffness and reduce stress under high loading. A series of 3 additional stringers are placed along the top and bottom skin panels to prevent buckling and provide a small amount of additional bending stiffness.

Ribs are spaced spanwise to maintain the airfoil cross-sectional shape and to support the flaperon control surfaces and interconnecting shaft components. Spaces for the interconnecting driveshaft and electrical wiring to pass through are made in the ribs. The torque box also houses enclosed fuel bladders carrying all fuel required for the RFP mission profile.

Required wing stiffnesses were determined by scaling the frequencies of XV-15 [17]. Initial sizing was performed by modeling the torque box cross-section as a trapezoid to estimate area moments of inertia. Classical laminate plate theory (CLPT) was used to identify anisotropic properties of the composite for varied ply layups. A grid search over skin thickness and ply layups was conducted to minimize weight, with results shown in Fig. 11.5. Only combinations of spar skin thickness and ply layups that achieve within 5% of the target stiffness are visible. The final design achieves a beamwise bending stiffness $EI_{\mathrm{N}} = 6.53 \times 10^6$ N·m^2, a chordwise bending stiffness $EI_{\mathrm{C}} = 1.62 \times 10^7$ N·m^2, and a torsional stiffness $GJ = 4.41 \times 10^6$ N·m^2.

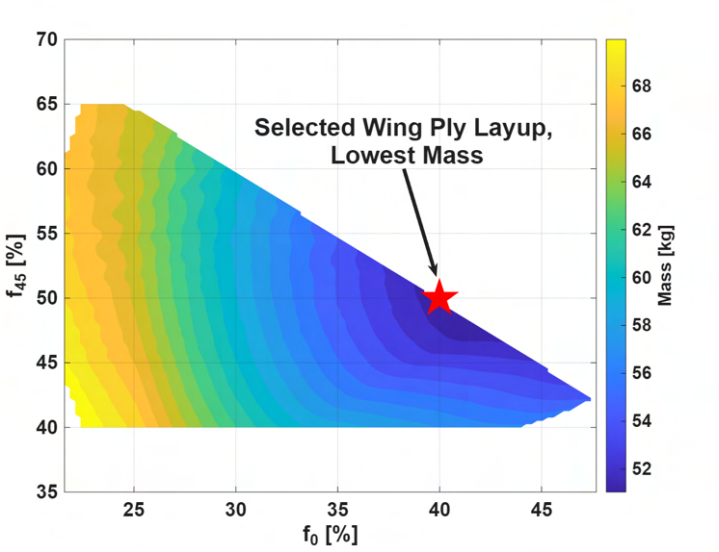


Figure 11.5: Grid search results for the wing torque box skin composite layup, showing half wing torque box weight of feasible designs that meet XV-15 stiffness targets.

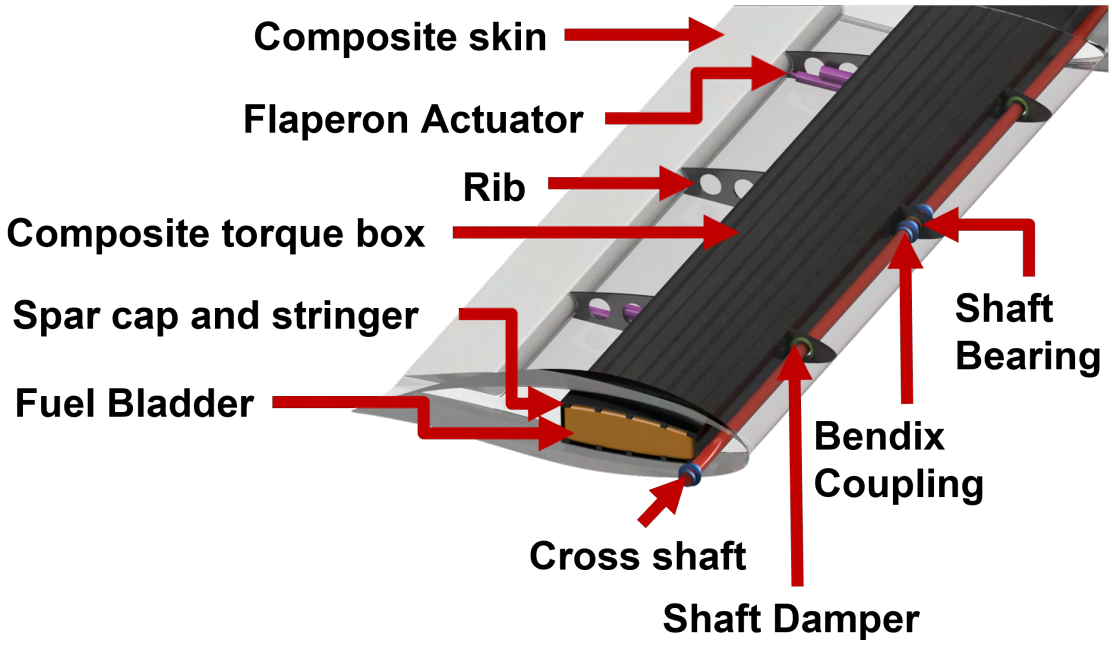


Figure 11.4: Grid search results for the wing torque box skin composite layup, showing half wing torque box weight of feasible designs that meet XV-15 stiffness targets.

11.2.2 Material Selection and Manufacturing

T300/5208 graphite-epoxy composite was selected for construction of the torque box, providing the high stiffness required to meet whirl flutter margins while providing a 31% reduction in weight versus aluminum. The torque box skin is a balanced and symmetric laminate with with 40% [0°] plies, 50% [±45°] plies, and 10% [90°] plies. The [±45°]-dominant layup maximizes torsional stiffness, while the [0°] plies provide spanwise stiffness to resist beamwise bending. The spar caps are 85% [0°] and 15% [±45°]. This layup strategy follows the design rules of thumb proposed by Kassapoglou [33] and protects against unforeseen secondary load cases.

The wing is constructed as a single continuous unit from nacelle to nacelle. Prefabricated molds hold the reinforced graphite fiber layers along with preformed spar cap assemblies. Mandrels within the mold shape the internal torque box geometry and are removed following cure. Because graphite-epoxy composite is a poor conductor of electricity, an aluminum mesh is co-cured into the outermost skin ply to prevent damage to the structure in the event of a lightning structure.

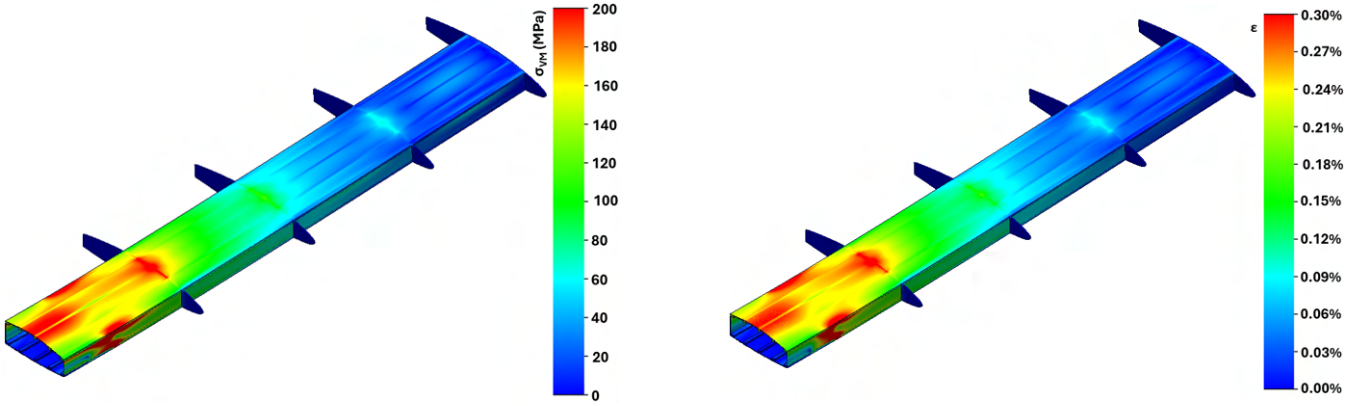
11.2.3 Finite Element Analysis

To verify the structural integrity of the *Mercury* wing design, FEA was performed using SolidWorks Simulation with unstructured tetrahedral elements. A curvature-based mesh was used, with the characteristic length set at 5 mm (0.2 in) to adequately capture stresses throughout the wing skin and ribs. This resulted in a high-quality mesh with the aspect ratio of all elements below 3. These mesh settings yielded approximately ten-million elements for the full-body model. Courser meshes were also run to identify any singularities present in the stress distributions.

The wing-fuselage connection was represented by a fixed boundary condition applied along a 50.8 mm (2 in) strip at a 762–812.8 mm (30–32 in) offset from the centerline on the bottom edges of the forward and aft spar faces. Two load cases were evaluated, driven by maneuverability requirements at 95% of the

mission gross takeoff weight, in accordance with the 2025 FAA Powered Lift and standard ATM flight maneuver requirements: 2g structural load factor in helicopter/conversion mode, and 3.5g structural load factor in airplane mode.

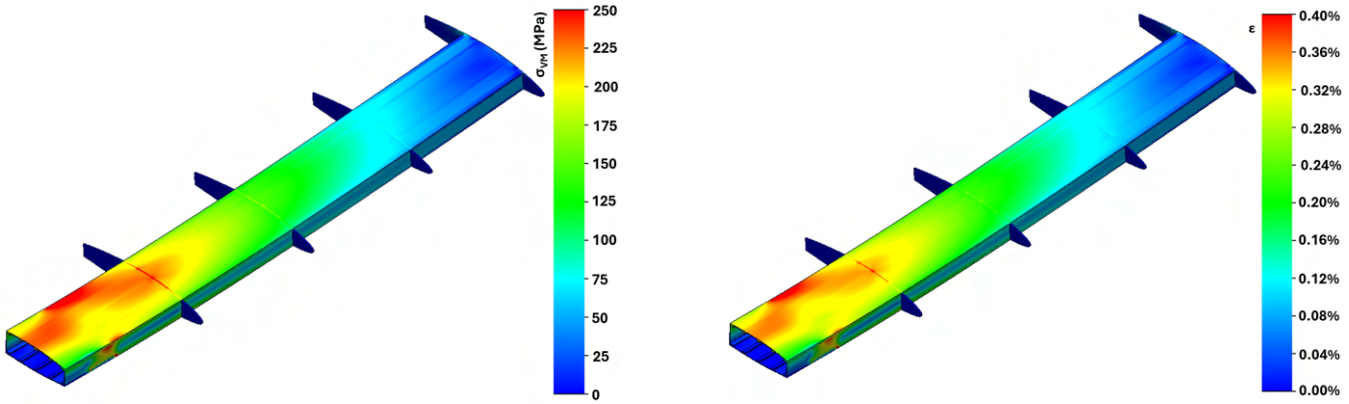
In the 2g case, representing hover and transition, the full 2g load is supported by rotor thrust, applied as a conservative 116 kN (26,000 lb) vertical load distributed evenly to the outboard ribs. In the 3.5g load case, *Mercury* is in aircraft mode so the full 3.5g load is supported by wing lift which was distributed evenly by applying 202 kN (45,500 lb) along the upper surface of the spar. In both cases, the loading and geometry is symmetric, so the model was cut in half with a symmetry boundary condition applied at the midplane.



(a) Stress distribution.

(b) Strain distribution

Figure 11.6: Wing FEA at 3.5g airplane mode loading condition.



(a) Stress distribution.

(b) Strain distribution

Figure 11.7: Wing FEA at 2g hover loading condition.

The 3.5g load case, shown in Fig. 11.6, produced peak von Mises stress of 250 MPa (36.2 ksi) and approximately 0.4% strain, with stress concentrations along the first upper skin panel and at the junction with the first inboard rib. The 2g load case, shown in Fig. 11.7, produced a peak stress of 200 MPa (29 ksi) and 0.3% strain, with hotspots at the upper corners of the forward and aft spar ends and near the first rib junction. These hotspot locations informed iterative design refinements, resulting in increased rib thickness and enlarged spar caps at critical stations. The final design achieves a safety factor greater than 1.5 in both load cases. In the hover load case the safety factor is approximately 2.5, and in the cruise case the safety factor is approximately 3.

11.3 Whirl Flutter Stability Analysis

Whirl flutter is the critical aeroelastic constraint for high-speed tiltrotors in airplane mode. *Mercury* is designed to be flutter free well beyond the vehicle limit airspeed of 180 m/s (350 kt). Two primary design levers are wing stiffness and pylon CG location relative to the wing elastic axis. Moving the pylon CG aft toward the elastic axis is stabilizing. In *Mercury*, the rotor-only tilt configuration allows the engine to be mounted aft on the pylon without ground clearance constraints.

Mercury features a 3-bladed gimbaled hub with scaled wing stiffnesses near those of the Maryland Tiltrotor Rig (MTR), a Froude-scaled wind tunnel model with wing stiffnesses itself loosely scaled to the XV-15. The *Mercury* wing elastic axis is located at 31% chord and the nacelle CG at 25% chord, placing the *Mercury* wing CG 6% of rotor radius (R) ahead of the elastic axis.

Whirl flutter stability was evaluated through both experiment and analysis, shown in Fig. 11.9. MTR wind tunnel stability tests were conducted in the Glenn L. Martin Wind Tunnel at the University of Maryland (Fig. 11.8), and confirm that a pylon CG 10% R ahead of the elastic axis, more destabilizing than *Mercury*'s 6% offset, remains stable up to 200 kt model-scale (460 kt full-scale equivalent) [34]. The test data is a representative case of the *Mercury* wing, as the wing frequencies are close (Table 11.2). UMARC-II, an in-house comprehensive multi-body aeromechanics solver [35], was used to model the *Mercury* rotor, wing, and pylon and predict stability across the same airspeed range. It remains a difficult challenge to predict whirl flutter accurately. However, both experiment and analysis confirm *Mercury* is whirl flutter free well beyond its limit airspeed, with a stability margin exceeding 29% above 180 m/s (350 kt).

Mode	XV-15	MTR	*Mercury*
1st Beam	0.45	0.29	0.27
1st Chord	0.86	0.54	0.58
1st Torsion	1.07	0.83	1.03

Table 11.2: Wing natural frequencies (/rev) at cruise RPM.

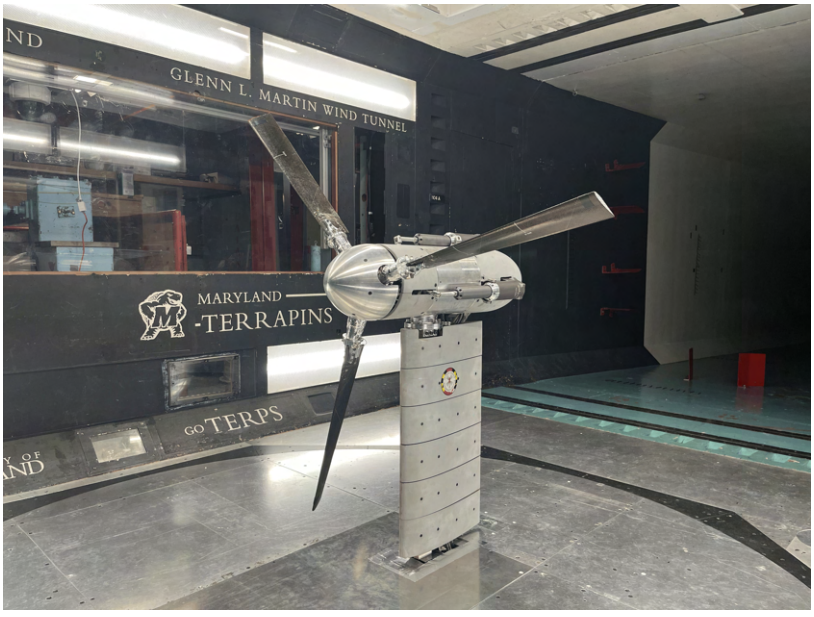
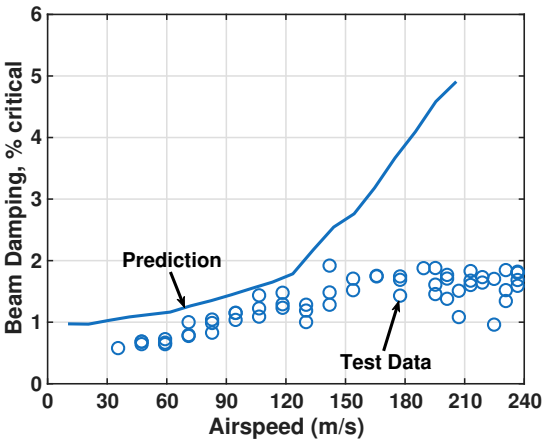
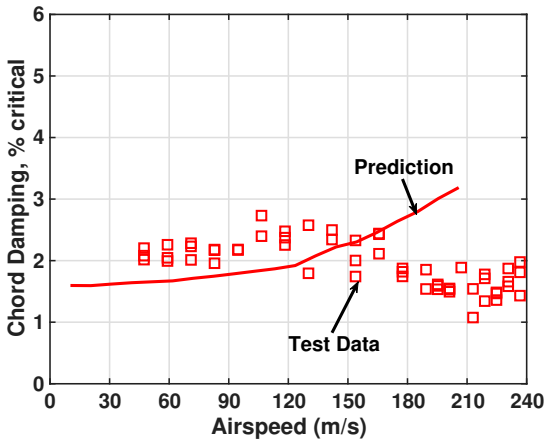


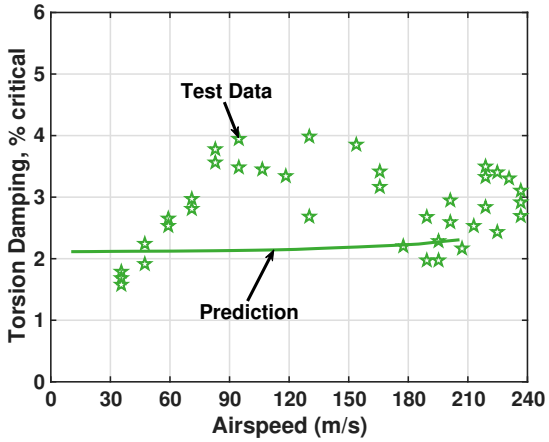
Figure 11.8: University of Maryland Tiltrotor Rig (MTR) in the Glenn L. Martin Wing Tunnel.



(a) Beam



(b) Chord



(c) Torsion

Figure 11.9: Mercury Whirl flutter stability analysis.

12 Mercury Airframe Design

In Phase I, the *Hermes* design retained the complete external geometry of the XV-15 baseline, including the rotor, wing, fuselage, nacelle, and empennage, as required by the RFP. For the Phase II vehicle, *Mercury*, the airframe was aerodynamically and structurally optimized beyond the hybrid system modifications of Phase I to improve performance in both airplane mode cruise and hover at 1,219 m / 35°C (4,000 ft / 95° or 4K/95), while respecting the RFP constraints.

12.1 Fuselage Design

12.1.1 Fuselage Aerodynamic Design

Drag reduction of the fuselage was a primary driver of airplane mode improvement of *Mercury* performance. The XV-15 fuselage geometry was reshaped using superellipse-based cross-sectional lofting, a parameterization in which key physical shape features such as nose fullness, leading and trailing edge roundness, and tail ramp steepness are directly derived from and controlled by the superellipse parameters. These shape parameters were used as design variables in a Genetic Algorithm based multi-objective optimization with the objective of minimizing fuselage aerodynamic drag. A machine learning-based surrogate model, AGRC

fuselage surrogate [36], was used to evaluate the aerodynamic performance of each candidate fuselage geometry in place of direct CFD, and a total of 24,000 surrogate evaluations were performed to arrive at the optimized fuselage shape.

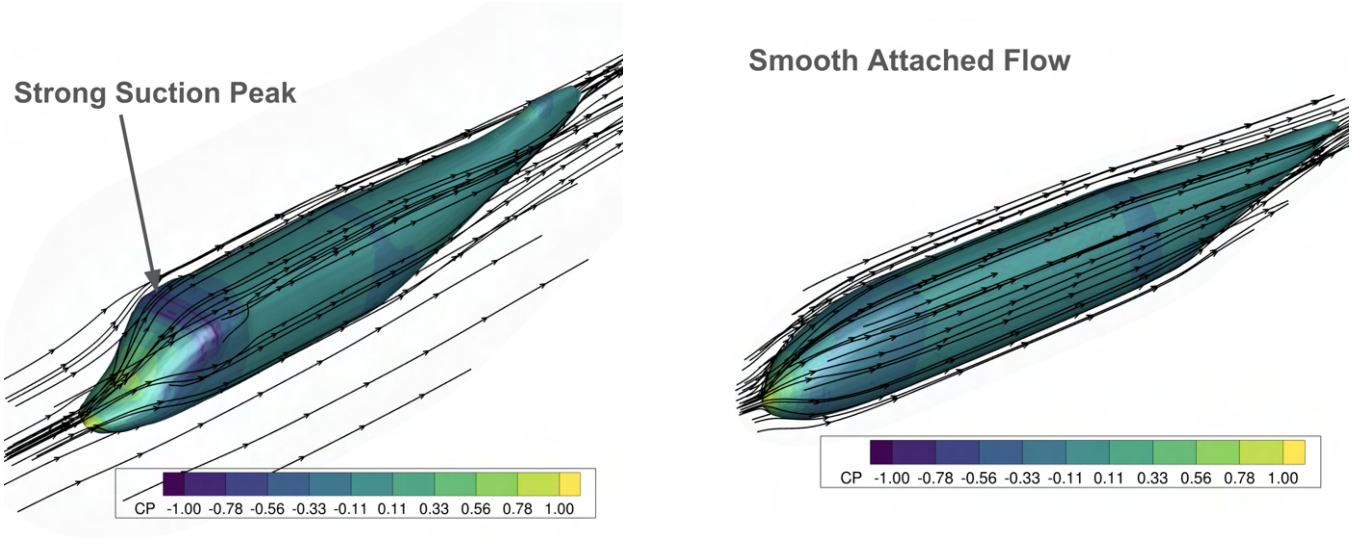
The UMD in-house Hamiltonian Path and Strand Grid based CFD solver (HAMSTR) [37] was used to assess the aerodynamic performance of the baseline and optimized fuselage. Optimization of the fuselage shape alone yielded a drag reduction of approximately 13 % relative to the XV-15 baseline. Further significant reduction was achieved by reconfiguring the cabin layout: adopting a tandem pilot arrangement and a staggered-row passenger seating arrangement allowed the fuselage width to be reduced by 30 %. The narrower and more elliptical cross-section also results in a smaller perimeter at each fuselage station, reducing the total wetted area compared to *Hermes*/XV-15, which directly lowers the skin friction drag component. The resulting frontal area cross-sectional comparison between *Hermes*/XV-15 and *Mercury* is shown in Fig. 12.1. Together, the optimized shape, reduced wetted area, and reduced cross-section resulted in a total fuselage drag reduction of 29% compared to *Hermes*/XV-15.



(a) Hermes/XV-15 frontal view

(b) Mercury frontal view

Figure 12.1: Frontal area cross-section comparison.



(a) *Hermes*: surface C_p with streamlines.

(b) *Mercury*: surface C_p with streamlines.

Figure 12.2: Fuselage surface C_p with streamlines at cruise conditions.

The fuselage surface C_p distributions and near body streamlines from CFD at cruise conditions are shown in Fig. 12.2. The *Hermes* fuselage shows a stronger suction peak near the nose with a more pronounced adverse pressure gradient along the mid-body, contributing to higher pressure drag. In contrast, *Mercury* shows a smoother and more gradual pressure recovery with fully attached streamlines along the entire body length, reflecting the more streamlined and aerodynamically efficient geometry achieved through the fuselage shape optimization.

12.1.2 Fuselage Structural Design

Mercury's fuselage is a semi-monocoque structure consisting of thirteen aluminum bulkheads connected by a T800/M21 carbon fiber/epoxy skin-stringer shell. The skin panels carry the primary torsional and shear loads, while the bulkheads react concentrated loads from the wing, empennage, landing gear, and internal systems. A single keel beam runs along the bottom of the fuselage to react vertical bending. A second keel beam is not required given the narrow fuselage cross-section.

The skin-stringer construction follows the approach used in the Airbus A350, in which curved fuselage panel sections are manufactured separately with co-cured longitudinal stringers, then joined at bulkhead stations during final assembly [38]. In *Mercury*, each panel section is produced by laying the carbon fiber skin and integral stringers together on a mandrel using automated fiber placement (AFP). This ensures precise fiber orientation and minimizes labor-intensive hand layup. Lightning strike protection is provided by an expanded copper foil mesh co-cured with the outermost ply of the carbon fiber skin. The aluminum bulkheads are then inserted and mechanically fastened to the barrel sections at each frame station. This construction was chosen over a fully co-cured fuselage (including bulkheads) to allow for individual panels and bulkheads to be repaired. Aluminum is selected for the bulkheads for its machinability to the multiple bulkhead shapes and low cost of production. However, direct contact between aluminum and carbon fiber composite can lead to galvanic corrosion of the aluminum. To mitigate this risk, several protective measures are employed. The aluminum bulkhead faces are anodized and a fiberglass fabric layer is interleaved between each bulkhead and the carbon fiber skin to provide electrical isolation. In addition, all fasteners are wet-installed with polysulfide sealant to seal holes against moisture ingress.

Two central bulkheads, thicker than the remaining eleven, serve as the primary wing attachment frames. The wing is mounted to these bulkheads using a four-pin connection, adapted from the ATR 42/72 wing-fuselage joint [39]. This arrangement allows the wing and fuselage to be manufactured and inspected independently, then joined during final assembly. The remaining eleven bulkheads distribute loads from the empennage structure and landing gear, and provide attachment points for the cooling system, battery pack, electric drivetrain components, and the flight deck. The internal structure is shown in Figure 12.3.

12.1.3 Finite Element Analysis

A simplified model of the *Mercury* fuselage was simulated with FEA using SolidWorks Simulation to ensure the structure can handle the large maneuver loads required by the RFP. A curvature-based mesh was used, with the characteristic length set at 6.35 mm (0.25 in) to adequately capture stresses across the thickness of the frames, bulkheads, and stringers. These mesh settings yielded approximately fourteen-million elements for the full-body model.

The wing-fuselage connection was represented by a fixed boundary condition applied at the cut surface of the two bulkheads and symmetry was applied in the lateral direction. The portion of the fuselage which carries the most load and has the most uniform cross section was simulated. This fuselage model was constructed by an ellipsoidal shell element representing the skin which runs from the second frame forward of the wing connection to the second frame aft of the wing connection. The ellipsoid shape was based

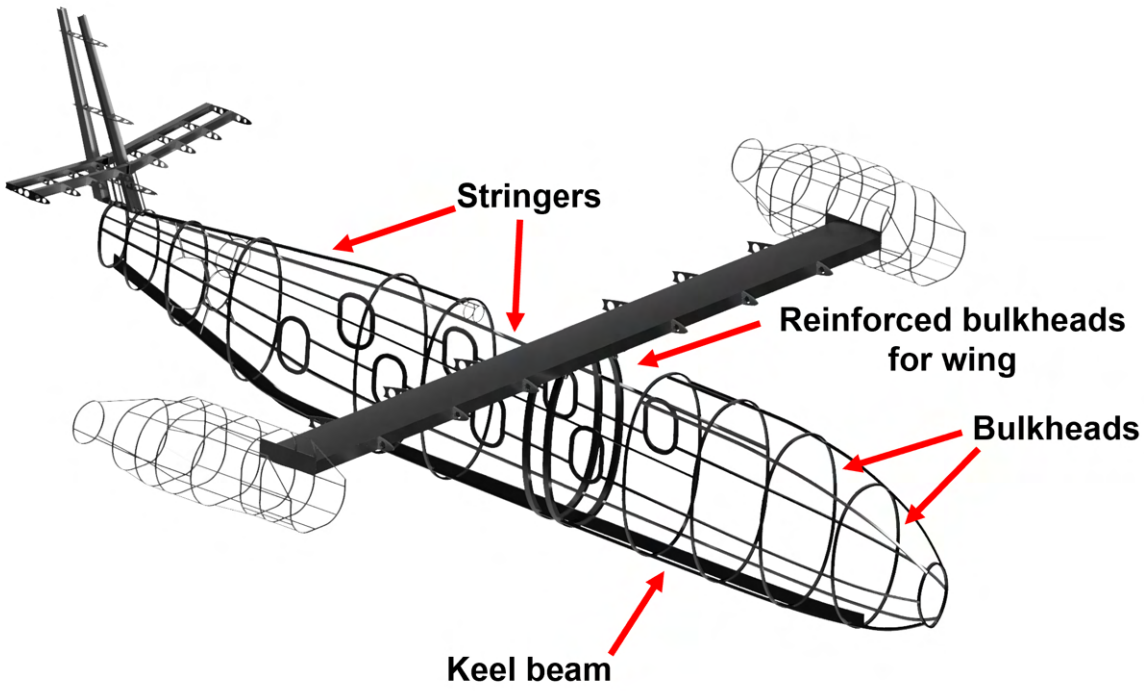


Figure 12.3: *Mercury* Internal structure.

on the maximum fuselage dimensions. The skin was connected to frames and stringers spaced according to the detailed model, with the bottom stringer replaced by a larger keel beam. The top three stringers between the inner two frames were cut along with the skin to leave room for the wing.

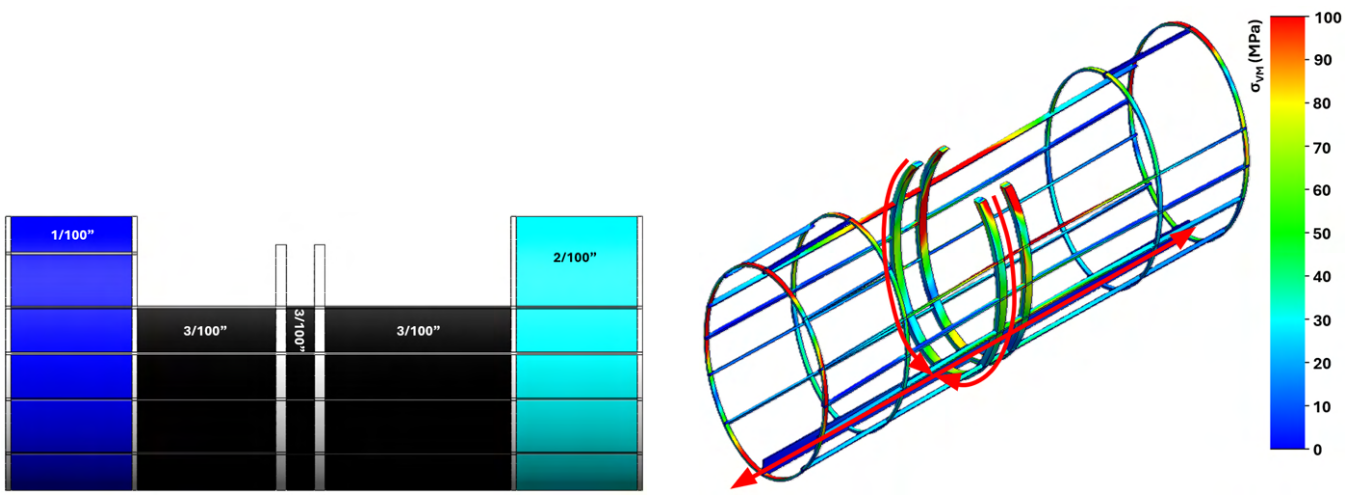
The 3.5g maneuver load case was simulated by distributing a 202 kN (45,500 lb) vertical load evenly to the four frames mounting the wing. The skin was split into five panels. A baseline skin thickness of 0.3 mm (0.01 in) was applied to each panel and the FEA model was iterated to target a 300 MPa (29 ksi) stress with Safety Factor of 1.5 by adjusting panel thicknesses in increments of 0.3 mm (0.01 in) as shown in Fig. 12.4(a). After each iteration, root-mean-squared von-Mises stresses in each segment of each panel were recorded, with segment boundaries defined by stringer locations. This was done to eliminate the effect of singularities on the iteration process. Typical von-Mises stresses in the stringers, frames, and bulkheads are 100 MPa (14.5 ksi). Figure 12.4(b) shows the *Mercury* fuselage FEA and the load path in the internal structure under 3.5g loading condition.

12.2 Nacelle Design

In addition to the fuselage, the nacelle geometry was also addressed as a contributor to overall parasite drag in airplane mode. The aerodynamic and structural considerations for the nacelle design are presented in subsections 12.2.1 and 12.2.2, respectively.

12.2.1 Nacelle Aerodynamic Design

For *Mercury*, the reduction in power required for both hover and cruise, resulting from the overall vehicle weight and drag reduction achieved in other components, allowed the engines to be scaled down. A V-280 Valor inspired architecture was adopted in which only the rotor and proprotor gearbox rotate during conversion, with the engine remaining fixed within a slimmer nacelle fairing. The surface pressure coefficient

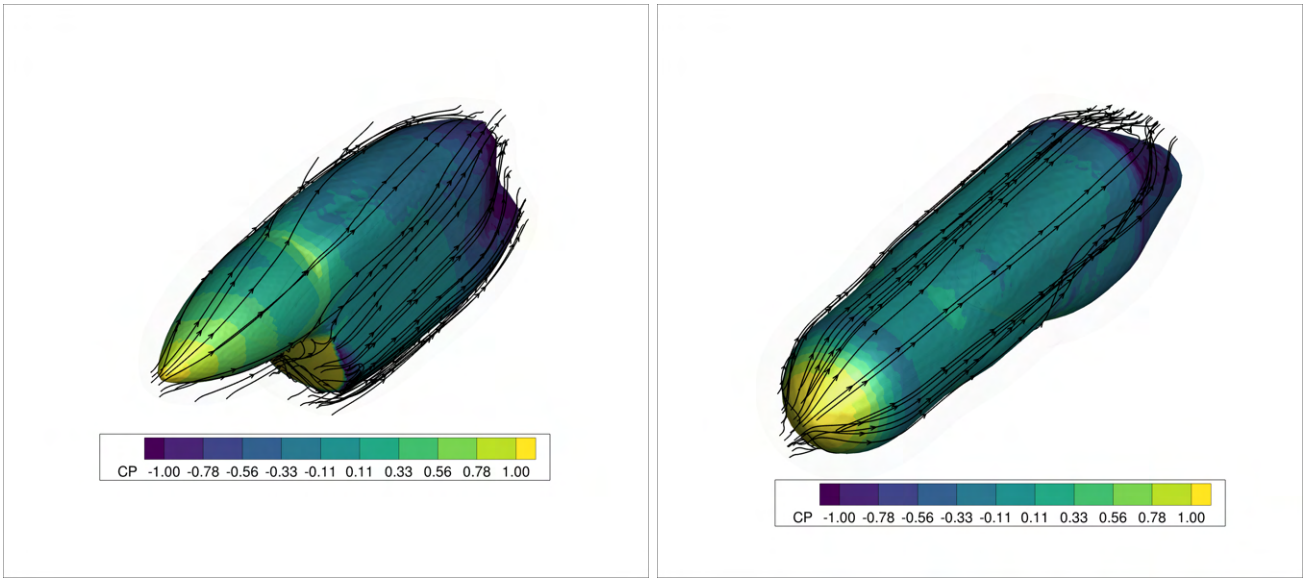


(a) Final fuselage skin thicknesses.

(b) Fuselage FEA load path under 3.5g loading.

Figure 12.4: *Mercury* fuselage finite element model.

distributions with nearbody streamlines from CFD for both nacelle configurations at cruise conditions are shown in Fig. 12.5. The *Hermes* nacelle shows stronger pressure gradients and more disturbed streamlines around the aft body, consistent with the bluffer geometry of the fully-rotating XV-15 nacelle. The *Mercury* nacelle, designed with a more elongated and streamlined design, shows smoother streamline attachment along the body and a more gradual pressure recovery, contributing to the lower parasite drag. The resulting nacelle flat-plate drag area is reduced from $0.0635\,\mathrm{m}^2$ (*Hermes*) to $0.0475\,\mathrm{m}^2$ (*Mercury*), representing a 25% reduction in nacelle parasite drag per side.



(a) *Hermes* Nacelle.

(b) *Mercury* Nacelle.

Figure 12.5: : Surface c_p with streamlines from CFD for nacelles in airplane mode.

12.2.2 Nacelle Structural Design

The nacelle assembly in helicopter mode is shown in Fig. 12.6. The nacelle structure follows a semi-monocoque construction similar to the fuselage consisting of a series of bulkheads and stringers, although careful consideration was required to accommodate the tilting mechanism. Tilting the entire nacelle to the vertical orientation is not possible due to limited ground clearance. Therefore, only the rotor and the rotating gearbox housing directly below it tilt upward during helicopter mode. Lift rods transfer rotor aerodynamic loads from the swashplate to the planetary gearbox housing. The planetary gearbox housing is directly connected to the bevel gearbox housing which consists of a non-rotating component attached to the nacelle structure, and a rotating component that revolves about the cross-shaft tilting the rotor upward. The nacelle structure is mounted to the wing spar. This series of connections ensures the rotor loads are transferred into the wing and fuselage structure.

To convert between helicopter and airplane modes, a singular double ball screw actuator powered by duplex self contained electro-hydraulic motors pushes against the planetary gearbox housing, tilting the rotor as depicted from hover (Fig. 12.6) to cruise (Fig. 12.7). Two electro-hydraulic motors are used for redundancy. The actuators permit tilting angles from 0° to 95°, with the additional five degrees of tilt backwards in helicopter mode improving the autorotation capability of *Mercury*.

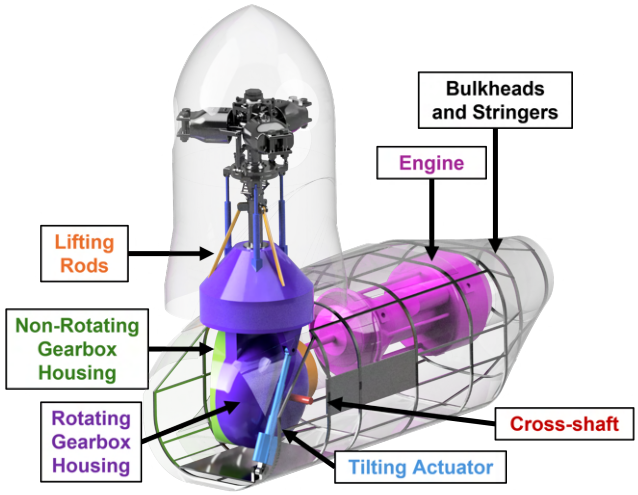


Figure 12.6: Nacelle in helicopter mode.

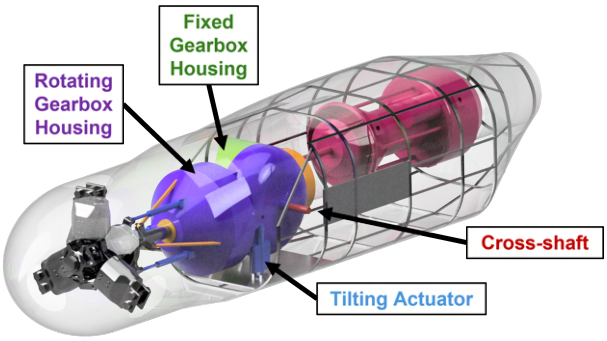


Figure 12.7: Nacelle in airplane mode.

12.3 Landing Gear

Like the XV-15, *Mercury* uses the tricycle configuration for landing gear. *Mercury* has two wheels for the nose landing gear and uses only one wheel for each side of the main landing gear. This landing gear configuration allows *Mercury* to store the main landing gear inside the fuselage removing the need for sponsons and improving aerodynamic efficiency. The front gear retracts forward and upward toward the nose of the aircraft. Should there be a hydraulic failure the landing gear can be unlocked and use gravity to aid in deployment.

12.3.1 Tire Selection

The selection of tires for the aircraft was primarily influenced by the requirement to manage landing loads while maintaining a compact profile. Four tire types were evaluated during the design phase: Type III,

Type VII, Three Part Type, and Radial. Detailed comparisons of these tire options are documented in Table 12.1 Ultimately, the Type III 5-4 tire was selected for the nose gear, and the Type III 7-8 was chosen for the main gear. These Type III models were favored because they are able to meet the load requirement while having a small overall dimension. The discrepancy in size between the nose and main gear tires reflects the 15:85 load distribution between the front and rear landing gear systems.

Table 12.1: Tire Parameter. **Chosen tire.*

Location	Tire Type	Size	Diameter (in)	Aspect Ratio	Tire Pressure (psi)
Front	Type III*	5–4	13.25	0.92	55
	Type VII	16×4.4	16.00	0.90	55
	Three Part	15×6.0-6	15.20	0.73	68
	Radial	16×4.4R8	16.40	0.90	155
Rear	Type III*	7–8	20.90	0.88	125
	Type VII	24×7.7	24.15	0.92	110
	Three Part	24×7.25-12	24.5	0.84	120
	Radial	21×7.25R10	21.90	0.78	166

12.3.2 Landing Gear Position

Lateral positioning of the landing gear is dictated by the center of gravity height, ensuring the assembly meets the minimum tip-over threshold of 25 degrees. This placement also accounts for a 1.5-foot fuselage clearance and expected tire displacement during static loading. Longitudinally, the configuration maintains a 15:85 load distribution between the nose and main gear relative to the longitudinal center of gravity. Consequently, the main landing gear and nose landing gear is placed at 60% and 10% of the fuselage length.

12.4 Crashworthiness

Mercury incorporates a layered crashworthiness strategy addressing structural energy absorption, occupant protection, and fuel system integrity.

Airframe: A keel beam runs longitudinally along the underside of the fuselage, providing a continuous load path that resists vertical crash loads and prevents floor collapse from encroaching on the occupant cabin.

Fuel System: Fuel is stored in multiple independent crash worthy bladders distributed across the wing rather than a wet wing, resulting in only 5% loss in fuel capacity for much improved fire post crash fire safety. Self-sealing bladders resist rupture and reduce fuel spillage following a crash, limiting fuel release and the risk of post-crash fire. Frangible couplers on all fuel lines at the engine interfaces sever cleanly under crash loads, isolating the bladders from the engines and preventing sustained fuel flow to a potential ignition source.

Occupant Protection: Pilot seats are equipped with Variable-Load Energy Absorbers (VLEAs), which stroke under controlled load to attenuate the vertical impulse transmitted to occupants, maintaining deceleration within survivable limits across a range of impact severities.

Propulsion Safety: In an engine failure during nacelle conversion from airplane to helicopter mode, rotor RPM must be maintained to prevent underspeed during the critical transition. The electric motor

can sustain rotor speed in both single and all-engine-out conditions, allowing the crew time to execute a controlled autorotative or powered landing.

13 Mercury Empennage

13.1 Empennage Configuration

The XV-15 H-tail configuration carries considerable structural weight, motivating a different empennage design for *Mercury*. A conventional tail was ruled out. The top surface of the fuselage angles down aft of the wing, so a conventional horizontal stabilizer would sit in the direct wake of the wing, lowering elevator effectiveness. A T-tail was rejected due to the added structural weight penalty of carrying the horizontal stabilizer atop the vertical fin. A cruciform configuration and V-tail were analyzed for cruise stability using an in-house flight dynamics code with the resulting stability roots shown in Fig. 13.1. A cruciform tail resulted in increased static stability versus a 45°V-tail of equal area, while also having lower structural weight. The *Mercury* horizontal stabilizer is placed at 25% span of the vertical tail, clear of both the fuselage and wing wake. *Mercury* is not anticipated to decelerate to wing stall in airplane mode, therefore impingement of a stalled wing wake on the tail was not a sizing consideration.

The horizontal stabilizer has a span of 3.18 m (10.42 ft) and a chord of 0.91 m (3.00 ft), with 5° of dihedral to enhance static stability in airplane mode. The horizontal stabilizer has a setting angle of $-2°$ to maintain cruise trim. The vertical stabilizer has a span of 1.90 m (6.25 ft). Empennage sizing was performed using aircraft tail volume ratios from [40] for representative fixed wing aircraft as a function of wing area and fuselage length. Both surfaces use a symmetric NACA0012 airfoil, appropriate for a control surface operating across positive and negative angles of attack. The horizontal stabilizer primarily counteracts the nose-down pitching moment from the wing and the forward pitching moment of the rotors in forward flight, a consequence of the vehicle center of gravity (CG) located ahead of the wing aerodynamic center for static stability and rotor shaft pivot point. The vertical stabilizer provides yaw control in forward flight.

13.2 Empennage Structure

The horizontal and vertical tail surfaces share a common structural concept: two aluminum I-beam spars with aluminum ribs and a composite skin. The two-spar arrangement carries bending and torsion loads, while the ribs maintain the airfoil section and distribute concentrated loads into the skin. The T800/M21 carbon epoxy composite skin provides additional torsional stiffness and reduces weight relative to an aluminum alternative. Aluminum 7075 is selected for the internal structure due to its machinability, ease of repair, and compatibility with the modest aerodynamic loads on the empennage surfaces.

The cruciform tail configuration places the horizontal stabilizer at 25% of the vertical tail span. Rather than transferring horizontal tail loads through the vertical tail structure, the horizontal stabilizer is independently supported by mounts connecting to the top stringer of the fuselage. This decouples the two surfaces structurally and allows each to be sized independently for its own loads. It also simplifies repair and replacement of either surface independently. The structural arrangement is shown in Fig. 13.2.

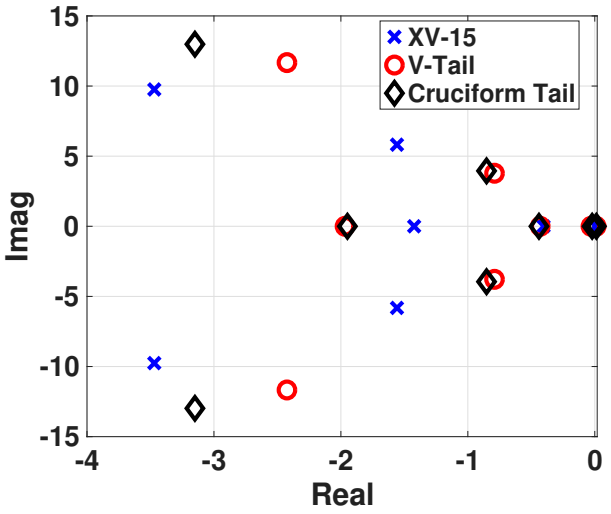


Figure 13.1: Cruise stability roots for *Mercury* with a V-tail and cruciform tail design compared to the XV-15

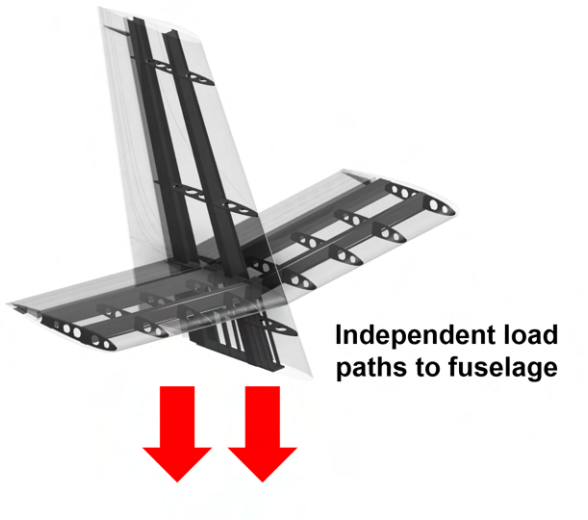


Figure 13.2: *Mercury* vertical and horizontal stabilizers have independent load paths to the fuselage structure.

14 Mercury Flight Controls and Avionics

14.1 Fly-by-Wire Architecture

Mercury employs fly-by-wire flight controls in place of the XV-15's mechanical mixing linkages, which are particularly heavy due to the complex collective, cyclic, and conversion control mixing throughout the vehicle's flight envelope. Replacing this hardware with a triplexed flight control computer (FCC) saves 82 kg (180 lb) [41] and reduces volume, while enabling additional automation that reduces pilot workload throughout the mission.

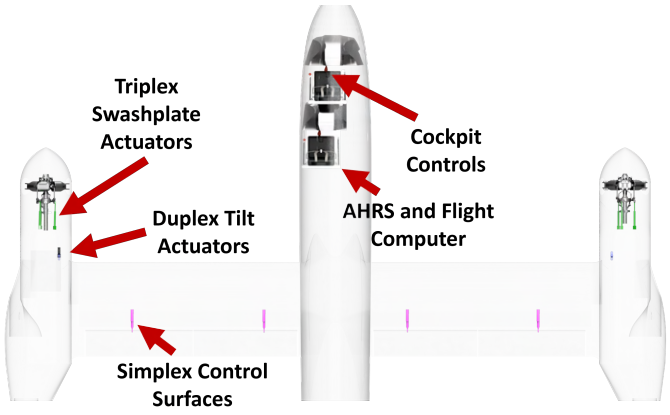


Figure 14.1: Flight controls diagram.

As shown in Fig. 14.1, fourteen electro-hydraulic actuators are distributed throughout the aircraft. Each rotor has three triplexed actuators controlling the swashplate. Nacelle conversion is managed by duplex hydraulic motors, and the fixed-wing control surfaces, flaperons, elevator, and rudder, are driven by simplex actuators. Redundancy is sized to consequence of failure: swashplate actuators are triplexed because loss of hover control is catastrophic, conversion actuators are duplexed as the aircraft must be able to control nacelle tilt, and fixed-wing surface failures still permit a safe transition to hover and landing.

14.1.1 Cockpit Controls

Each pilot has an independent lateral and longitudinal stick, yaw pedals, and throttle. A thumb-operated dial on each throttle controls nacelle conversion angle. A hybrid enable switch on the center console engages the automatic hybrid cycling strategy, and a rotor speed setting switch commands the change between hover and cruise. Beyond this, all power splitting, engine governing, and battery management is handled automatically by the FADEC and HMC without further pilot input. All controls feature a force feedback system providing tactile cues on aircraft state, and the conversion dial provides haptic feedback to keep the pilot within the conversion corridor.

14.1.2 Full Authority Digital Engine Controllers and Hybrid Management Computer

Mercury retains the same dual-channel FADEC and HMC architecture developed for the Phase I hybrid design *Hermes*, described in Section 5. The FADEC governs fuel flow, TIT, and turbine shaft speed on each turboshaft. The HMC coordinates the turboshaft-motor power split and hybrid power strategy. The rotor speed reduction from 589 RPM in hover to 343 RPM in cruise is made following the pilot command, after crossing the airspeed threshold, and nacelle conversion.

14.2 Avionics

14.2.1 Cockpit Layout

Mercury utilizes a tandem cockpit layout and a 1 by 6 single-row passenger layout as shown in Fig. 14.2 and Fig. 14.3. The tandem cockpit in conjunction with single-row seating reduces fuselage width by 30% and fuselage drag by a corresponding 29% compared to the XV-15 and *Hermes*. The captain sits at the front while the copilot sits 0.25 m (10 in) higher and 0.12 m (4.6 in) to the left. The copilot seat maintains a field of view of 140° compliant with FAA AC 25.773-1 [42]. The seating arrangement is offset to the left, allowing both pilots access to their seats. Each pilot station is equipped with independent glass displays, throttles, sticks, and pedals as shown in Fig. 14.2.

14.2.2 Avionics Architecture

Mercury is built on a foundation of proven, certified off-the-shelf avionics based on Garmin technology to minimize development risk. The Garmin G3X integrated flight deck provides a primary flight display (PFD), multifunction display (MFD), and an integrated avionics computer. The interface has been adapted from the standard Garmin configuration to support *Mercury*'s fly-by-wire architecture and hybrid propulsion system, with dedicated displays and control logic added for tiltrotor-specific functions including conversion corridor guidance, nacelle position feedback, and hybrid energy management.



Figure 14.2: *Mercury* cockpit and cabin top view.



Figure 14.3: Copilot cockpit view.

14.2.3 Hybrid Monitoring System

The Hybrid Monitoring System (HMS) is a custom display integrated into the MFD providing the crew with a real-time status of the propulsion system related parameters (Fig. 14.4). Engine power and temperature for both turboshafts, motor torque and temperature, and battery SOC are presented in a unified view. In an additional display, a power flow synoptic analogous to the energy management display of the Toyota Prius [43] depicts instantaneous power transfer between the turboshafts, motor/generator, battery, and rotors, enabling rapid assessment of hybrid system operation. Battery SOC is rendered as a live bar with digital readout, and the hybrid power split ratio (the fraction of total propulsive power supplied electrically) is prominently displayed to support in-flight energy management decisions.

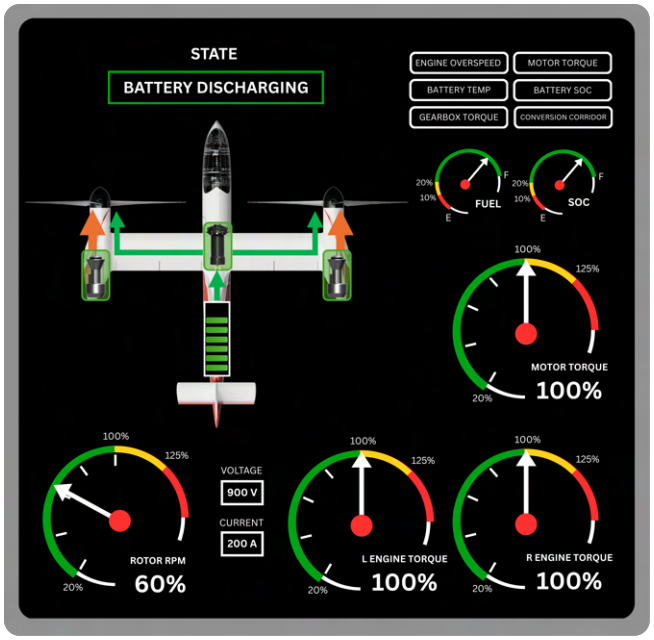


Figure 14.4: *Mercury* hybrid monitoring system.

A First Limitation Indicator (FLI) is integrated into the HMS, consolidating limit monitoring across all aircraft systems into the pilot's primary scan. Parameters monitored include engine overspeed, motor torque, battery temperature and SOC minimum, gearbox torque limits, and conversion corridor boundaries. When a parameter approaches its limit, the FLI annunciates the affected system with color-coded urgency (caution/warning) and directs the crew to the appropriate corrective action.

14.2.4 Autopilot

Mercury employs a full autopilot suite comprising a Stability Augmentation System (SAS) and a Flight Director (FD) in both airplane and helicopter mode, built on the Garmin GFC autopilot platform and adapted for tiltrotor fly-by-wire integration. The system provides 4-axis attitude stabilization through all primary flight phases, with the FD delivering guidance cues for route following, altitude capture, and airspeed management, enabling single-pilot operation.

14.2.5 Communications and Power

Mercury carries HF, UHF, and VHF radios for communication with other aircraft and ATC, an intercom connecting the flight deck with the passenger cabin, a cockpit voice recorder, and ADS-B Out in compliance with Federal Aviation Regulations. Avionics power is drawn from the main 900 V DC bus and stepped down to 28 V through a dedicated DC-DC converter, with a secondary 14 V bus powering displays, radios, and flight computers. A self-contained avionics battery within the AHRS enclosure provides up to 30 minutes of backup power to essential instruments in the event of a main bus failure.

14.2.6 Health and Usage Monitoring System

Mercury employs a Health and Usage Monitoring System (HUMS) to maintain airworthiness and support condition-based maintenance. Strain gauges and accelerometers distributed across the rotor hubs, nacelle gearboxes, cross shaft, wing, and fuselage monitor vibration signatures and structural loads. Temperature and pressure sensors cover the battery pack, electric motor, and turboshaft engines. During flight the HUMS monitors outputs against established limits and alerts the crew upon exceedance; post-flight, accumulated load cycle and fatigue data are available for download by maintenance crews. The flowchart is shown in Figure 14.5.

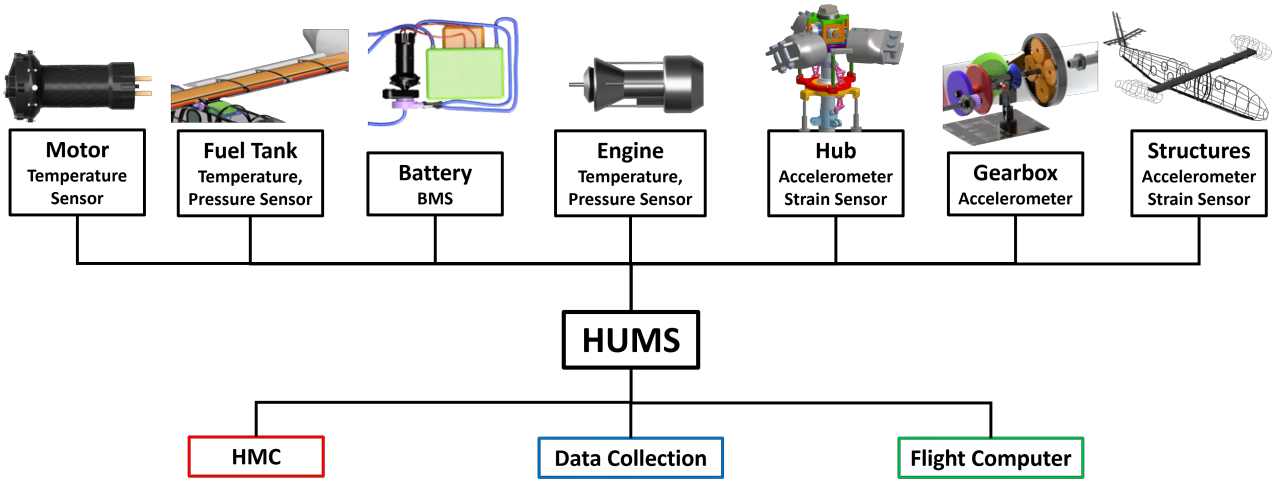


Figure 14.5: Health and usage monitoring system flowchart.

15 Mercury Flight Dynamics

15.1 Control Mixing

Pilot controls for a tiltrotor must intuitively merge the controls of a conventional helicopter with an airplane. Pilot inputs are fed into the triplexed flight control computer (FCC) for mixing and stability augmentation, with sensing from an attitude and heading reference system (AHRS). A summary of the control mixing strategy is outlined in Table. 15.1.

Table 15.1: Control Mixing Strategy

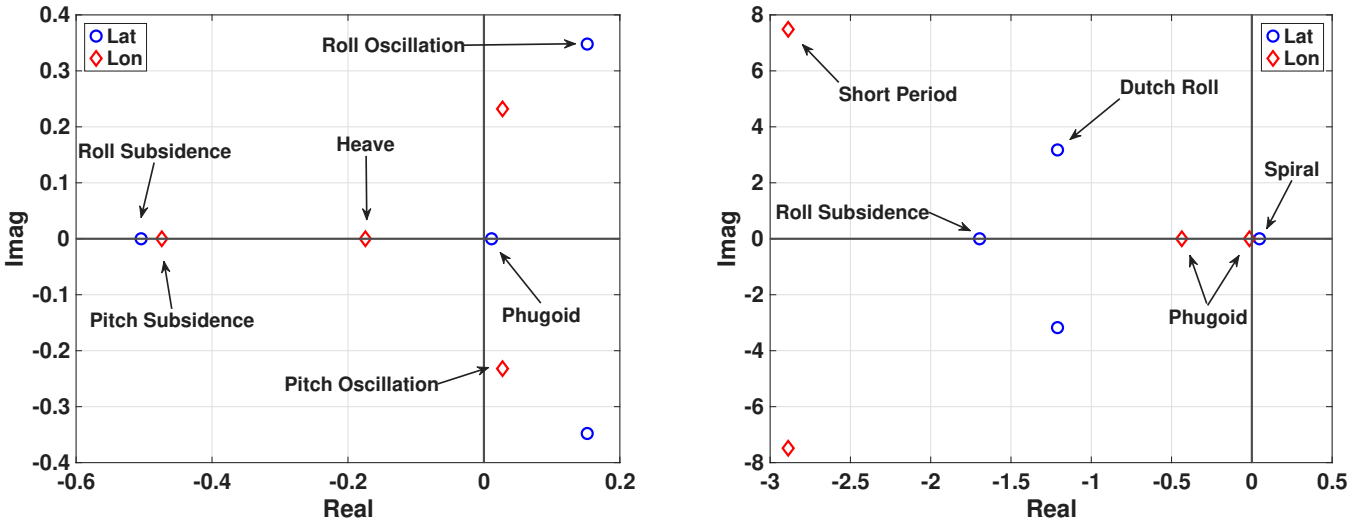
Control Input	**δLat**	**δLon**	**δThrottle**	**δPed**
Rotor	Lat. Cyclic and Diff. Collective	Lon. Cyclic	Collective Pitch	Diff. Lon. Cyclic
Control Surfaces	Flaperons	Elevator		Rudder

In hover, the throttle lever simultaneously modulates the collective pitch on both rotors to increase and decrease lift. Longitudinal control inputs command the longitudinal cyclic on both rotors equally. This induces a pitching moment on the aircraft, but unlike a conventional helicopter, tilting the rotor shafts is preferred to generate forward thrust. The lateral control inputs manage the lateral cyclic on each rotor as well as a differential collective. Differential rotor thrust augments the lateral cyclic to produce a rolling moment on the aircraft. Pedal controls produce a differential longitudinal cyclic where the rotor tip path planes are in opposite directions generating a yawing moment. The flaperons are directed down in hover to minimize wing download. In forward flight, the rotors tilt forward as speed increases. Conventional airplane controls progressively replace the helicopter controls as the control surfaces become more effective. Rotor controls only remain to adjust the rotor pitch and thrust in forward flight.

15.2 Aircraft Stability

Mercury's flight dynamics model utilizes a 6-degree-of-freedom rigid-body dynamic model of the fuselage, nonlinear aerodynamic lookup tables for the fuselage, rotor blades, wing, and empennage, rigid flap and lead-lag rotor blade dynamics, and a dynamic inflow model for the rotor. The state vector contains the rigid body states, position states, blade flapping and lagging states, and dynamic inflow states for the proprotors. The control inputs consist of collective, lateral and longitudinal cyclics, and pedals. The nonlinear model is linearized by trimming the vehicle to a desired flight condition.

In hover, *Mercury* exhibits hover behavior expected from tiltrotors as shown by the decoupled stability roots in Fig. 15.1(a). *Mercury* has an unstable Dutch roll mode and phugoid mode in hover. Cruising at the mission flight speed of 156 m/s (303 kt), *Mercury* has a slightly unstable spiral mode as shown in Fig. 15.1(b). To manage these instabilities, pilot control is aided by the stability augmentation system (SAS).



(a) Hover (b) Cruise

Figure 15.1: *Mercury* open loop stability roots in hover and airplane cruise.

16 Mercury Vehicle Performance

16.1 Vehicle Drag Estimation

Component-level parasite drag was estimated for *Mercury* in airplane mode at 156 m/s (260 KCAS) and 3048 m (10,000 ft) using a combination of high-fidelity CFD and Prouty's semi-empirical method [44]. The primary aerodynamic components fuselage, main wing, and nacelles were analyzed using the in-house Hamiltonian Strand Navier Stokes CFD solver (HAMSTR), providing the equivalent flat-plate drag area f for each component, defined as:

$$D = \frac{1}{2}\rho V^2 f \tag{5}$$

where f is the equivalent flat-plate drag area (m^2) representing the area of a flat plate oriented normal to the flow that would produce the same drag.

The remaining components, the horizontal and vertical tail, were estimated using Prouty's method. Interference drag between each lifting surface and the fuselage was accounted for using an interference factor of 10% applied to each component consistent with Prouty's estimates. Miscellaneous drag, which includes contributions from antennas, door handles, skin gaps, and rivets was also estimated following Prouty's method. It should be noted that the wing flat-plate area obtained from HAMSTR CFD reflects the total drag at the cruise setting angle, and therefore includes both the profile drag and the induced drag contribution at the operating lift coefficient. The resulting component drag breakdown for *Mercury* is presented in Table 16.1. *Mercury* achieved a total drag reduction of approximately 28 % relative to the *Hermes/XV-15*, driven primarily by the redesigned fuselage shape (29.0 % reduction), the thinner, unswept AGRC-W413 wing section (25.0 % reduction), the more streamlined and compact nacelle geometry (25.0 % reduction), and the cruciform empennage with reduced area replacing the H-tail (38 % and 66 % reduction in horizontal and vertical surface drag respectively).

Table 16.1: Component wise flat-plate drag area breakdown for *Hermes* and *Mercury* in airplane mode

Component	**Method**	***Hermes***		***Mercury***		**Δ (%)**
		f (m^2)	(ft^2)	f (m^2)	(ft^2)	
Fuselage	CFD	0.160	1.720	0.113	1.221	−29
Main Wing	CFD	0.332	3.570	0.249	2.677	−25
Interference	Prouty (10%)	0.033	0.357	0.025	0.268	−24
Nacelles (×2)	CFD	0.127	1.370	0.095	1.028	−25
Sponsons	Prouty	0.007	0.079	—		−100
Interference	Prouty (10%)	0.001	0.008	—		−100
Horizontal Tail	Prouty	0.039	0.420	0.024	0.259	−38
Interference	Prouty (10%)	0.004	0.040	0.002	0.025	−50
Vertical Tail(s)	Prouty	0.035	0.372	0.012	0.129	−66
Interference	Prouty (10%)	0.003	0.037	0.001	0.013	−67
Miscellaneous	Prouty	0.036	0.391	0.035	0.371	−3
Total		**0.777**	**8.364**	**0.556**	**5.985**	**−28**

16.2 Hover Download

Tiltrotors have higher hover download compared to conventional helicopters, owing to their higher disk loading and the large wing area positioned directly in the rotor downwash field. Based on XV-15 hover test data, the rotor wake download penalty ranges from 5–15 % of gross takeoff weight (GTOW) [45], depending on flap deflection angle and rotor–wing geometry. In hover, the wing operates at no forward speed and the rotor downwash impinges nearly perpendicularly on the wing upper surface, acting as a cross-flow bluff body rather than an aerodynamic lifting surface. The vertical drag coefficient and equivalent flat plate drag area for each component are reported in 16.2. Methods based on Prouty [44] and Hoerner [46] were used to estimate the vertical drag coefficients. The wing, horizontal tail, and vertical tail were approximated as 3D flat plates, while the nacelles, are approximated at cylinders. According to Anderson [47], drag coefficients of bluff bodies were measured using the frontal area as the reference area.

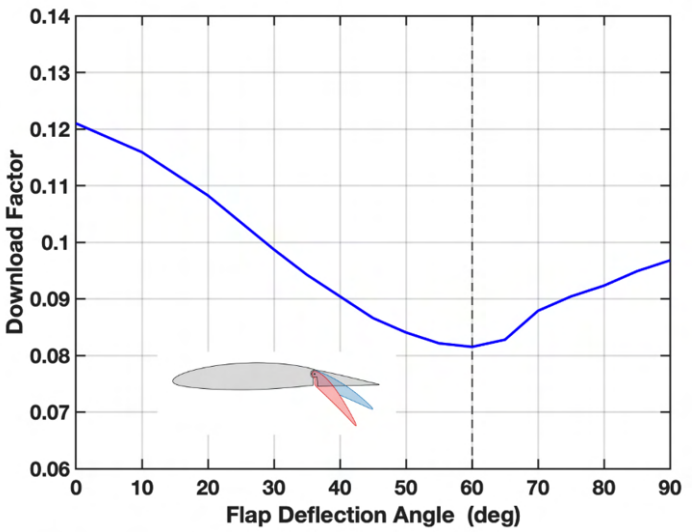


Figure 16.1: Hover download factor variation with wing flap deflection.

To reduce download, trailing-edge flaps are deflected in hover to redirect the rotor wake downward, reducing the effective area of the wing exposed to downwash. Rotor wake effects, such as induced velocity and rotor wake area, on the wing, are found using momentum theory along with a wake model.

Based on vertical drag coefficients from XV-15 hover tests [48], the optimal flap conditions can be found to minimize download as the percentage of thrust is reported for various locations and deflection angles

of the trailing edge flap. Download factor variation with flap deflection for the *Mercury* wing is shown in Fig. 16.1. With no flap deflection, a download factor of 0.12 is observed. The download factor decreases with increasing flap deflection, reaching a minimum of 0.08 at 60°, beyond which it begins to rise again. This increase occurs because at large flap angles the rotor downwash impinging on the wing separates from the surface, creating a recirculation region that increases the net downward force on the wing. For the *Mercury* wing, with a flap spanning 25% of the wing chord, a download factor of 0.08 is achieved by deflecting the flap 60° downward.

Table 16.2: Vertical drag breakdown for *Mercury* in hover at 4K/95.

Component	$f_{\mathbf{dl}}$ m^2 (ft^2)	**Contribution** (%)
Wing	17.637 (189.84)	86.0
Nacelles (×2)	1.907 (20.53)	9.3
Miscellaneous (5%)	0.964 (10.38)	4.7
Total f_{dl}	**20.51 (220.75)**	**100.0**

16.3 Hover Performance

The hovering performance of *Mercury* is shown in Fig. 16.2. The hybrid system provides a significant increase in available power because the battery can operate at maximum power output regardless of altitude. The performance of *Mercury* is limited under ISA +20° conditions, and the battery is required to hover out of ground effect under 1,219 m /35°C (4,000 ft / 95°F), conditions. *Mercury* is not designed to hover at altitudes above 1,219 m (4,000 ft) under ISA+20° conditions without exceeding the maximum rated power (MRP) of the engines. The torque limits are not shown as they are the same as *Hermes*. Given that the required power is substantially lower for *Mercury*, the torque limit is never reached in normal operation of the aircraft.

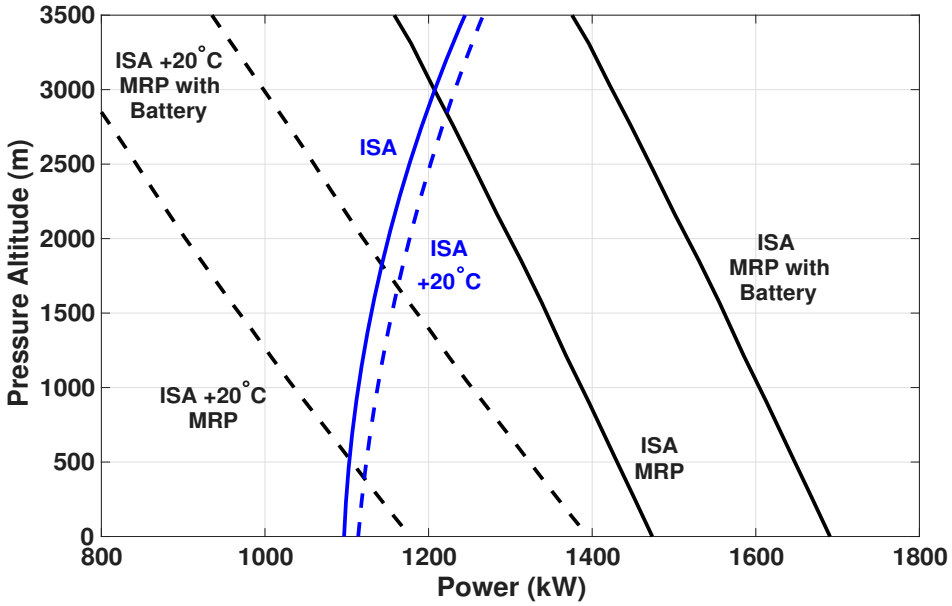


Figure 16.2: *Mercury* hover power required and maximum rated power (MRP) available from the engines under ISA and ISA+20 conditions at different pressure altitudes.

16.4 Conversion Corridor

The conversion corridor is calculated for *Mercury* with a wing flap angle of zero degrees as shown in Fig. 16.3. *Mercury* can be flown in helicopter mode, edgewise flight, up to a maximum speed of 68 m/s (132 kt) before requiring a transition into axial flight. Past this maximum speed, the rotor will encounter high advancing blade loads from transonic flow. The conversion sequence initiates immediately following a transition from hover to edgewise flight, but the nacelle angle is recommended to remain above 75°, largely remaining in edgewise flight, until the airspeed exceeds 46 m/s (89 kt) to avoid wing stall. *Mercury* maintains a rotor speed of 589 RPM the entirety of the conversion sequence to avoid rotor stall. The rotor RPM is only reduced to 343 RPM when the nacelles have rotated to 0°. The upper airspeed limit for nacelle angles between 60° and 0° is restricted by the power available from the engines and battery. Deflecting the wing flaps reduces the wing stall region enabling slightly slower speeds while tilting the nacelles.

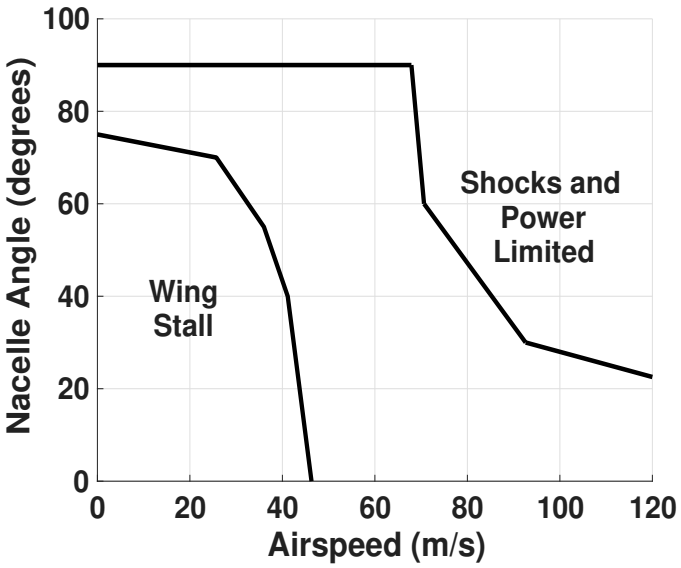


Figure 16.3: Conversion corridor for *Mercury* with $\theta_{flap} = 0°$.

16.5 Cruise Performance

The estimated power required at sea level for *Mercury* at different nacelle and flap angles is shown in Fig. 16.4. Drag estimates detailed in Section 16.1 were utilized to determine cruising performance. Due to the overall drag reduction of 28%, *Mercury* operates at significantly lower power compared to the XV-15. Increasing the nacelle angle (tilting it downward) enables progressively higher speeds. Deflecting the wing flaps (increasing θ_{flap}) is desirable in helicopter and conversion modes to offload lift onto the wings. In airplane mode, the wing generates all of the lift, so wing flap is not necessary and only contributes additional drag. *Mercury* operates at a relatively high speed of 77 m/s (150 kt) for best range, and a substantially lower speed of 46 m/s (89 kt) for best endurance. The L/D of *Mercury* at sea level is shown in Fig. 16.5. Airplane mode increases L/D considerably from helicopter and conversion modes, peaking to an L/D of 10.1 at 77 m/s (150 kt).

The range of *Mercury* is shown in Fig. 16.6(a). The RFP mission traverses a minimum of 567 km (306 nm) with two pilots totaling 181 kg (400 lb) and six passengers amounting to 544 kg (1,200 lb). Operating with the mission fuel capacity of 615 kg (1,355 lb), two pilots, and a six passenger payload achieves a range of 1,063 km (574 nm). The range with the onboard fuel tank can be extended to as much as 1,228 km (663 nm) if the payload is reduced to zero. Adding auxiliary fuel tanks maximizes the range to 1,895 km (1,023 nm) if *Mercury* carries no payload.

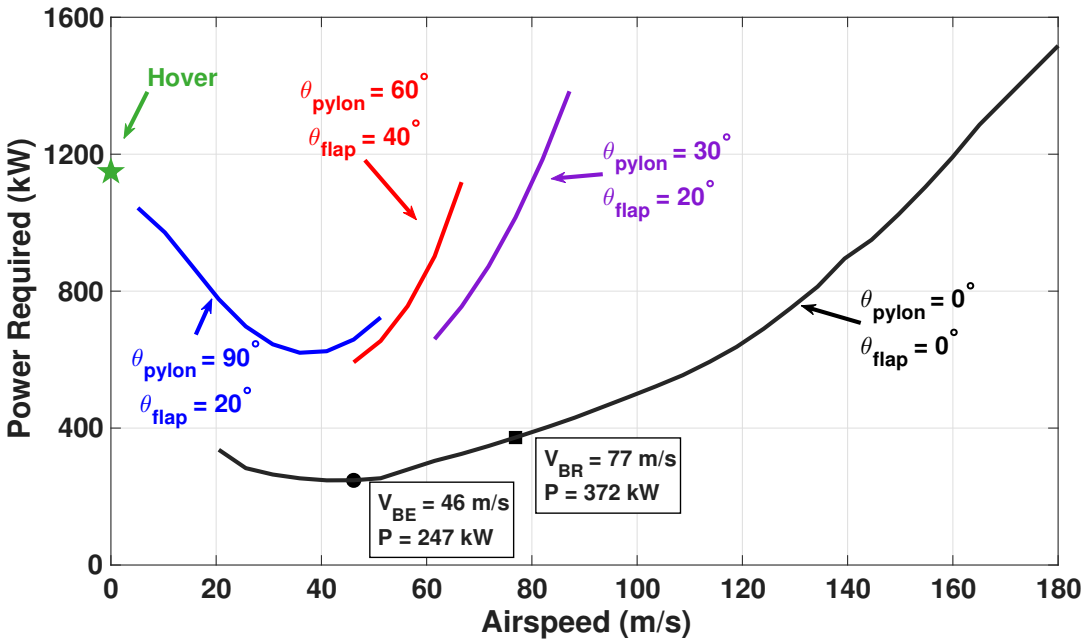


Figure 16.4: Power required at sea level for *Mercury* in helicopter, conversion, and airplane modes with best endurance and best range velocities in airplane mode.

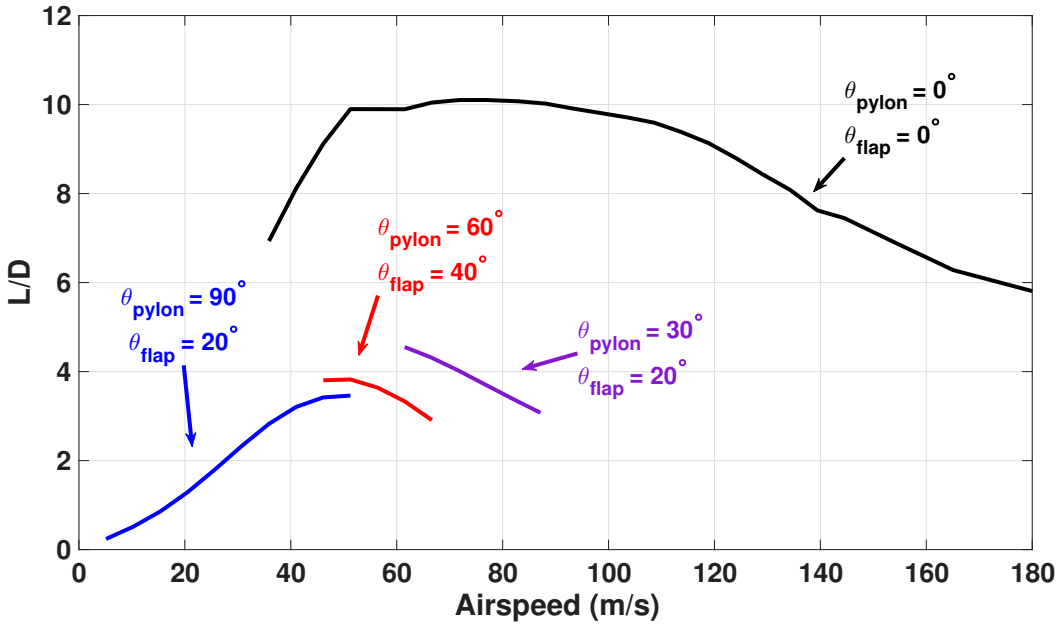
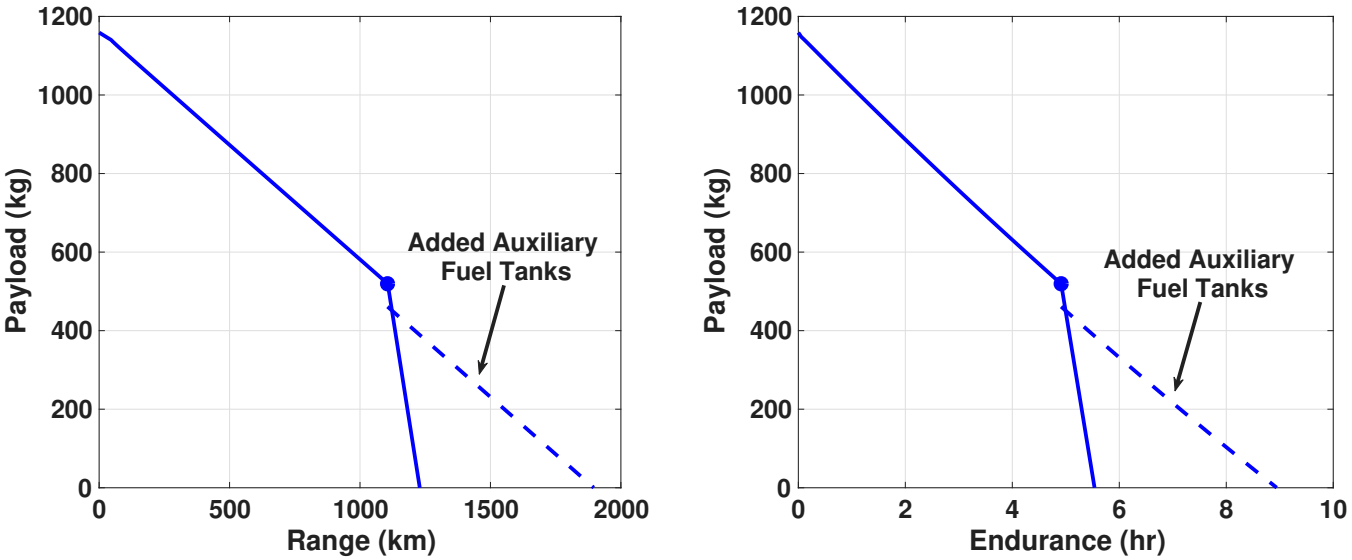


Figure 16.5: L/D at sea level for *Mercury* in helicopter, conversion, and airplane modes.

The endurance of *Mercury* is shown in Fig. 16.6(b). Carrying 544 kg (1,200 lb) of payload, two pilots, and the mission fuel capacity, *Mercury* can operate for 4.7 hours. Reducing the payload to zero while only using the onboard fuel tanks extends the endurance to as high as 5.5 hours. Supplying auxiliary tanks and removing the payload expands the endurance to a maximum of 8.9 hours.



(a) Range.

(b) Endurance.

Figure 16.6: Range and endurance of *Mercury* with two pilots.

The height-velocity envelope for *Mercury* is shown in Fig. 16.7. *Mercury* is capable of cruising at very high altitudes, but only for very short periods of time due to the limited energy capacity of the battery. Resorting to only engine usage reduces the envelope to lower altitudes and speeds. The maximum operating cruise speed is 168 m/s (327 kt) which can only be maintained for 6.3 minutes before the battery is fully depleted.

16.6 Climb Performance

The rate of climb for *Mercury* in airplane mode is shown in Fig. 16.8. The required power to climb is low at slow cruising speeds, enabling single engine operation to minimize fuel consumption. The climb rate can reach as high as 16.1 m/s (3,165 ft/min) when maximizing power from the engines and the battery. For the RFP mission, the battery is not discharged to climb faster or reduce fuel use because the hover segment prior expended the battery. Instead, both engines are utilized to climb and recharge the battery. *Mercury* completes the climb segment of the mission in 5.5 minutes at a climb rate of 9.2 m/s (1,818 ft/min) at a cruising speed of 64 m/s (125 kt) to avoid wing stall.

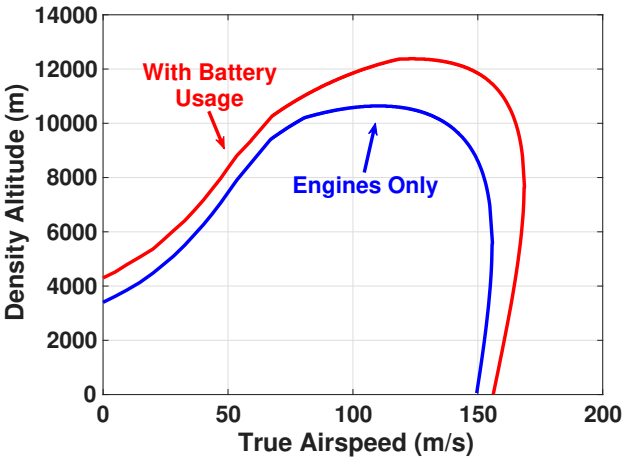


Figure 16.7: Height-velocity envelope for *Mercury* in airplane mode.

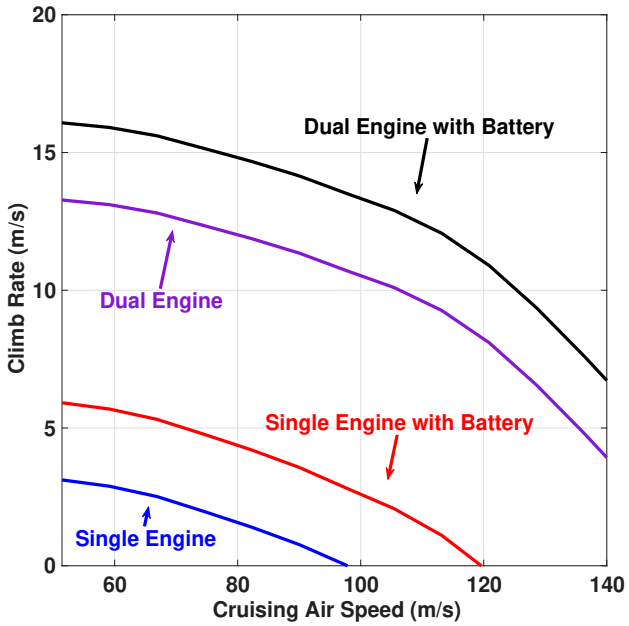


Figure 16.8: Climb rate of *Mercury* at sea level with various combinations of battery and engine usage.

17 Aircraft Operations and Sustainment

17.1 Technological Risk Assessment

Hermes and *Mercury* reduce development risk in two ways: integrating proven mechanical design elements and conducting extensive qualification testing. The integration of a hybrid architecture introduces technological risks through increased system complexity. However, this risk is offset by selecting proven, mature technologies in the remainder of the design. The airframe, rotor hub, transmission, and flight controls draw on existing tiltrotor designs, the XV-15, V22, and AW609, and are revised with modern materials for improvement. Battery and electric motor technology, although novel in tiltrotors, have been utilized in a wide variety of aircraft. During the development of the XV-15, extensive qualification testing on its transmission was conducted to resolve numerous concerns [18]. A testing apparatus was constructed that simulated the engine and proprotor flight loads, and a range of torques and RPMs were applied to the transmissions and gearboxes. Similar testing will be completed for *Hermes* and *Mercury* to establish confidence in the hybrid-electric designs across different flight test conditions and emergency scenarios.

17.2 Sustainment Impacts

The hybrid propulsion system in *Hermes* and *Mercury* introduces additional sustainment considerations to improve long-term reliability and service. Maintenance of electrical components is performed less frequently than on mechanical components due to containing significantly fewer moving parts. An on-condition maintenance strategy is used on the battery and motor where inspections only occur when the battery management system (BMS) indicates the components have substantially degraded or experienced damage. Active health monitoring predominantly tracks motor current and torque and battery current. Additionally, transient loads and sudden torque changes can be responded to much faster from a motor than the engines. Utilizing the motor in this manner reduces the amount of time the turboshaft engines operate at excessively

high speeds, and thus decreases wear and fatigue. This reduces overall maintenance time.

17.3 Emergency Procedures

Mercury is designed to operate safely under all single engine inoperative (OEI) and all-engine inoperative (AEI) conditions across the full flight envelope as required by the RFP. This safety of the propulsion and drive system is achieved through three complementary mechanisms: an interconnecting cross shaft, hybrid electric motor, and a dedicated autorotation capability.

17.3.1 One Engine Inoperative

Each turboshaft engine is coupled to its nacelle gearbox through a freewheeling sprag clutch. In the event of an engine failure or intentional shutdown, the sprag clutch disengages the failed engine from the drivetrain. The cross shaft then transmits the mechanical output of the operative engine across the wing to both rotors simultaneously. This architecture mirrors the interconnect-shaft philosophy of the XV-15, V-22, and AW-609.

Mercury's HPDM-180 center electric motor, rated at 180 kW (241 HP), provides a power reserve that is available instantly if an engine fault is detected. This arrangement is similar to the Airbus Engine Backup System, in which an electric motor on the main gearbox supplements or substitutes rotor drive power following an engine failure. The motor augmentation is particularly consequential at the critical points of a CS-29 Category A takeoff and landing profile. At the takeoff decision point, contingency (two minute setting) power available from the surviving engine plus electric motor output provides enough power to hover out of ground effect. This enables the pilot to accelerate and subsequently climb without altitude loss. At the landing decision point, the same combined power budget supports a balk and fly-away maneuver or a controlled OEI landing. The recommended power ratio criterion of $P_{\text{OEI}}/P_{\text{HOGE}} \geq 0.9$ for CS-29 Category A ground-level-helipad performance [49] is met by the combination of a single engine 2-min contingency rating and the electric motor's continuous output. *Mercury* was sized to achieve OEI power margins consistent with Category A performance at the critical points of the flight profile, with the electric motor ensuring that a single-engine failure remains a recoverable condition.

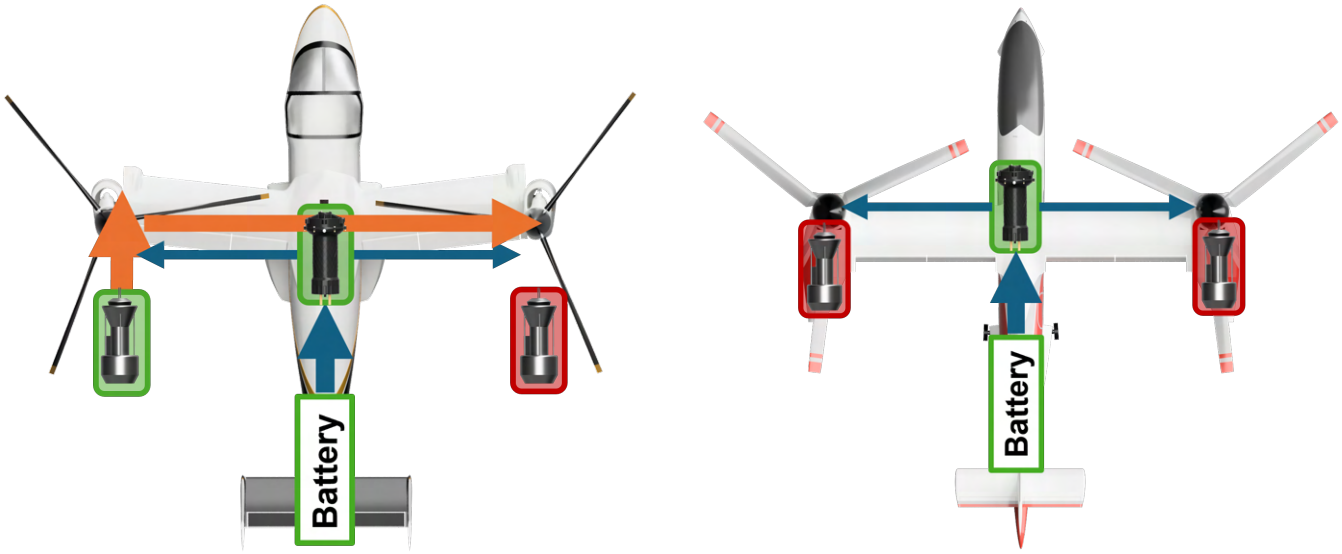
17.3.2 All Engine Inoperative Autorotation

The primary challenge for a tiltrotor aircraft during an AEI event in cruise is management of the rotor speed as the nacelles start in airplane mode (0° tilt) with the rotor disk oriented for forward thrust rather than lift. *Mercury* addresses this challenge and RFP requirement by utilizing the central electric motor to maintain rotor speed during nacelle conversion.

1. **Motor engagement and proprotor unloading:** AEI is detected through a combination of cross-shaft torque sensing and rotor speed decay. A reduction in cross-shaft torque indicates that the engines have stopped producing power, and rotor underspeed provides a confirmation independent of engine instrumentation. Upon detection, sprag clutch freewheels isolate the failed engines from the drivetrain, and the fly-by-wire system unloads the proprotors into a freewheeling state to reduce torque demand. The electric motor engages immediately to maintain rotor speed above the autorotative entry threshold.
2. **Nacelle conversion:** Once commanded by the pilots, the fly-by-wire system initiates an emergency nacelle tilt to helicopter mode (90°). At cruise airspeed, the wing provides sufficient lift to sustain a controlled glide, allowing the conversion to proceed without immediate altitude loss. Throughout the transition, the electric motor maintains rotor speed above the autorotative entry threshold.

3. **Autorotative entry:** Once in helicopter mode, rotor collective is reduced to configure the rotor for autorotation. The motor provides power during the steady autorotation to slow the descent rate.
4. **Flare and touchdown:** The pilot executes a standard autorotative flare to arrest sink rate. Throughout the descent, flight control laws schedule collective and nacelle tilt as a function of airspeed to account for the partial lift contribution of the wing. Touchdown is completed with no engine power.

The result is a full autorotation capability from any point in the flight envelope. *Mercury*'s motor-assisted rotor speed augmentation provides a guarantee that rotor speed is maintained through the most critical phase of nacelle tilting in the autorotation sequence from cruise.



(a) One Engine Inoperative operation.

(b) All Engine Inoperative operation.

Figure 17.1: Power flow diagram during OEI and AEI operations of *Hermes* and *Mercury* hybrid powertrain.

17.4 Cost

The purchase price, maintenance costs, and operating costs for *Hermes* and *Mercury* are estimated using Harris-Scully cost models outlined in the NDARC theory manual [50]. The aircraft purchase price is calculated using a revised Harris-Scully model that accounts for various factors including empty weight, power available, and number of blades. It also factors in airframe, composites, equipment, flight controllers, batteries, and is adjusted for inflation. The maintenance cost per flight hour is calculated taking into account the total maintenance cost per hour and maintenance cost for the battery, and is similarly adjusted for inflation. The operational cost is calculated based on costs of maintenance, fuel, crew, depreciation, insurance, finance, and emissions.

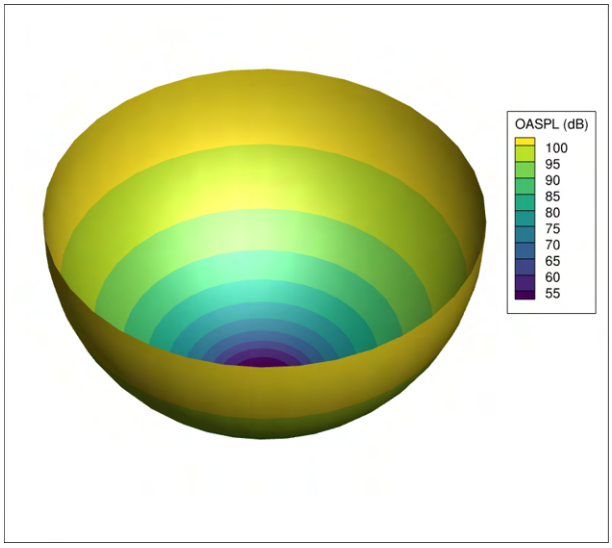
The final estimate calculates a cost with an average error of 18%. *Hermes* is priced at **19.9 million** USD, and *Mercury* is priced at **15.3 million** USD. The aircraft maintenance costs, in dollars per flight hour, are estimated from a statistical relationship in Harris-Scully and adjusted for inflation to 2026. The approximate maintenance costs are **1,300** USD per flight hour and **1,050** USD per flight hour for *Hermes* and *Mercury* respectively. The estimated operating costs are **7,100** USD per flight hour and **5,500** USD per flight hour for *Hermes* and *Mercury* respectively taken for 1100 available block hours per year.

18 Acoustics

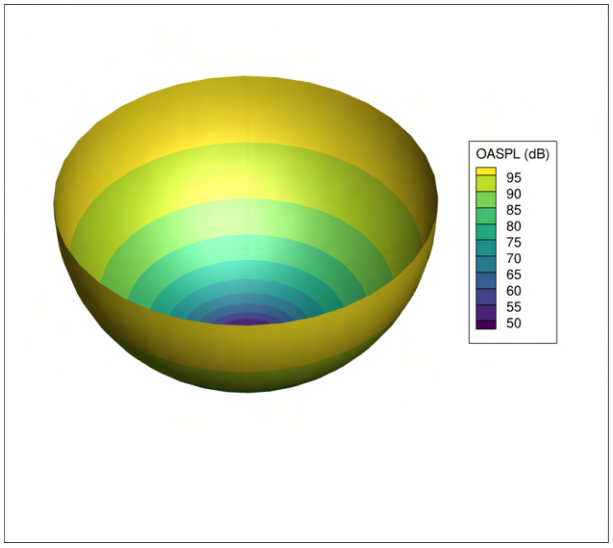
Noise analysis was performed for both *Hermes* and *Mercury* in the hover condition at 4K/95, representing the most acoustically critical segment of the design mission. At this condition the rotor operates at its highest thrust coefficient and no forward speed, producing the strongest periodic blade loading and thickness noise contributions. The elevated noise levels are primarily because of the high rotor tip speed and the high thrust coefficient required at the 4K/95 condition, both of which intensify periodic blade loading and thickness noise.

Sectional aerodynamic loads lift and drag per unit span at each azimuthal and radial station were extracted from the BEMT trim solution and supplied to the Acoustic Code of the University of Maryland (ACUM) [51], an in-house rotorcraft acoustic solver based on Farassat Formulation 1A of the Ffowcs Williams–Hawkings (FW-H) equation [52, 53], to compute the Overall Sound Pressure Level (OASPL).

Observers were distributed over a hemisphere of radius 152 m (500 ft), consistent with the far-field measurement setup of Conner and Wellman [54], centered at the rotor hub with angular resolution of 10° in both azimuth and elevation, covering the lower half-space below the rotor disk plane where community noise propagates in hover. The resulting noise directivity patterns are shown in Fig. 18.1. The predicted peak in-plane OASPL of 100 dB for *Hermes* at 152 m is closer the measured in-plane OASPL of approximately 95-100 dB reported by Conner and Wellman for the XV-15 at the same observer distance. The hemispherical contour illustrates the noise directivity, with the highest levels at the rim corresponding to in-plane observers at rotor disk height, and decreasing toward the base directly below the hub where thickness and loading noise are weakest. *Mercury* achieved a peak OASPL noise reduction of 5 dB relative to *Hermes*, attributed to the reduced blade loading from the optimized chord and twist distribution and the improved sectional c_l/c_d of the AGRC airfoil sections.



(a) *Hermes*: Noise directivity.



(b) *Mercury*: Noise directivity.

Figure 18.1: Noise comparison between *Hermes* and *Mercury* in hover at 4K/95.

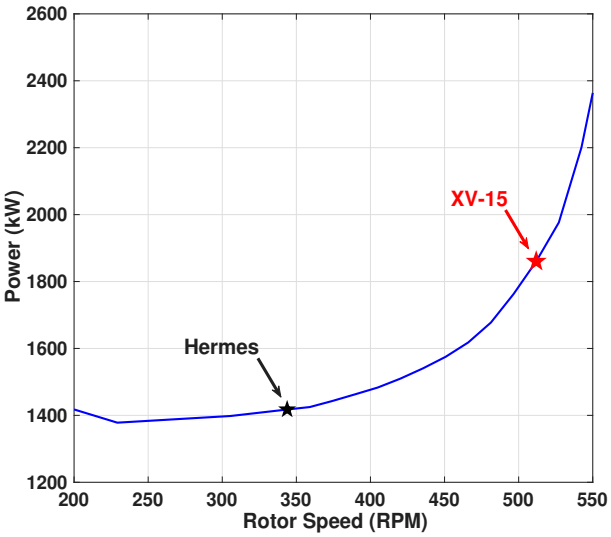
19 Proprotor RPM Strategies

Proprotor RPM variation during the mission is examined in this section. The XV-15 uses a two-speed RPM change between hover and forward flight at 589 RPM and 517 RPM respectively. This two-speed

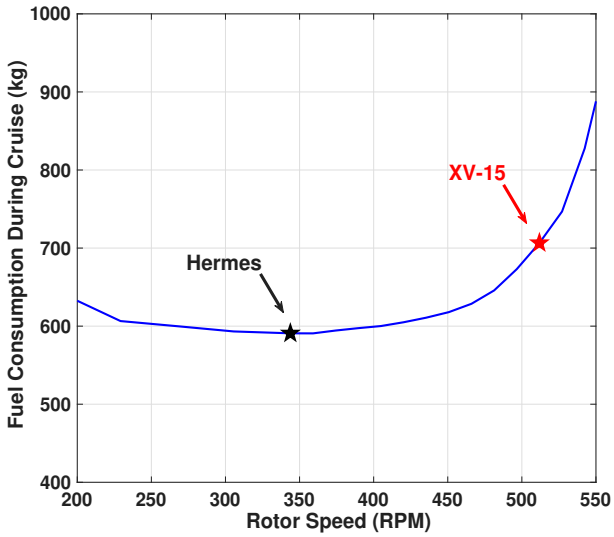
RPM strategy is used in many tiltrotors including the V-22 and AW-609. Likewise, *Hermes* and *Mercury* use a two-speed system. A multi-speed RPM strategy with more than two rotor speeds was considered for *Hermes* and *Mercury*, but such a system did not provide sufficient weight improvements to justify the increased complexity.

19.1 Cruise Rotor Speed Reduction

Reducing the rotor RPM transitioning from hover to cruise provides a significant benefit to cruising efficiency. Lift is primarily provided by the wing in cruise, and the rotor acts as a propeller to provide forward thrust. At high cruise speeds, the rotor tip speed becomes a dominant driver of cruise power due to high rotor profile drag. Reducing the rotor speed substantially lowers the cruise power required, reducing fuel consumption. The XV-15 operates at 517 RPM in airplane mode requiring 1,860 kW (2,494 HP) of power to cruise at 156 m/s (260 KCAS) airspeed and 3,048 m (10,000 ft) altitude as shown in **??**. This high power requirement necessitates 707 kg (1,558 lb) of fuel as shown in 19.1(b). Reducing the rotor RPM, in conjunction with hybridizing, results in the improved efficiency from *Hermes*. At a rotor RPM of 343, *Hermes* operates at 1,397 kW (1873 HP) of power, a 33% reduction compared to XV-15, and minimizes fuel consumption to 590 kg (1,301 lb) if the hybrid system is not utilized. This fuel consumption is further reduced by enabling the hybrid system as outlined in Section 3. The XV-15 was not designed to operate at a rotor speed of 343 RPM, so modifications were made to the drivetrain (Section 4) and rotor (Section 9) to permit the significant rotor speed reduction. During the conversion mode in flight, the engine shaft speed is reduced by 41% to slow the rotor to 343 RPM from 589 RPM.



(a) Cruise power.



(b) Fuel consumption.

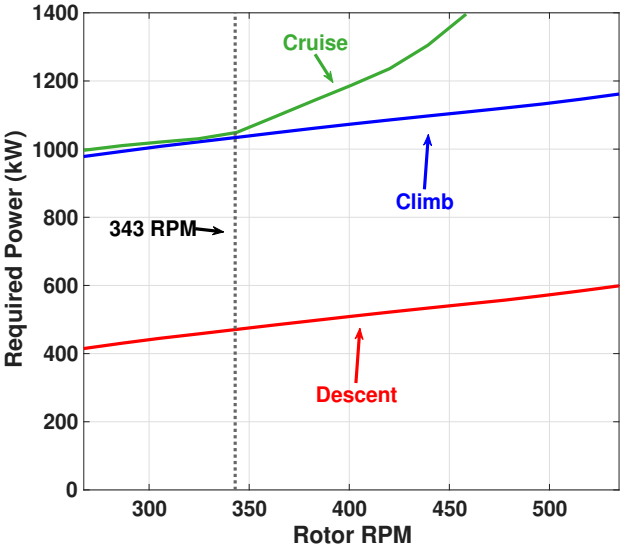
Figure 19.1: Cruise performance of *Hermes* and XV-15 at 3048 m (10000 ft) altitude and 156 m/s (303 kt) airspeed for varying rotor RPM.

Mercury uses the same cruising rotor RPM as *Hermes*. Reducing the rotor RPM below 343 slightly decreases the power required to complete the cruise segment as shown in Fig. 19.2(a). However, this power reduction does not directly correlate with the fuel consumption as the specific fuel consumption of turboshaft engines increases with reduced RPM. As such, the fuel use minimally decreases with rotor RPM below 343 RPM as shown in Fig. 19.2(b). Reducing the RPM from 343 to 267 increases the rotor torque by 22%, considerably increasing the size and weight of the drivetrain. The marginal weight savings accrued by the reduced rotor speed will only be lost by demanding a stronger and larger gearbox and transmission

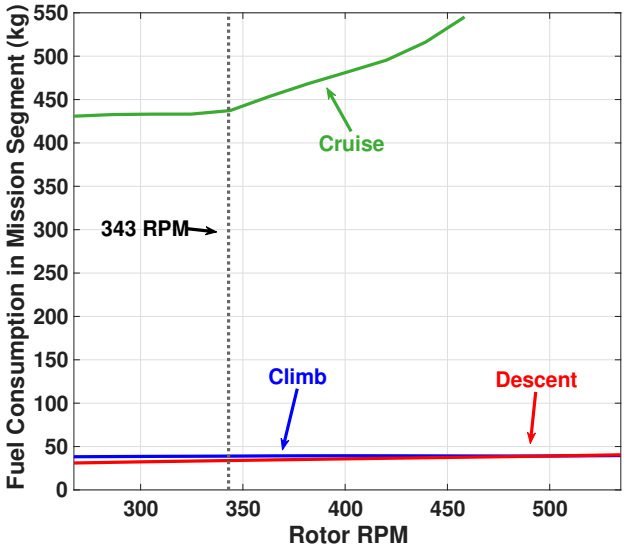
to sustain the increased rotor torque.

19.2 Rotor Speed Variation During Climb and Descent

The climb and descent segments operate at the same rotor speed as the cruise segment. Similarly to cruise, reducing rotor RPM directly decreases the power required as shown in Fig. 19.2(a) and slightly decreases the fuel consumption as shown in Fig. 19.2(b). However, reducing the rotor speed requires strengthening the supercritical cross shaft designed for two-speed operation. This reduced rotor speed approaches the second natural frequency of the shaft. This increased weight from the drivetrain completely negates the fuel savings from performance improvements.



(a) Power required to fulfill climb, cruise, and descent segments for varying rotor RPM for *Mercury*.



(b) Fuel consumed during climb, cruise, and descent segments for varying rotor RPM for *Mercury*.

Figure 19.2: Effect of rotor RPM on climb, cruise, and descent power and fuel consumption for *Mercury*.

19.3 Limitations Caused by Mechanical Drive System

Hermes and *Mercury* utilize a mechanical drive system to rotate the proprotors. Developing a multi-speed RPM strategy introduces numerous design challenges that either increase complexity or weight of the vehicle. An electrically driven system whereby turbogenerators directly power electric motors that in turn spin the proprotors can modulate the motor speed for a continuously variable rotor speed system. A mechanical drive system, however, must utilize a continuously variable transmission (CVT) to replicate the variability of an electric motor. These systems are typically belt-driven, which require significantly more maintenance due to belt slippage, heat, and overall increased wear. Mechanical CVTs have only recently begun development, and as such, have not proven to be reliable systems. An alternative solution is to design a four-speed transmission similar to automobile transmissions to set a rotor speed for each mission segment. This permits a constant engine speed, simplifying the supercritical cross shaft design. Multi-speed transmissions are not typically used on aircraft, and the enormous weight added largely limits their use. All of these systems increase vehicle weight which must be avoided.

The final selected rotor speeds for *Hermes* and *Mercury* along with the XV-15 are shown in Table 19.1. Because *Hermes* and *Mercury* operate at the same rotor speeds, the percent difference compared to the XV-15 is the same for both vehicles.

Table 19.1: Rotor Speeds for XV-15, *Hermes*, and *Mercury*

	XV-15	Hermes	Mercury
Helicopter Mode RPM	589	589	589
Airplane Mode RPM	517	343	343

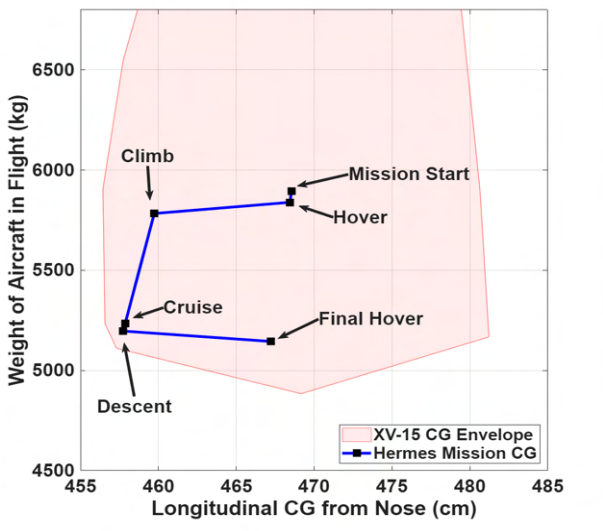
20 Aircraft Comparisons

This section provides a detailed breakdown of three vehicles: the XV-15, *Hermes*, and *Mercury*.

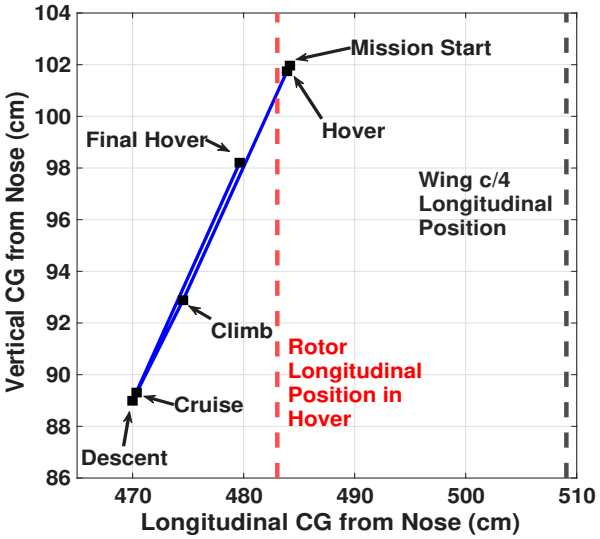
20.1 Vehicle Weight and Balance

The center of gravity (CG) range for the XV-15 covers an envelope shown in Fig. 20.1(a) [17]. The hybrid propulsion system in *Hermes* replaced the drivetrain and rotor, expanded the fuel tanks, and added a battery and electric motor. The overall vehicle propulsive system weight and the rotor weight are comparable to the XV-15. Also, all of these components remain in the relative same location to the longitudinal station of the wing, 480 cm (188 in), from the nose. Thus, the estimated longitudinal CG variation for *Hermes* during the mission remains within the CG envelope of the XV-15.

The vertical and longitudinal CG range for *Mercury* is shown in Fig. 20.1(b). During the hover segments, the CG is located only a few centimeters ahead or behind the rotor. This reduces pilot cyclic inputs and maintains comfortable aircraft pitching angles. During the climb, cruise, and descent segments when *Mercury* is in airplane mode, the CG remains in front of the wing, maintaining static stability in flight.



(a) *Hermes* longitudinal CG from the nose during the mission compared to the XV-15 CG envelope.



(b) Longitudinal and vertical CG from the nose for *Mercury* during the mission

Figure 20.1: Center of gravity (CG) variation for XV-15, *Hermes*, and *Mercury*.

Table 20.1 outlines the weight breakdown of all three vehicles. *Hermes* slightly decreases the empty weight by 1% from 4,581 kg (10,101 lb) on the XV-15 down to 4,552 kg (10,038 lb) and exchanges payload weight for additional fuel to accomplish the RFP mission. The propulsive system on *Hermes* manages to be of similar weight compared to the XV-15 despite the additional components. The improved and redesigned drivetrain required for the hybrid architecture provided the weight savings. Propulsive system accessories include the battery management system, battery charging power electronics, and cooling system. *Mercury*

is a lighter vehicle that accomplishes the same mission. *Mercury* reduces the weight of all components for an overall empty weight reduction of 21% compared to *Hermes*.

Table 20.1: Full Weight Breakdown

Components	**XV-15 Baseline**		**Hermes**		**Mercury**	
	kg	*lb*	*kg*	*lb*	*kg*	*lb*
Rotor	445	981	443	977	271	597
Rotor Blades	269	593	269	593	97	213
Rotor Hub	176	388	174	384	174	384
Wing Structure	429	946	429	946	222	490
Empennage	118	259	118	259	63	136
Horizontal Tail	86	190	86	190	31	69
Vertical Tail	31	69	31	69	32	70
Fuselage	721	1589	721	1589	625	1379
Landing Gear	238	524	238	524	151	362
Nacelle Structure	166	365	166	365	135	297
Flight Controls and Hydraulics	644	1420	644	1420	522	1152
Propulsive System	1259	2776	1232	2717	1132	2497
Engine	548	1209	548	1209	457	1007
Battery	0	0	86	191	72	159
Electric Motor	0	0	16	35	16	35
Accessories	0	0	37	83	48	106
Fuel Tanks	102	226	117	257	96	211
Drivetrain	608	1341	427	942	444	978
Avionics, Instruments, and Electrical Systems	302	666	302	666	215	475
Miscellaneous (Furnishings, Environmental Controls, etc.)	261	576	261	576	249	550
TOTAL EMPTY WEIGHT	**4581**	**10101**	**4552**	**10038**	**3599**	**7937**
Mission Fuel	651	1436	834	1839	615	1355
Payload and Crew	664	1463	509	1123	726	1600
GROSS WEIGHT	**5897**	**13000**	**5897**	**13000**	**4940**	**10892**

20.2 General Overview of All Aircraft

Table 20.2 outlines key operating parameters and characteristics of all three vehicles. The XV-15 does not operate the same mission as *Hermes* and *Mercury*, so the mission payload and fuel are not directly comparable. *Hermes* installs the same T53 engines as the XV-15 and augments it with a battery and motor to increase maximum continuous power output by 8.3% at sea level. The fuel capacity is also expanded by 24% to meet mission requirements. *Mercury* decreases the gross weight to 4939 kg (10892 lb), a 16.2%





reduction from *Hermes*. The lower weight enables the installation of two downscaled engines with a battery and motor to produce 1521 kW (2040 HP) at sea level. *Mercury* uses less fuel and carries more payload to complete the mission.

Table 20.2: General Vehicle Parameters

	XV-15 Baseline		**Hermes**		**Mercury**	
	kg	*lb*	*kg*	*lb*	*kg*	*lb*
Gross Takeoff Weight	5895.7	13000.0	5895.7	13000.0	4939.4	10891.5
Mission Payload Weight	663.7	1463.4	509.1	1122.6	725.8	1600.0
Turboshaft Engine Weight	548.1	1208.6	548.1	1208.6	456.8	1007.3
Battery Weight	N/A		86.4	190.5	72.0	158.8
Electric Motor Weight	N/A		16.0	35.3	16.0	35.3
Mission Fuel Weight	651.2	1436.0	834.2	1839.3	614.5	1355.0
Maximum Fuel Weight	675.7	1490.0	839.0	1850.0	639.5	1410.0
Max Gross Takeoff Weight at Sea Level, VTOL	6802.7	15000.0	7149.7	15765.0	6335.6	13970.0
Max Gross Takeoff Weight at Sea Level, STOL	6802.7	15000.0	7149.7	15765.0	6335.6	13790.0
	m	*ft*	*m*	*ft*	*m*	*ft*
Rotor Diameter	3.8	12.5	3.8	12.5	3.8	12.5
Wing Span	9.8	32.2	9.8	32.2	9.8	32.2
	kW	*HP*	*kW*	*HP*	*kW*	*HP*
Single Turboshaft Maximum Continuous Power (MCP) at Sea Level	932.1	1250.0	932.1	1250.0	670.7	899.4
Single Turboshaft Maximum Rated Power (MRP) at Sea Level	1155.8	1550.0	1155.8	1550.0	831.6	1115.2
Electric Motor Maximum Power	N/A		180.0	241.4	180.0	241.4
Battery Maximum Power Output	N/A		216.0	289.6	180.0	241.4
Total Maximum Continuous Power (MCP) at Sea Level	1864.2	2500.0	2018.7	2707.2	1521.4	2040.2
	kWh		*kWh*		*kWh*	
Battery Energy Capacity	N/A		21.6		18.0	

21 Additional Mission Capabilities

Mercury's hybrid-electric propulsion system, high cruise speed, and "hot and high" VTOL capability enables a variety of missions beyond its primary transport role.

Emergency Medical Services & Search and Rescue: *Mercury* combines rapid response with extended

loiter capability up to 8 hours. Hybrid operation reduces fuel consumption during search or standby phases, while cruise speeds exceeding 300 kt enable fast transport of rescue personnel, patients, or survivors between remote locations and medical facilities.

VIP & Intercity Transport: The six-passenger cabin and high speed cruise enable rapid city-center-to-city-center travel. *Mercury* combines the accessibility of a helicopter with cruise speeds approaching those of regional fixed-wing aircraft, providing a competitive door-to-door transportation solution.

Offshore Energy Support & Critical Logistics: *Mercury* provides rapid transportation of personnel, equipment, and time-sensitive cargo to offshore platforms and remote sites. Its VTOL capability eliminates dependence on airport infrastructure, while high cruise speed significantly reduces transit times compared to conventional rotorcraft.



(a) Emergency Medical Services & SAR



(b) Offshore Energy Support



(c) VIP & Intercity Transport

Figure 21.1: Alternative mission capabilities of *Mercury*.

22 Summary

The University of Maryland Graduate Design Team presents two hybrid electric tiltrotors in response to the 43rd Annual VFS Student Design Competition, sponsored by Leonardo: *Hermes*, a constrained hybrid redesign of the XV-15 for phase I, and *Mercury*, a clean-sheet minimally constrained hybrid electric tiltrotor for phase II. Both designs adopt a parallel hybrid architecture and demonstrate that hybrid electrification of a tiltrotor platform is not only technically achievable but offers a compelling combination of performance, efficiency, and technical readiness for the emerging civil tiltrotor market.

Phase I: *Hermes*

Hermes retains the proven XV-15 airframe and T53 turboshaft engines while integrating a centrally mounted electric motor and battery pack to deliver meaningful improvements in hover performance, cruise speed, and fuel efficiency within the original 13,000 lb gross takeoff weight.

1. A parallel hybrid architecture mechanically couples both T53 turboshaft engines and a single H3X HPDM-180R electric motor through a supercritical cross-shaft, providing 10% electrically sourced power while minimizing added component weight and avoiding intermediate power conversion losses.
2. *Hermes* is capable of hover out of ground effect at full gross takeoff weight under "hot and high" 4K/95 conditions by supplementing engine power with 180 kW of battery discharge during the initial five-minute hover segment.
3. A 40% rotor speed reduction in cruise, enabled by a redesigned constant velocity gimbaled hub, substantially lowers rotor power, allowing for sustained flight at 156 m/s (260 KCAS at 10,000 ft).
4. A dedicated Full Authority Digital Engine Controller (FADEC) on each turboshaft, replacing the XV-15's original hydromechanical fuel control units, combined with a central Hybrid Management

Computer (HMC), fully automates all power splitting, engine governing, and battery management. The pilot engages the hybrid strategy via a single switch. The FADEC and HMC coordinate turboshaft output, motor torque, and battery state of charge without further pilot input, substantially reducing workload throughout the mission.

5. The battery undergoes five recharge/discharge cycles during cruise, keeping the charge C-rate below 9 to ensure safe thermal operation and battery longevity.
6. A closed-loop liquid cooling system maintains battery temperature below 70°C and keeps the electric motor within safe operating limits during the demanding 4K/95 hover segment, where the combined battery and motor waste heat reaches 43.5 kW.
7. Supercritical cross-shafting operating above the shaft's first natural frequency reduces cross-shaft weight by 50% through decreased material requirements and elimination of redundant support bearings.
8. The empty weight of 10,038 lb is marginally lower than the original XV-15 despite the addition of hybrid components, achieved through modern drivetrain materials and electronic hybrid engine control.
9. *Hermes* achieves a maximum range of 1,308 km (706 nmi) and a maximum endurance of 5 hours, exceeding the XV-15 in both metrics due to reduced cruise power and expanded onboard fuel capacity.

Phase II: *Mercury*

Mercury is a clean-sheet, parallel hybrid electric tiltrotor that leverages modern materials, aerodynamic optimization, and structural redesign to maximize the benefits of hybrid propulsion. At a gross takeoff weight of only 4,989 kg (10,891 lb), 15% lighter than *Hermes* and the XV-15, *Mercury* meets all Phase II RFP requirements while delivering superior range, payload, and operating economy.

1. *Mercury* retains the same parallel hybrid architecture as *Hermes*, a H3X HPDM-180R motor mechanically coupled through a supercritical cross-shaft, paired with 30% downscaled T53 engines with 671 kW MCP (912 HP), sized through the same hybrid selection procedure, with at least 10% of mission power sourced or distributed electrically.
2. A 28% overall drag reduction relative to the XV-15 baseline is achieved through a slim fuselage enabled by a 1×6 single-row cabin and tandem pilot seats (29% fuselage drag reduction), a thin 13% thick carbon/epoxy composite wing free from whirl flutter through the 180 m/s (350 KTAS) limit airspeed (25% wing drag reduction), and streamlined nacelles in which only the rotor tilts while the engine remains fixed (25% nacelle drag reduction).
3. An aerodynamically optimized composite proprotor planform improves propulsive efficiency by 5.9% and hover figure of merit by 6.3% relative to the XV-15 rotor, while satisfying the RFP constraint of 25 ft diameter compatible with the NASA 40×80 wind tunnel.
4. *Mercury* meets the RFP payload requirement of 726 kg (1,600 lb) for six passengers and two crew at 90.7 kg (200 lb) each, completing the full 567 km (306 nmi) mission profile with a 10% fuel reserve, exceeding the payload-carrying capability of *Hermes*.
5. A fly-by-wire flight control system with triplexed flight control computers replaces the XV-15's mechanical mixing linkages. Redundancy is sized to the consequence of failure: swashplate actuators are triplexed, conversion actuators are duplexed, and fixed-wing surface actuators are simplex with a safe hover fallback.
6. *Mercury* retains the FADEC and Hybrid Management Computer architecture developed for *Hermes*. A liquid cooling system maintains battery and motor temperatures within safe limits during the

hover segment, accommodating *Mercury's* 36.8 kW combined waste heat load.

7. *Mercury* achieves hover out of ground effect at full 4,940 kg (10,891 lb) gross takeoff weight under 4K/95 conditions using the electric motor to supplement the downscaled engines at takeoff power, satisfying the RFP HOGE requirement.
8. A 40% rotor speed reduction from 589 RPM in hover to 343 RPM in cruise, enables sustained flight at 260 KCAS (303 KTAS) at 3,048 m (10,000 ft), with a maximum operating speed of 168 m/s (327 KTAS) exceeding the RFP V_{NO} requirement of 300 KTAS.
9. *Mercury* is designed to handle OEI consistent to civil CS-29 Category A standards: the cross-shaft transmits surviving-engine power to both rotors, while the electric motor provides instant contingency power. Entry into autorotation is available at any airspeed or flight mode via the fly-by-wire system and central electric motor.
10. With mission fuel, two pilots, and a full 6-passenger payload, *Mercury* achieves a range of 1,063 km (574 nm) and an endurance of 4.7 hours. With auxiliary fuel tanks and no payload, maximum range extends to 1,895 km (1,023 nm) and maximum endurance reaches 8.9 hours.

Hermes demonstrates a practical and low-risk pathway to hybridizing an existing tiltrotor platform, while *Mercury* illustrates the full potential of a purpose-designed hybrid-electric aircraft. Together, they show that hybrid-electric tiltrotors can deliver superior efficiency, safety, and operational flexibility, making them strong candidates for the next generation of regional and civil vertical-lift transportation.

23 Team Composition

The UMD Graduate Design Team brings together 9 members spanning experimental research, computational analysis, and systems engineering, providing broad coverage of the disciplines required for an integrated hybrid tiltrotor design.

Visesh Uppoor (Team Lead) brings experimental and comprehensive analysis experience in high-speed rotorcraft aeroelasticity, contributing to structures, aeroelastic stability, and overall systems integration across both phases.

Howard Zheng contributed to vehicle sizing and performance, and brings research experience in compound rotorcraft experimentation.

Alex Teacu brings a background in autonomous technology and space vehicle design, contributing CAD and the application of cross-domain design approaches to rotorcraft problems.

Manmohan Thakur brings expertise in machine learning applied to aerodynamic optimization, which was applied directly to aerodynamic design in this project. He also comes with much work experience in industry before joining graduate school.

Jacques Read brings experience across multiple design projects in transmission and powertrain analysis, leading the drivetrain and gearbox design.

Marge Donovan brings expertise in rotorcraft blade structural design and manufacturing from her work on extraterrestrial rotorcraft, contributing to primary load-bearing structural design.

John Schmidt brings a research background in hybrid power strategies for rotorcraft, leading development of the hybrid architecture and detailed component sizing.

Dakota Brakob brings five years of industry experience in conceptual design, structural and fluid analysis, and motion studies across a range of vehicle scales, contributing detailed FEA of key structural components.

John Jessamy is a graduate student in aerospace engineering with experience in CAD and novel vehicle configuration studies, contributing to vehicle layout and configuration development.

References

[1] Newgard, C. D., Schmicker, R. H., Hedges, J. R., Trickett, J. P., Davis, D. P., Bulger, E. M., Aufderheide, T. P., et al., "Emergency Medical Services Intervals and Survival in Trauma: Assessment of the "Golden Hour" in a North American Prospective Cohort," *Annals of Emergency Medicine*, Vol. 55, No. 3, 2010, pp. 235–246.e4.

[2] Airbus, "EcoPulse: The Distributed Hybrid-Electric Propulsion Demonstrator," 2023, Accessed: 2026-05-29.

[3] Johnson, W., Silva, C., and Solis, E., "Concept Vehicles for VTOL Air Taxi Operations," *AHS Specialists' Conference on Aeromechanics Design for Transformative Vertical Flight*, San Francisco, CA, Jan 2018, Report Number: ARC-E-DAA-TN50731.

[4] Saias, C. A., Goulos, I., Roumeliotis, I., Pachidis, V., and Bacic, M., "Preliminary Design of Hybrid-Electric Propulsion Systems for Emerging Urban Air Mobility Rotorcraft Architectures," *Journal of Engineering for Gas Turbines and Power*, Vol. 143, No. 11, Nov 2021, pp. 111015.

[5] Saias, C. A., Goulos, I., Pachidis, V., and Bacic, M., "On the Effects of Optimal Implementation of Variable Rotor Speed and Power Management on Hybrid-Electric Rotorcraft," *Journal of Engineering for Gas Turbines and Power*, Vol. 145, No. 3, Mar 2023, pp. 031028.

[6] Mills, B. and Datta, A., "Fundamental Studies of Variable-Voltage Hybrid-Electric Powertrains," *Journal of the American Helicopter Society*, Vol. 66, No. 2, April 2021, pp. 1–14.

[7] Arace, M. and Datta, A., "Fundamental Understanding of Hybrid-Electric Power," *Vertical Flight Society Annual Forum 79*, West Palm Beach, FL, May 16-18, 2023.

[8] Arace, M. and Datta, A., "Impact of Detailed SFC on Hybrid-Electric VTOL Sizing," *Vertical Flight Society Annual Forum 80*, Montreal, Quebec, May 7-9, 2024.

[9] Schmidt, J. L., Xu, H., and Datta, A., "Experimental Exploration of Hybrid-Electric Power for VTOL Aeromechanics Design," *AIAA SCITECH 2025 Forum*, 2025.

[10] Schmidt, J. L., Xu, H., and Datta, A., "Experimental Exploration of Battery-Engine Hybrid-Electric Power Sharing," *Vertical Flight Society Annual Forum 81*, Virgina Beach, VA, May 20-22, 2025.

[11] Liu, J. and Peng, H., "Modeling and Control of a Power-Split Hybrid Vehicle," *IEEE Transactions on Control Systems Technology*, Vol. 16, No. 6, 2008, pp. 1242–1251.

[12] Denis, N., Dubois, M. R., Trovão, J. P. F., and Desrochers, A., "Power Split Strategy Optimization of a Plug-in Parallel Hybrid Electric Vehicle," *IEEE Transactions on Vehicular Technology*, Vol. 67, No. 1, 2018, pp. 315–326.

[13] Tuegel, E., "AIRCRAFT STRUCTURAL RELIABILITY AND RISK ANALYSIS HANDBOOK," Vol. 2, 2020.

[14] "T53 Engine Experience Report," Tech. Rep. USAAAVS-PAM-74-11, Army Agency for Aviation Safety, Fort Rucker, AL, 1974, Accession Number: ADA373234. Available at `https://apps.dtic.mil/sti/tr/pdf/ADA373234.pdf`.

[15] Justin, C., Patel, S., Bouchard, E. D., Gladin, J., Verberne, J., Li, E., Ozcan, M., Rajaram, D., Mavris, D., D'Arpino, M., Aldemir, T., Rizzoni, G., Türkmen, G. S., Mayo, M., and Bivens, C., "Reliability and Safety Assessment of Urban Air Mobility Concept Vehicles," NASA Contractor Report NASA/CR-20210017185, National Aeronautics and Space Administration, Moffett Field, CA, March 2021.

[16] Ohneseit, S., Finster, P., Floras, C., Lubenau, N., Uhlmann, N., Seifert, H. J., and Ziebert, C., "Thermal and Mechanical Safety Assessment of Type 21700 Lithium-Ion Batteries with NMC, NCA

and LFP Cathodes–Investigation of Cell Abuse by Means of Accelerating Rate Calorimetry (ARC)," Vol. 9, No. 5, pp. 237.

[17] Maisel, M. D., Borgman, D. C., and Few, D. D., "Tilt Rotor Research Aircraft Familiarization Document," NASA-TM x-62407, Jan. 1975.

[18] Maisel, M. D., Giulianetti, D. J., and Dugan, D. C., "The History of the XV-15 Tilt Rotor Research Aircraft: From Concept to Flight," NASA SP- 2000-4517, 2000.

[19] U.S. House Armed Services Committee, "V-22 Program Update," 2025, Accessed: 2026-02-11.

[20] Carpenter Technology Corporation, "AerMet® 310 Datasheet," 2025, Accessed: 2026-05-01.

[21] Carpenter Technology Corporation, "Pyrowear® 53 Datasheet," 2025, Accessed: 2026-05-01.

[22] Sonneborn, W. G., Covington, C. E., and Wilson, K., "V-22 PROPULSION SYSTEM DESIGN," *Seventeenth European Rotorcraft Forum*, 1991.

[23] Safran Helicopter Engines, "Removable Pack for Reactivating a Turboshaft Engine, Architecture for a Multi-Engine System for Propelling a Helicopter, provided with such a Pack, and Corresponding Helicopter," 2015.

[24] Rosenstein, H. and Clark, R., "Aerodynamic development of the V-22 tilt rotor," *Aircraft Systems, Design and Technology Meeting*, 1986, p. 2678.

[25] Kulfan, B. M., "The CST universal parametric geometry representation method, recent extensions and applications," *Proc R Aeronaut Soc Conf*, Vol. 114, 2007, pp. 157–176.

[26] Mitchell, M., *An introduction to genetic algorithms*, MIT press, 1998.

[27] Anand, A., Safdar, M. M., Marepally, K., and Baeder, J. D., "A comprehensive review of neural network training approaches for airfoil design and optimization," *AIAA SCITECH 2025 Forum*, 2025, p. 271.

[28] Jung, Y. S., *Hamiltonian Paths and Strands for Unified Grid Approach for Computing Aerodynamic Flows*, University of Maryland, College Park, 2019.

[29] Deb, K., Pratap, A., Agarwal, S., and Meyarivan, T., "A fast and elitist multiobjective genetic algorithm: NSGA-II," *IEEE transactions on evolutionary computation*, Vol. 6, No. 2, 2002, pp. 182–197.

[30] Office of the Federal Register, "Part 25.581 Lightning Protection," April 8 1970.

[31] Patil, M. and Datta, A., "A Scalable Time-Parallel Solution of Periodic Rotor Dynamics in X3D," *Journal of the American Helicopter Society*, Vol. 66, No. 4, October 2021, pp. 1–16.

[32] Gaffey, T. M., "The Effect of Positive Pitch-Flap Coupling (Negative δ_3) on Rotor Blade Motion Stability and Flapping," *Journal of the American Helicopter Society*, Vol. 14, No. 2, April 1969, pp. 49–67.

[33] Kassapoglou, C., *Design and Analysis of Composite Structures: With Applications to Aerospace Structures*, Aerospace Series, Wiley, 2011.

[34] Akinwale, A. and Datta, A., "The Effect of Pylon Center of Gravity on Tiltrotor Whirl-Flutter," *AIAA SciTech 2025 Forum*, Jan. 2025.

[35] Gul, S. and Datta, A., "Development of an Aeromechanics Solver for Loads and Stability of Hingeless Tiltrotors," *Journal of Aircraft*, Vol. 60, No. 1, Jan. 2023, pp. 143–159.

[36] Thakur, M., Anand, A., Marepally, K., and Baeder, J., "A Novel Parameterization Framework and Neural Network-Based Surrogate Modeling for Rotorcraft Fuselage Aerodynamic Prediction." *AIAA SCITECH 2026 Forum*, 2026, p. 1117.

[37] Jude, D., Lee, B., Jung, Y. S., Petermann, J., Govindarajan, B., and Baeder, J., "Application of a Heterogeneous CFD Framework Towards Simulating Complete Rotorcraft Configurations," *American Helicopter Society, 74th Annual Forum Proceedings, Phoenix, Arizona, May 14-17, 2018*.

[38] Hiken, A., "The Evolution of the Composite Fuselage: A Manufacturing Perspective," *Aerospace Engineering*, edited by G. Dekoulis, chap. 5, IntechOpen, 2019, pp. 95–124.

[39] ATR, *ATR 72-500 Structures Training Manual: ATA 57 – Wings*, 2012, Level 3 Maintenance Training Manual.

[40] Gudmundsson, S., *General Aviation Aircraft Design Applied Methods and Procedures*, Elsevier Inc., 2022.

[41] C. A. Widdison, J.P. Magee, H. A., "Conceptual Design Study of a 1985 Commercial STOL Tilt Rotor Transport," Tech. Rep. NASA CR 137601, Boing Vertol Company, 1974.

[42] Federal Aviation Administration, Washington, DC, USA, *Pilot Compartment View Design Considerations*, 1993.

[43] Toyota Motor Corporation, *2026 Prius Owner's Manual: Vehicle Status Information and Indicators – Instrument Cluster – Energy Monitor/Consumption Screen*, Toyota Motor Corporation, 2026, Accessed: 2026-05-28.

[44] Prouty, R. W., *Helicopter performance, stability, and control*, 1995.

[45] McCroskey, W. J., Spalart, P. R., Laub, G. H., Maisel, M. D., and Maskew, B., "Airloads on Bluff Bodies, with Application to the Rotor-Induced Downloads on Tilt-Rotor Aircraft," NASA-TM 84401, Sept. 1983.

[46] Hoerner, S., *Fluid-Dynamic Drag*, Vol. 2, Sighard F. Hoerner, 1958.

[47] Anderson, J., *Fundamentals of Aerodynamics*, McGraw-Hill series in aeronautical and aerospace engineering, McGraw-Hill Education, 2017.

[48] McCroskey, W., Spalart, P., Laub, G., Maisel, M., and Maskew, B., "Airloads on Bluff Bodies, with Application to the Rotor-Induced Downloads on Tilt-Rotor Aircraft." Tech. rep., 1983.

[49] Wood, T., "One Engine Inoperative (OEI) and Autorotation for Heavy Lift Rotorcraft System," NASA Contractor Report NASA/CR-2012-216038, NASA Ames Research Center, Moffett Field, California, Aug. 2012, Prepared by Bell Helicopter Textron, Inc., Hurst, Texas under Contract No. NAS2-01063, Task Order 15.

[50] Johnson, W., "NDARC: NASA Design and Analysis of Rotorcraft," NASA-TP 20250010468, Nov. 2025.

[51] Jayasundara, D., "Long Duration Aeroacoustic Simulations," 2021.

[52] Williams, J. F. and Hawkings, D. L., "Sound generation by turbulence and surfaces in arbitrary motion," *Philosophical Transactions for the Royal Society of London. Series A, Mathematical and Physical Sciences*, 1969, pp. 321–342.

[53] Farassat, F., "Linear acoustic formulas for calculation of rotating blade noise," *AIAA journal*, Vol. 19, No. 9, 1981, pp. 1122–1130.

[54] Conner, D. A. and Wellman, J. B., "Hover acoustic characteristics of the XV-15 with advanced technology blades," *Journal of Aircraft*, Vol. 31, No. 4, 1994, pp. 737–744.